

Dynamic Plasmonic Systems with Actuating Nanotransducers

Sean Cormier
Christ's College



A thesis presented for the degree of
Doctor of Philosophy

Department of Physics
University of Cambridge

November, 2019

Declaration

This dissertation is the result of my own research undertaken at the University of Cambridge and does not include work done in collaboration with others except where specified in the text. This work has not been submitted in whole or part for a degree or other qualification at the University of Cambridge or other universities and does not exceed the prescribed word limit of 60,000 words.

Sean Cormier
November, 2019

This thesis is dedicated to my family and dear friends.

Acknowledgements

I owe a great deal of gratitude to the many who have supported me throughout my PhD. This thesis would not have been completed without their support.

Firstly, I would like to thank my PhD supervisor, Jeremy Baumberg, for his support throughout my PhD. His excitement for science is contagious and his continuous stream of interesting ideas made the hard work in the lab rewarding and enjoyable. His guidance throughout my PhD was very helpful and very much appreciated.

I would also like to thank my previous supervisor Mathias Kolle for his early guidance in my research career. His academic advice and recommendation of the University of Cambridge prompted my PhD application. But most importantly, his trust in me to independently design and conduct experiments helped foster my strong passion for scientific research.

I am incredibly grateful for my time in the NanoPhotonics Centre. The group has been as welcoming as it has been stimulating. Everyone in the group has helped make my experience in Cambridge exceptional with fascinating discussions, exciting collaborations, and friendships. There are several notable members of the group who have directly contributed to some of the work described in this thesis. In particular, I would like to thank Andrew Salmon, Vladimir Turek, Jialong Peng, Hyeon-Ho Jeong, Marlous Kamp, Bart de Nijs and Hamid Ohadi for their help designing experiments and optical setups. I also would like to thank Cloudy, Dean, Rohit, Will, Marie-Elena, Alex, Wenting, Jack, David, Demelza, Charlie, Junyang, Yago, Jan, Giuliana, Matthew, Wilson, Ivana, Femi, Elena, Alex, Eoin and Ermanno. Their collective optimism and creativity helped spin experimental failures into new exciting collaborative ideas with many successes.

I would also like to extend my thanks to the university staff who have supported my research. The lab technicians, Anthony and Giovanni, have been especially useful and resourceful for building and implementing experimental designs. Colin and the IT team have helped maintain the functionality of all lab machines, and the administrative staff have provided constant friendly support for many essential tasks. I am very grateful for all their support.

I would like to acknowledge the financial support I received from the Winton Programme for the Physics of Sustainability and the C T Taylor Cambridge Trust Fund. Without this funding my PhD studies would not have been possible.

I am also thankful for all the communities that have given me the pleasure of belonging. I am grateful for my time at Christ's College, which greatly enriched my life beyond the lab. I really enjoyed being part of the graduate community and I will cherish all the people I have met and the shared memories from the years I have spent in Cambridge.

Above all, I am most thankful for my wonderful family for all their love and continuous support. I thank my parents for supporting my endeavours far from home and my brothers, Nick and Alex, as well as my close family for the great company and, sometimes witty, comic relief. You are all loved greatly.

Abstract

The development of programmable nanomachines that deliver therapeutic drugs to specific target sites, assemble objects, or work together to apply coherent forces on-demand has been long sought after in the field of nanotechnology. A major hurdle in this endeavour is the lack of a reliable source of power for driving these machines. In this work, plasmonic nanoparticles coated with thin thermoresponsive polymeric shells actuate in response to light to give rapid, dynamic optical and mechanical responses. They are called actuating nanotransducers (ANTs). Their fast, reversible response and small size suggests they are good candidates for powering nanomachines.

ANTs consist of gold nanoparticles coated with the poly(N-isopropylacrylamide) (PNIPAM). Gold nanoparticles have renowned tunable plasmonic properties, while PNIPAM is a well-known polymer that expands and contracts in response to temperature in aqueous media. The particular combination of these materials enables fast local actuation of the PNIPAM shell in response to light via plasmonic heating. These simple nanoparticle actuators exhibit optical and self-assembly behaviours that vary greatly depending on their environment.

In this thesis, various ANT systems are studied. The crucial role of local surface charge on the reversible self-assembly of gold colloids is examined. The mechanical responses of individual ANTs are characterised in Nanoparticle on Mirror plasmonic structures. The dynamic behaviours of ANTs in thin-films and microdroplets are also investigated. It is observed that the thin-films undergo a reversible insulator-to-metal transition that is well captured with an effective medium model. In addition, the microdroplets are shown to mimic the optical response of chromatophores, giving rise to substantial changes in colour. This work demonstrates that the optical and physical properties of individual ANTs can be switched with light, and particle ensembles can effectuate significant responses at much larger scales.

List of Publications

- [1] Marie-Elena Kleemann, Jan Mertens, Xuezhi Zheng, Sean Cormier, Vladimir Turek, Felix Benz, Rohit Chikkaraddy, William Deacon, Anna Lombardi, Victor V. Moshchalkov, Guy A. E. Vandenbosch, and Jeremy J. Baumberg. Revealing Nanostructures through Plasmon Polarimetry. *ACS Nano*, 11(1):850–855, 2017.
- [2] Sean Cormier, Tao Ding, Vladimir Turek, and Jeremy J. Baumberg. Actuating Single Nano-Oscillators with Light. *Advanced Optical Materials*, 6(6):1701281, 2018.
- [3] Vladimir A. Turek, Rohit Chikkaraddy, Sean Cormier, Bill Stockham, Tao Ding, Ulrich F. Keyser, and Jeremy J. Baumberg. Thermo-Responsive Actuation of a DNA Origami Flexor. *Advanced Functional Materials*, 28(25):1706410, 2018.
- [4] Sean Cormier, Tao Ding, Vladimir Turek, and Jeremy J. Baumberg. Dynamic- and Light-Switchable Self-Assembled Plasmonic Metafilms. *Advanced Optical Materials*, 6(14):1800208, 2018.
- [5] Vladimir A. Turek, Sean Cormier, Benjamin Sierra-Martin, Ulrich F. Keyser, Tao Ding, and Jeremy J. Baumberg. The Crucial Role of Charge in Thermoresponsive-Polymer-Assisted Reversible Dis/Assembly of Gold Nanoparticles. *Advanced Optical Materials*, 6(8):1701270, 2018.
- [6] Junyang Huang, Bart de Nijs, Sean Cormier, Kamil Sokolowski, David-Benjamin Gryns, Charlie A. Readman, Steven J. Barrow, Oren A. Scherman, and Jeremy J. Baumberg. Plasmon-induced optical control over dithionite-mediated chemical redox reactions. *Faraday Discussions*, 214, 2019.
- [7] Jialong Peng, Hyeon-Ho Jeong, Qiangi Lin, Sean Cormier, Hsin-Ling Liang, Michael F. L. De Volder, Silvia Vignolini, and Jeremy J. Baumberg. Scalable electrochromic nanopixels using plasmonics. *Science Advances*, 5(5):eaaw2205, 2019.

Submitted:

- [1] Andrew R. Salmon*, Sean Cormier*, Wenting Wang, Chris Abell, and Jeremy J. Baumberg. Motile Artificial Chromatophores: Light-Triggered Nanoparticles for

Microdroplet Locomotion and Color Change. *Advanced Optical Materials*, 2019.

**Equal Contribution.*

Contents

1	Introduction	1
1.1	Outline	2
1.2	Light Interactions with Metal Nanoparticles	4
1.2.1	Localised Surface Plasmon Polaritons	6
1.2.2	Plasmonic Coupling Between Nanospheres	8
1.2.3	Plasmonic Nanoparticle Heating	9
1.3	Stimuli-responsive Polymers	14
1.3.1	Lower Critical Solution Temperature	14
1.4	Forces on the Nanoscale	18
1.5	Summary	21
2	Actuating Nanotransducers	23
2.1	Au@PNIPAM Core-shell Nanoparticles	23
2.2	ANT Flocculation	25
2.2.1	Heating-induced Flocculation	25
2.2.2	Light-induced Flocculation	29
2.3	Summary	30
3	Materials and Methods	33
3.1	ANT Synthesis	33
3.1.1	Gold Nanoparticle Cores	33
3.1.2	Grafting PNIPAM Shells	35
3.2	Substrates for ANT Systems	37

3.2.1	Template-stripped Gold	37
3.2.2	Semi-permeable Membranes	37
3.3	Optical Setups and Techniques	38
3.3.1	Extinction Spectroscopy	38
3.3.2	Dynamic Light Scattering	40
3.3.3	Microscopy Techniques	41
3.4	Summary	44
4	Formation of ANT Clusters	45
4.1	Cluster Formation Mechanism	45
4.2	Modelling ANT Clusters	47
4.2.1	Multisphere T-matrix Simulations	48
4.2.2	Extrapolated Cluster Model	50
4.3	Effects on ANT Cluster Formation	52
4.3.1	Effects of PNIPAM Termination	52
4.3.2	Effects of Ionic Strength	54
4.3.3	Effects of Excess PNIPAM	57
4.4	Conclusion	57
5	ANT on Mirror	59
5.1	ANT on Mirror Structure	59
5.2	Numerical Modelling of ANToM	65
5.3	Heat-induced Switching	68
5.4	Light-induced Switching	69
5.4.1	Light-induced Damage	72
5.5	ANT Force and Efficiency	74
5.6	Dynamics of Polymer Nano-shells	74
5.7	Conclusion and Outlook	76

6	Dynamic ANT Films	77
6.1	ANT Film Preparation	77
6.2	ANT Film Structure	78
6.3	Modelling Optical Properties	79
6.3.1	Effective Medium Approximation	79
6.3.2	Thin-film Interference	82
6.4	ANT Film Switching	84
6.4.1	Bulk Heating	84
6.4.2	Light-induced Heating	86
6.5	Self-healing Behaviour	90
6.6	Printing by Sintering	90
6.7	Conclusion	92
7	ANT Microdroplets	93
7.1	Artificial Chromatophores	93
7.1.1	Optical Response to Bulk Heating	95
7.1.2	Local Light-induced Heating Effects	98
7.2	ANT Microdroplet Swimmers	101
7.3	Conclusion	102
8	Conclusions and Outlook	105
8.1	Summary	105
8.2	Future Directions	107
	References	111



1. Introduction

For over half a century, the rapid development of nanoscience has extensively changed the world with the advent of space age materials to the small chips that support artificial intelligence. Still, there is much further to go, especially in the field of soft nanotechnologies, where materials are grown and self-assembled with complex, weak interactions. In 1959, Feynman presented his classic talk *There's Plenty of Room at the Bottom* at the annual meeting of the American Physical Society. He mentioned an idea from his PhD student, Albert Hibbs, that one day we might swallow our surgeons [1]. He was referring to ingestible nanomachines that could swim through bodies and perform precise surgical procedures. Sixty years later, the realisation of these nanomachines remains in the distant future, but the recent development of molecular motors and stimuli-responsive materials in integrated systems is a significant step towards this goal. The pursuit of these nanomachines remains a research topic of great interest in the many scientific communities [2].

In nature, nanomachines control cellular functions in all organisms. For example, motor proteins can transport materials throughout cells and work in unison to cause larger scale actuation for muscle contraction. These motor proteins are powered with the chemical potential of adenosine triphosphate (ATP), which is carefully regulated by a complex cascade of cellular nanomachine interactions [3]. For artificial actuators, a much simpler controllable power source is desired. Promising alternatives include pH, temperature, and light. For many applications, light-driven actuators are preferred, because they can be easily controlled remotely with high spatial and temporal resolution. This work aims to examine the behaviours of simple artificial nano-actuators that consist of plasmonic nanoparticles coated with thermoresponsive polymer shells. These nanoparticles are called actuating nanotransducers (ANTs).

The ANTs discussed throughout this thesis are soft-plasmonic composites. They consist of a heterogeneous mixture of soft and plasmonic materials. Soft matter is a subclass of condensed matter that encompasses fluids, colloids, gels, and many other materials that can be deformed easily with external stresses or thermal fluctuations. Plasmonic materials are metals that can support the collective oscillations of electrons

when excited by an electromagnetic field. These collective oscillations are called plasmons.

The plasmonic properties of metal structures are highly sensitive to changes in shape, size, refractive index, and their proximity to other plasmonic structures [4]. Their tunability makes them enticing materials for photonic applications. The plasmonic response of metals, both in frequency and amplitude, is proportional to the number density of conductive electrons as described in more detail in this chapter. As a result, noble metals with high electron number densities, such as gold (Au) and silver (Ag), are commonly used plasmonic materials. Remarkable advances in lithography and nanoparticle synthesis have allowed for the preparation of gold and silver nanoparticles in different shapes and sizes, tuning their optical properties across the visible spectrum [5, 6]. However, once synthesised, it is challenging to tune the optical properties of the nanoparticles, especially reversibly. This constrains their application in photonic devices.

The integration of soft materials that readily change refractive index, shape and size, such as stimuli-responsive polymers, with plasmonic materials, allows for the design of tunable optical systems. Inversely, with the appropriate selection of soft material, optically controlled nanoscale actuators are realised via plasmonic heating-induced structural changes.

1.1 Outline

This initial chapter discusses the fundamentals of light interactions with plasmonic nanoparticles and the basic principles of thermoresponsive polymers. It builds the base for understanding the dynamic light-responsive behaviours of ANTs. It begins with the fundamental interactions of light and plasmonic nanoparticles to generate colour and localise heating on the nanoscale. Thermoresponsive polymers are then introduced to describe sharp phase transitions with temperature that elicit mechanical actuation on the nanoscale. Finally, the relevant forces on the nanoscale are presented, as they play a key role for the understanding of the behaviours of ANTs in the various systems explored in this thesis.

Chapter 2 covers the switchable optical and physical properties of gold nanoparticles coated with thermoresponsive polymers. Recent studies in the field and current

applications of these composite particles are highlighted. In addition, the ANTs are characterised and their reversible self-assembly behaviour in aqueous media is discussed.

Chapter 3 is the experimental section of this thesis. It presents the preparation procedures for ANT particles along with the various substrates used in forming different ANT systems. In addition, the optical techniques and experimental setups used to both control and characterise the behaviour of the ANT systems are described.

Chapter 4 investigates the underlying mechanisms driving the reversible assembly and disassembly of the ANTs. The optical properties of ANT clusters are modelled to distinguish their internal particle distributions. The effects of polymer functionalisation, concentration, and solution ionic strength are examined. It is found that these factors are responsible for the multi-stable nano-configurations observed in ANT self-assembly.

Chapter 5 discusses the temperature and light response of ANT particles in the Nanoparticle on Mirror (NPoM) geometry. This plasmonic structure is designed for the simultaneous probing and actuation of ANTs with light, and enables the mechanical characterisation of individual particles. Large forces, > 0.3 nN, are observed with fast (sub-ms) switching times, and stroke lengths on the order of 10 nm.

Chapter 6 investigates the unusual behaviours of dense ANT particle thin-films. These plasmonic films exhibit interesting optical behaviours arising from the macroscale effective medium response of the film and the microscopic interactions of the gold nanoparticles within. They are thermally switched on large-scale areas with bulk heating or locally with focused light. In addition, they exhibit interesting thermomechanical and thermofluidic dynamics in response to local light-induced heating.

Chapter 7 describes the behaviour of ANTs encapsulated in microdroplets. The confinement of the particles within microscale volumes alters their response to temperature. The microdroplets behave like artificial chromatophores, which are able to disperse and localise pigments to drastically change their optical properties. Furthermore, they exhibit optically driven locomotion from light-induced heating effects.

Chapter 8 recapitulates the key results and conclusions, and highlights interesting future directions stemming from the work discussed in the previous chapters.

1.2 Light Interactions with Metal Nanoparticles

Light consists of self-propagating electromagnetic fields that interact diversely with materials and are visible to the eye. The interaction of light with plasmonic nanoparticles is interesting, because these particles can enhance optical fields on the nanoscale, and they have tunable optical properties. In metals, these properties are predominantly dictated by the interactions between light and electrons. Since metals are conductive, some of their electrons are effectively de-localised throughout the material. These electrons can be collectively modelled as a sea of free electrons that can move in waves on the surface of the metal. This is the basis for the Drude model, which is commonly used to approximate the optical properties of metals.

Under an external electric field \mathbf{E} a force is applied on the electrons. Their motion \mathbf{x} over time t is described by the general wave equation for a harmonic oscillator [4]

$$m^* \frac{d^2 \mathbf{x}}{dt^2} + m^* \gamma \frac{d\mathbf{x}}{dt} = -e\mathbf{E}, \quad (1.1)$$

where m^* is the effective mass of the electrons, γ is the damping coefficient of the electron oscillations, and e is the electron charge constant. For the case of excitation by light, the external field \mathbf{E} is described by the time varying oscillating component $\mathbf{E} = \mathbf{E}_0 \exp\{-i\omega t\}$ where ω is the frequency. The displacement of the electrons on a gold particle is depicted in Figure 1.1. A particular solution of this equation in the form $\mathbf{x} = \mathbf{x}_0 \exp\{-i\omega t\}$ results in the following relation

$$\mathbf{x} = \frac{e}{m^*(\omega^2 + i\gamma\omega)} \mathbf{E}. \quad (1.2)$$

As the electron density shifts to either side of the nanoparticles an electric dipole is formed that oscillates with frequency ω . The dipole moment of the nanoparticle with an electron density number N (the number of electrons per unit volume) is described by its polarisation \mathbf{P} , where

$$\mathbf{P} = -N e \mathbf{x} = \frac{N e^2}{m^*(\omega^2 + i\gamma\omega)} \mathbf{E}. \quad (1.3)$$

The dielectric function, ε , is the relative permittivity of a material and is defined from the ratio of polarisation to external field. It is commonly used to describe the light-matter interactions and relates to the refractive index, n , of non-magnetic

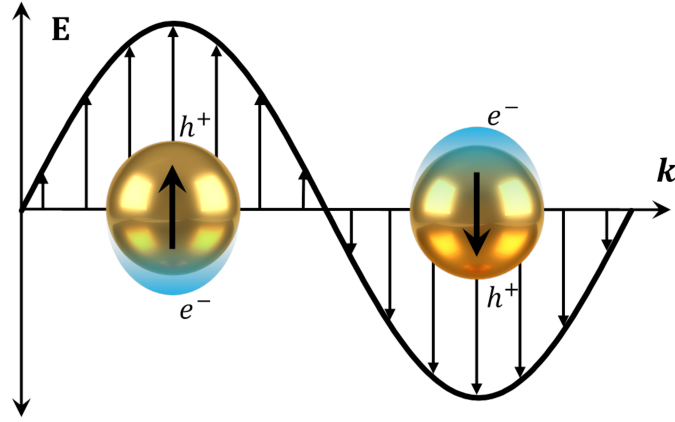


Fig. 1.1 Schematic of conductive electron displacement on gold nanoparticles when excited by an electromagnetic field. The collective oscillation of the electrons e^- on the surface of nanoparticles is indicated with the translucent blue particle projection. The corresponding electron vacancies, or holes h^+ , are also labelled. The arrows denote the induced dipole orientation of the nanoparticles.

materials by $n = \sqrt{\varepsilon}$. The frequency-dependent component of the dielectric function of free electrons is

$$\varepsilon(\omega) = 1 + \frac{\mathbf{P}}{\varepsilon_0 \mathbf{E}}, \quad (1.4)$$

where ε_0 is the permittivity of free space. Substituting Equation 1.3 into Equation 1.4 gives

$$\varepsilon(\omega) = 1 - \frac{\omega_p^2}{\omega^2 + i\gamma\omega}, \quad (1.5)$$

where the characteristic plasma frequency ω_p is

$$\omega_p = \sqrt{\frac{Ne^2}{\varepsilon_0 m^*}}. \quad (1.6)$$

In order to account for the effects of the bound electrons on the dielectric function, the constant ε_∞ is introduced [7]. This gives the total dielectric function

$$\varepsilon = \varepsilon_\infty - \frac{\omega_p^2}{\omega^2 + i\gamma\omega}. \quad (1.7)$$

This is the Drude model for the dielectric function of metals. For real materials $\gamma > 0$, hence the permittivity is complex with $\varepsilon = \varepsilon' + i\varepsilon''$. The modelled real and

imaginary components of the dielectric function of gold are compared with experimental data from Johnson and Christy in Figure 1.2 [8].

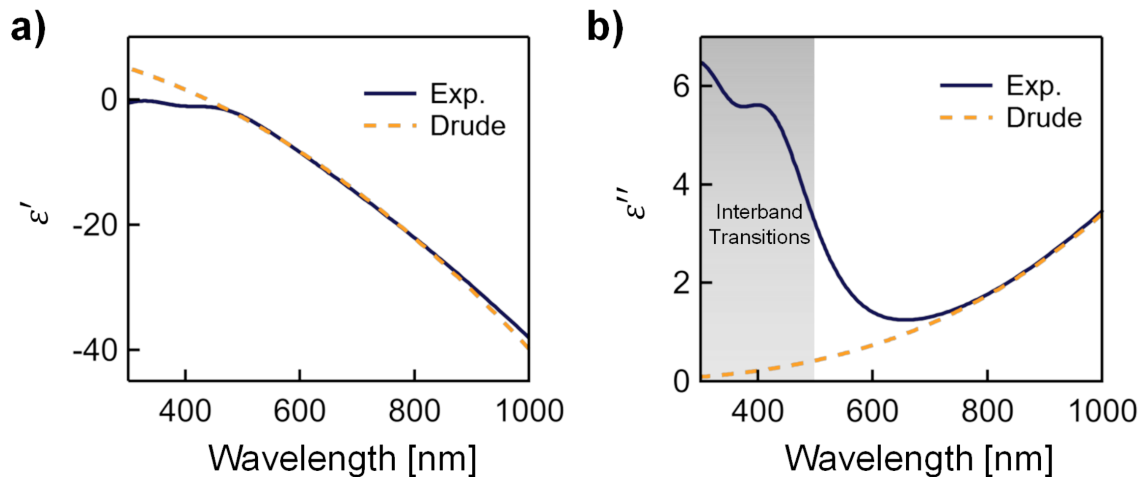


Fig. 1.2 Comparison of the dielectric function of gold according to the Drude model with experimental results from Johnson and Christy [8]. a) The real and b) imaginary components of the dielectric function of gold. The Drude model parameter values are $\lambda_p = \frac{2\pi c}{\omega_p} = 142$ nm, $\epsilon_\infty = 9.5$, and $\gamma = 1.3 \times 10^{14}$ s $^{-1}$ for gold.

The real part of the dielectric function in the Drude model agrees well with experiment at visible wavelengths $\lambda > 500$ nm (Figure 1.2a). For $\lambda < 500$ nm, there is a discrepancy which is caused by the interband transitions of gold. The effect of these transitions is more dominant in the imaginary part of the dielectric function (Figure 1.2b). Gold has particularly small interband separations due to large relativistic effects, which raise the **5d** electron energies and lower the energies of the valence **6s** electrons [9]. These relatively low energy interband transitions are responsible for the absorption of blue light, giving gold its characteristic yellow lustre. In general, the Drude model serves as a good approximation of the optical properties of the plasmonic materials. However, since it does not account for interband transitions, it only agrees well for $\lambda > 500$ nm for gold.

1.2.1 Localised Surface Plasmon Polaritons

Plasmonic nanoparticles support localised surface plasmon polaritons (LSPPs). LSPPs are collective, coherent oscillations of electrons on the surface of metallic nanostructures.

They occur at specific frequencies based on the polarisability of the particles, which is highly sensitive to size, shape, material, and proximity to other plasmonic surfaces.

The origin of LSPP resonances in spherical metal nanoparticles can be analytically derived for spheres that are much smaller than the wavelength of light ($R \ll \lambda$). Under this condition, the external field is approximately uniform across the nanoparticle such that the particle can be modelled as an oscillating electromagnetic dipole. The polarisability, α , of a spherical nanoparticle with radius R is

$$\alpha = 4\pi R^3 \frac{\varepsilon - \varepsilon_m}{\varepsilon + 2\varepsilon_m}, \quad (1.8)$$

where ε and ε_m are the dielectric functions of the nanoparticle and the surrounding medium, respectively [10]. For metals, ε is negative while ε_m is usually positive. This results in the plasmonic resonance condition $\varepsilon = -2\varepsilon_m$ at which LSPPs are excited. The polarisability of nanoparticles is related to their scattering, extinction, and absorption cross-sections, σ , by

$$\sigma_{\text{scat}} = \frac{k^4}{6\pi} |\alpha|^2, \quad (1.9)$$

$$\sigma_{\text{ext}} = k \text{Im}(\alpha), \quad (1.10)$$

and

$$\sigma_{\text{abs}} = \sigma_{\text{ext}} - \sigma_{\text{scat}} = k \text{Im}(\alpha) - \frac{k^4}{6\pi} |\alpha|^2, \quad (1.11)$$

where k is the wavenumber, which depends on the wavelength of light with the relationship $k = \frac{2\pi n}{\lambda}$ [10]. Notably, σ_{scat} scales with R^6 , whereas σ_{abs} only scales with R^3 . Therefore, absorption dominates for smaller particles, while scattering is more efficient for larger particles. These equations define the optical response of nanoparticles. In transmission, the resonance condition of the polarisability gives a bright red colour to gold nanoparticle suspensions as shown in Figure 1.3.

The polarisation of spheres described in Equation 1.8 indicates ways to tune the colour of the nanoparticles. The resonance can be tuned by changing the dielectric functions of the nanoparticle or its surrounding medium, i.e. the materials. It is also well known that changing the shape of nanoparticles significantly affects their resonance frequency. Unfortunately, analytical models for the polarisation of nanoparticles only exist for very simple geometries. The polarisation of more complicated geometries must currently be solved with numerical methods.

As shown in Figure 1.3b, the resonance dependency on particle size is not captured within the approximation that $R \ll \lambda$. The redshift in resonance and peak broadening

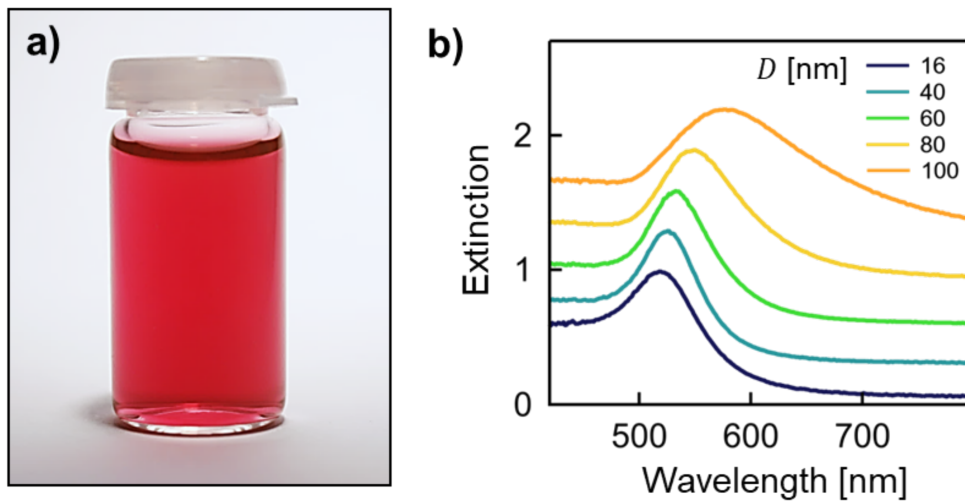


Fig. 1.3 Plasmonic gold nanoparticles in suspension. a) Photograph of red 60 nm gold nanoparticles in a glass vial. b) Extinction spectra of gold nanoparticle suspensions with diameters, D , varying from 16 to 100 nm.

with increasing size is caused by retardation effects. The larger particles experience greater phase delays since the dipole surface charges are further separated [11]. Conveniently, the plasmon frequency can also be tuned without changing the size or shape of the particles by controlling their separation distance.

1.2.2 Plasmonic Coupling Between Nanospheres

Plasmonic nanoparticles in close proximity interact strongly. The effects of plasmonic coupling is most simply demonstrated between two identical nanoparticles that form a dimer. Similar to molecular orbital hybridisation, their interaction creates new hybridised modes that resonate at different energies as illustrated in Figure 1.4.

Out of the two hybrid modes depicted, only the ‘bright’ mode can be excited with light because it is overall dipolar [12]. In addition, higher order ‘bright’ modes exist, but they are generally outside the visible energy range and have lower quantum efficiencies. Therefore, their contribution to the optical properties of ANT systems discussed in later chapters is negligible.

An interesting feature of plasmonic coupling is the high sensitivity of the resonance wavelength to the spacing between particles. The resonance redshifts as the spacing decreases. The weak coupled mode overlaps the single particle mode at $\lambda = 530$ nm when the gap, r , is greater than 20 nm. For smaller separations, the coupled mode

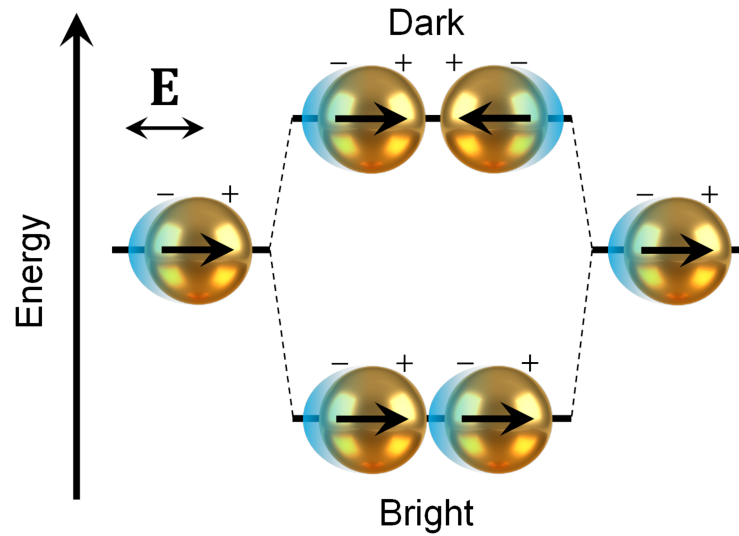


Fig. 1.4 Schematic of coupled modes and relative energies in the hybridisation model for a plasmonic dimer under an exciting optical field \mathbf{E} polarised parallel to the dimer axis.

is strongly redshifted and both the single particle and dimer modes are spectrally resolved, as simulated in Figure 1.5a.

Another notable characteristic of plasmonic coupling is the strong, confined field-enhancement that occurs in the gap. The calculated near-field distributions of intensity enhancement for 10 and 3 nm particle separations are shown in Figure 1.5b. The enhancement is greatly increased for smaller gap sizes.

So far only dimers have been discussed. The addition of other nanoparticles to form larger interacting chains or clusters discretely generates new ‘bright’ modes with lower energy states. Hence, larger nanoparticle assemblies typically have further redshifted coupled modes. This ability to tune optical properties by controlling the number and relative position of coupled plasmonic particles is commonly used in ANT systems.

1.2.3 Plasmonic Nanoparticle Heating

Both single-particle and coupled modes have absorption cross-sections. The absorption cross-section relates to the non-radiative decay of excited plasmons, which generates heat. For nanoparticles, this process can rapidly generate large temperature gradients across nanoscale volumes [14, 15].

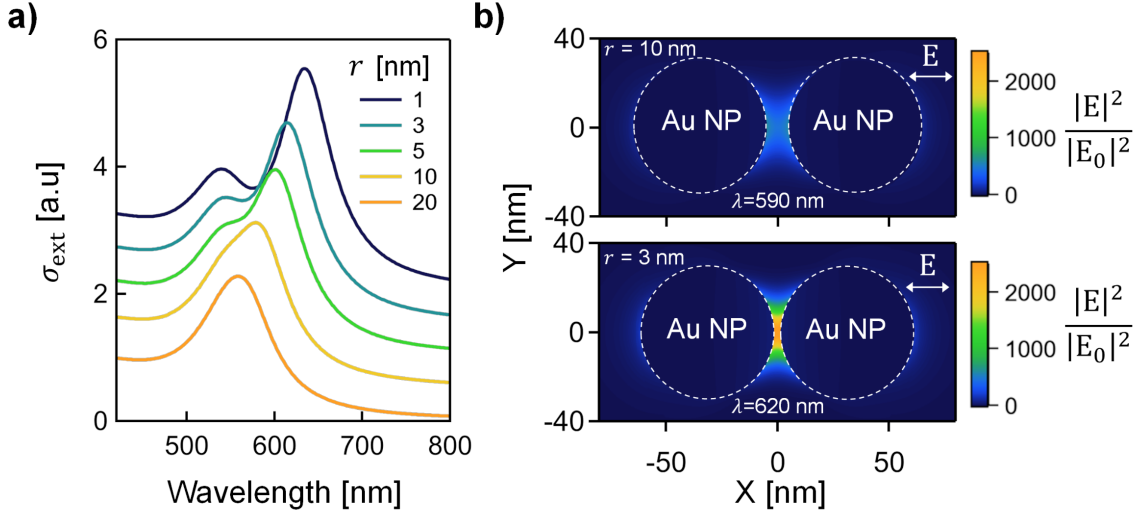


Fig. 1.5 Optical properties of plasmonic dimers. a) Extinction cross-section, σ_{ext} , of dimers as a function of separation distance, r . The spectra are vertically offset by 0.5. b) Near-field intensity enhancement with separation distances fixed to 10 and 3 nm. The optical properties are calculated with a T-matrix solver by Mackowski and Mishchenko for 60 nm gold dimers in water ($n = 1.33$) [13].

The absorption process consists of three steps, which are observed in short-pulse laser excitation experiments. First, the laser pulse is partially absorbed by the conduction electrons on the nanoparticle. This increases their temperature and they quickly thermalise over a time scale of ≈ 100 fs via electron-electron scattering [16]. Then, the excited electrons scatter off lattice sites and excite phonons, which thermalise, through electron-phonon and phonon-phonon interactions, over the time scale of ≈ 1.7 ps for gold [17]. Finally, the nanoparticle is approximately heated uniformly and the heat dissipates into the surrounding medium. The rate of this final step depends on the size of the particles and the thermal conductivity of the medium [18]. Under CW irradiation, these processes occur concurrently and the characteristic timescale, τ , for cooling of a spherical nanoparticle with a radius R is given by the following expression

$$\tau = \frac{R^2 C_{NP}^2}{9C_m \Lambda_m}, \quad (1.12)$$

where C_{NP} and C_m are the heat capacities (per unit volume) of the nanoparticle and the surrounding medium, and Λ_m is the thermal conductivity of the surrounding medium [19]. For particles ranging in size from 16 to 100 nm in diameter, this gives expected temperature switching rates on the order of ≈ 100 ps. This fast switching is ideal for rapidly inducing local temperature gradients around plasmonic particles.

For metal nanoparticles in aqueous solutions, the thermal conductivity of the particle is typically much larger than that of the surrounding liquid ($\kappa \gg \kappa_m$). Under this condition, it can be approximated that the particle has a uniform steady state temperature, while the temperature profile in the surrounding medium is a function of the distance, r , away from the particle surface. The profile around the nanoparticle under constant illumination at steady state can be solved analytically from the heat diffusion equation

$$\frac{1}{r^2} \frac{\partial}{\partial r} \left[\kappa r^2 \frac{\partial T}{\partial r} \right] = -q. \quad (1.13)$$

Note that the thermal conductivity, κ , and the generated heat, q , are functions of distance r . For $r \leq R$, $\kappa = \kappa_{NP}$ and $q \neq 0$, and for $r > R$, $\kappa = \kappa_m$ and $q = 0$, as light is only absorbed by the nanoparticle. Considering the conservation of energy, the heat generation in the nanoparticle must be normalised by the total power absorbed Q which is the product of the absorption cross-section of the particle, σ_{abs} , and the light intensity, I , [20]

$$Q = \int_V q(r) dV = \sigma_{\text{abs}} I. \quad (1.14)$$

Using the total power absorbed, Baffou et al. derived an analytical expression for the change in temperature, ΔT_{NP} , of the nanoparticle under continuous irradiation [18]. Here, the nanoparticle temperature during constant irradiation is $T(r) = T_0 + \Delta T(r)$, where T_0 is the initial temperature and

$$\Delta T_{\text{NP}} = \frac{Q}{4\pi\kappa_m R}. \quad (1.15)$$

Using the approximation that the thermal conductivity of the nanoparticle is much higher than that of the surrounding medium, the following steady state temperature profiles are found for two cases: (1) when $r \leq R$ and (2) when $r > R$ [18], giving

$$\Delta T(r) = \begin{cases} \Delta T_{\text{NP}}, & r \leq R \\ \Delta T_{\text{NP}} \frac{R}{r}, & r > R. \end{cases} \quad (1.16)$$

The modelled temperature profile for a gold particle in an aqueous solution under CW irradiation at $\lambda = 532$ nm is shown in Figure 1.6. The temperature change in the

surrounding medium is half that of the nanoparticle at a distance of $r = 2R$, hence R away from the particle surface.

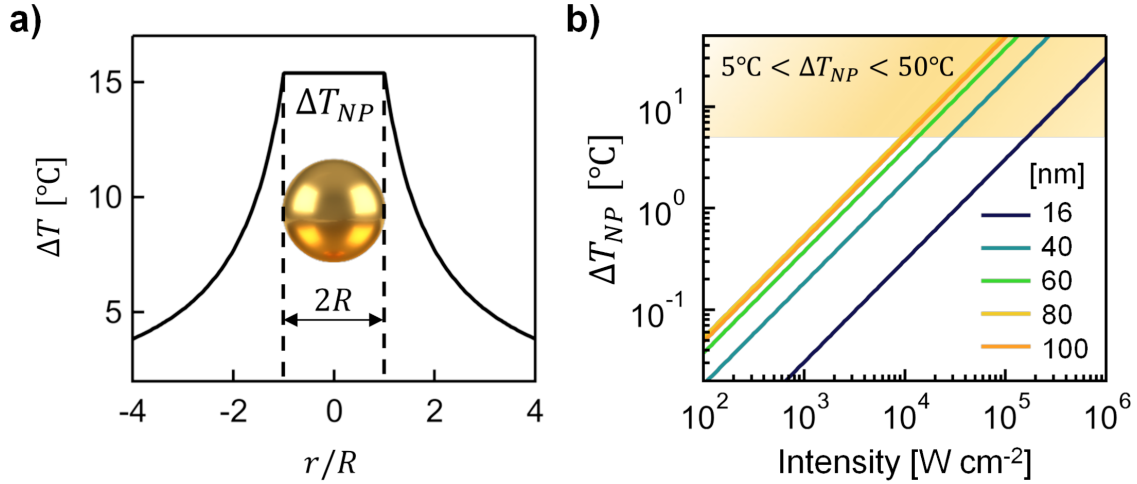


Fig. 1.6 Local plasmonic heating of gold nanoparticles in aqueous solution. a) Steady state radial temperature profile of a particle in solution with radius R . The calculation uses the parameters $\lambda = 532$ nm, $I = 5 \times 10^5$ W cm $^{-2}$, $\kappa_m = 0.61$ W m $^{-1}$ K $^{-1}$, and $R = 8$ nm. b) Particle temperature as function of light intensity for particle diameters ranging from 16 to 100 nm. The ΔT region 5°C to 50°C highlights a practical range for heating the surrounding aqueous solution by few degrees above the ambient temperature without generating vapour.

As previously discussed, the absorption cross-section also depends on the radius, R , of the particle. Larger nanoparticles absorb significantly more light than smaller particles. For comparison, a single 100 nm particle absorbs an order of magnitude more intensity than a single 16 nm particle. However, there are diminishing returns with size for the larger particles. This is evident from the negligible difference in heating between the larger 80 and 100 nm particles in Figure 1.6b.

Considerable power is required for heating local volumes by a few degrees around well-dispersed nanoparticles in aqueous solution ($\approx 10^4$ W cm $^{-2}$ for 100 nm particles). Typically, the ideal range of heating to drive thermal processes surrounding the nanoparticles, such as the switching of thermoresponsive materials, is ΔT_{NP} from 5°C to 50°C. Lower temperatures may be inadequate for switching or only result in partial switching, while higher temperatures can generate steam or damage the polymer or particle. Of course, this temperature range is subject to the initial temperature bias of the medium.

For plasmonic particle applications, it is very common to have the surface of the nanoparticles coated with ligands for stabilisation effects in liquid suspensions or to introduce other specific functionalities. Surface ligands or shells can affect the temperature profile around the particles. If there is a sufficient discrepancy between the thermal conductivities of the shell material and the surrounding medium, then the analytical temperature profile from Equation 1.16 must be re-written as

$$\Delta T(r) = \begin{cases} \frac{Q}{4\pi} \left(\frac{1}{\kappa_1 R_1} + \frac{1}{\kappa_2 R_2} - \frac{1}{\kappa_1 R_2} \right), & r \leq R_1 \\ \frac{Q}{4\pi} \left(\frac{1}{\kappa_1 r} + \frac{1}{\kappa_2 R_2} - \frac{1}{\kappa_1 R_2} \right), & R_1 < r \leq R_2 \\ \frac{Q}{4\pi \kappa_2 r}, & r > R_2, \end{cases} \quad (1.17)$$

where R_1 and R_2 are the radii of the particle and shell, respectively, while κ_1 and κ_2 are the thermal conductivities of the shell and the surrounding medium [18]. Interestingly, differences on the order of a factor of 2 between the shell and medium conductivities result in significant changes for ΔT_{NP} , but no change of the heat profile in the surrounding solution (Figure 1.7). Considering the conservation of energy, this result agrees well, since the heat flux in and out of the particle must remain constant regardless of the shell's conductivity.

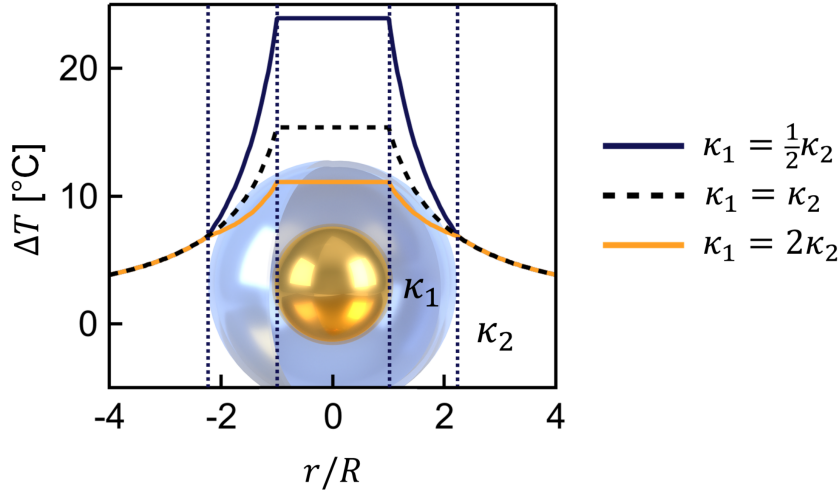


Fig. 1.7 Steady state radial temperature profile of core-shell nanoparticles with gold cores and shells with different thermal conductivities from the surrounding media. The parameters $\lambda = 532 \text{ nm}$, $I = 5 \times 10^5 \text{ W cm}^{-2}$, $\kappa_1 = 0.61 \text{ W m}^{-1} \text{ K}^{-1}$, and $R = 8 \text{ nm}$ were used to generate this profile.

The shell can play a much more significant role in the temperature profile by affecting the plasmonic properties. From Equations 1.8 and 1.11, it is evident that changes in the dielectric function, ϵ_m , surrounding the particle can shift the plasmon absorption and greatly affect the overall heating. Similarly, the emergence of plasmonic coupled modes between multiple nanoparticles in close proximity can drastically change the plasmonic absorption.

1.3 Stimuli-responsive Polymers

Stimuli-responsive materials are soft materials that have dynamic properties altered by changes in the external environment. The external stimuli can be light, temperature, pH, ionic strength, and electric or magnetic field. Depending on the material, the response can vary as well [2, 21]. For example, common responses are changes in colour and solubility. Stimuli-responsive materials have gathered a lot of interest from various industries and scientific communities due to their innate ability to provide dynamic functionality to nano-/microsystems [22].

Thermoresponsive polymers are a particularly interesting class of stimuli-responsive materials. They typically undergo phase transitions with small changes in temperature. The phase transitions can thermodynamically change the interaction potential between polymers and their solvents, causing significant expansion and contraction of the polymers. Poly(N-isopropylacrylamide) (PNIPAM) is particularly interesting because it is biocompatible and undergoes a phase transition near physiological temperatures [23]. For this reason, PNIPAM is one of the most studied stimuli-responsive polymers and is used as a model thermoresponsive polymer for the ANT systems presented in this work.

1.3.1 Lower Critical Solution Temperature

The lower critical solution temperatures (LCST) marks the temperature at which mixtures are miscible for all compositions. Below the LCST, a mixture will form a single phase, while above the LCST, depending on the composition, the mixture can separate into multiple phases. Usually, mixtures will separate into two phases. The miscibility of the mixture depends on the change in Gibbs free energy of mixing, ΔG_{mix} , where [24]

$$\Delta G_{\text{mix}} = \Delta H_{\text{mix}} - T\Delta S_{\text{mix}}. \quad (1.18)$$

The change in free energy takes into account both the differences in enthalpic, ΔH_{mix} , and entropic, ΔS_{mix} , energy contributions. The enthalpic term accounts for the difference in molecular interaction energies between miscible and immiscible states. It is comprised of the differences in monomer-monomer, monomer-solvent, and solvent-solvent interactions between the two states. Whereas, the entropic term accounts for the change of entropy of the mixture.

Mixing is spontaneous when $\Delta G_{\text{mix}} < 0$. In general, mixing increases entropy ($\Delta S_{\text{mix}} > 0$), which implies that mixtures are more miscible at higher temperatures. This gives rise to upper critical solution temperatures (UCSTs), which marks the upper limit of temperature that the mixture is partially insoluble for all compositions.

In 1941, the free energy of mixing for long polymers was solved independently by Flory and Huggins [25, 26]. The Flory-Huggins solution theory is a thermodynamic model of polymer solutions which adapts the entropy of mixing to account for the typically drastic size difference between polymer chains and solvent molecules. The mixing energy depends on the volume fraction of the polymer, Φ , and degree of polymerisation, N , with the relation

$$\Delta G_{\text{mix}} = k_B T \left[\chi \Phi (1 - \Phi) + \frac{\Phi}{N} \ln (1 - \Phi) + (1 - \Phi) \ln \Phi \right], \quad (1.19)$$

where k_B is the Boltzmann constant and χ is the Flory parameter. Generally, χ is non-linearly dependent on temperature [23]. This dependency can vary greatly between polymers with different monomer units, structures, and molecular weight. It is normally fitted to measured solution phase transitions with analytical models.

Although, the properties of PNIPAM have been studied extensively, significant variations in the phase diagrams have been reported [23]. The consensus is that the critical transition temperature, T_c , is approximately 32°C, but this temperature varies by a few degrees depending on the synthesis procedure. The T_c can also be tuned by introducing other monomers in the PNIPAM chains to form copolymers [27, 28]. Jain et al. demonstrated that it can be tuned from 25°C to 55°C by varying ratios and types of ionic liquid monomers in PNIPAM copolymers [29].

Unlike other acrylamide polymers, the T_c of PNIPAM is consistent over a large range of solution volume fractions, Φ . In addition, there is negligible variation in T_c

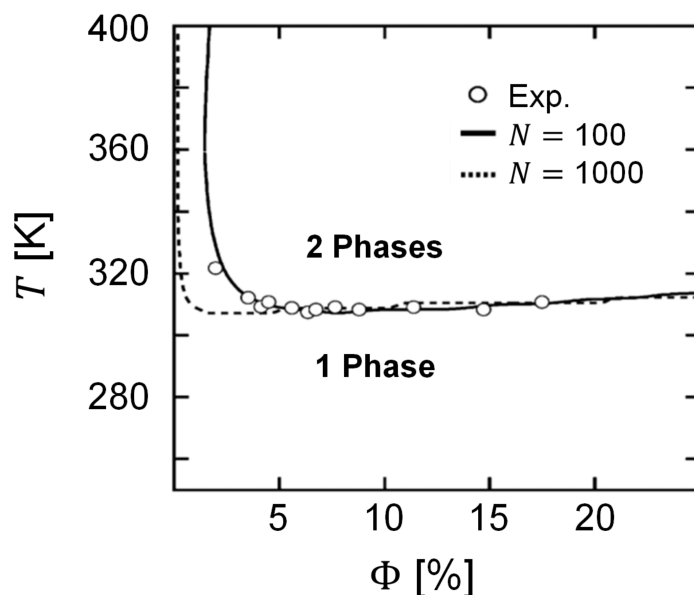


Fig. 1.8 A modelled phase diagram for PNIPAM compared with experimental data. a) Modelled spinodal curve for PNIPAM with degrees of polymerisation fixed to $N = 100$ and $N = 1000$. The experimental data are from Gomes de Azevedo et al. [31]. This is a modified figure from Okada and Tanaka [30].

with molecular weight. This is surprising given that most polymers have increasing transition temperatures with molecular weight. Very few theories have emerged to explain this phenomenon, but Osaka et al. have proposed that cooperative hydration of PNIPAM chains can explain this property (Figure 1.8) [30]. This is based on the formation of favourable hydrogen bonding networks over extended stretches along the chains.

The phase diagram indicates the T_c where the PNIPAM undergoes a phase transition. The transition is reversible and changes the polymer configuration between extended coil and globule states, below and above T_c respectively. These configurations are depicted in Figure 1.9a. The changes in mean radius of gyration, $\langle R_g \rangle$, and radius of hydration, $\langle R_h \rangle$, with temperature demonstrate the sharp transition at 32°C and significant change in size with a factor of ≈ 6.3 (Figure 1.9b). The transition is driven by alterations to the hydrogen bonding of the PNIPAM amide groups. Below T_c , hydrogen bonds are preferably formed with the surrounding water molecules, while above T_c the intrachain hydrogen bonds between amide groups are favoured. This leads to an increase in the hydrophobicity of PNIPAM above T_c [32].

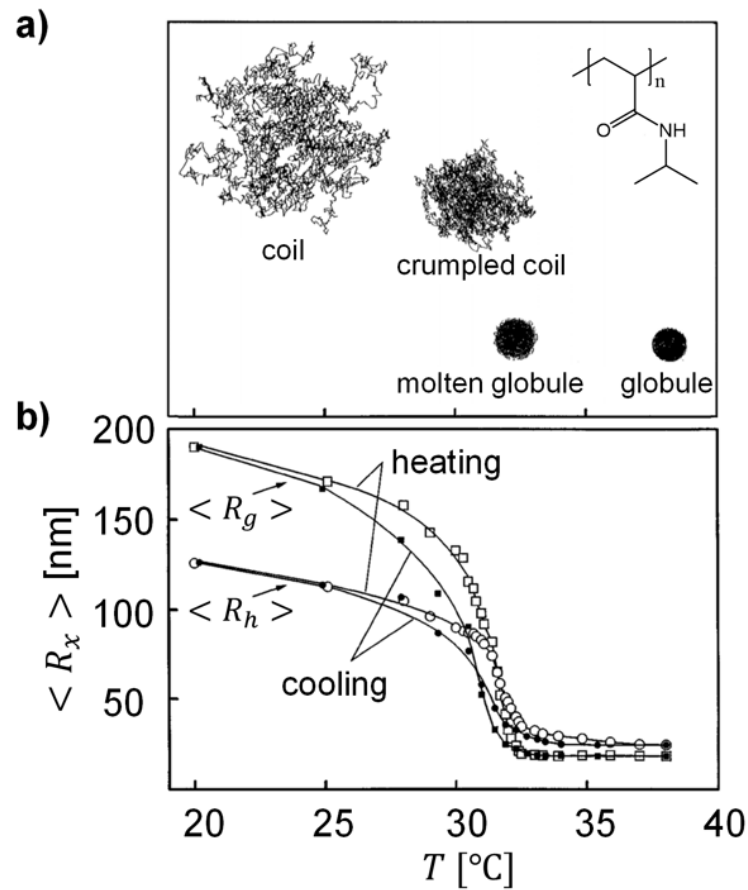


Fig. 1.9 Transitions of single PNIPAM chains ($M_W = 1.3 \times 10^7 \text{ g mol}^{-1}$) between the coil and globule states. a) Schematic of thermodynamically stable states of a single homopolymer chain in the coil-to-globule and globule-to-coil transitions. The molecular structure of the polymer with n repeat units is shown in the inset. b) Mean radius of gyration, $\langle R_g \rangle$, and radius of hydration, $\langle R_h \rangle$, in response to heating and cooling above and below T_c . This figure is adapted from Wu et al. [33].

The reversible coil-to-globule transition is an intramolecular phase transition that does not involve interchain interactions, hence can only be studied at low concentrations [33]. At higher concentrations, the PNIPAM chains form aggregates mediated by interchain hydrogen bonding. The formation of these aggregates increases the turbidity or cloudiness of solutions when heated above T_c . This cloud point coincides with the T_c , as shown in the extinction of the PNIPAM solution in Figure 1.10. Here, the measured cloud point agrees well with the literature values for the T_c of PNIPAM.

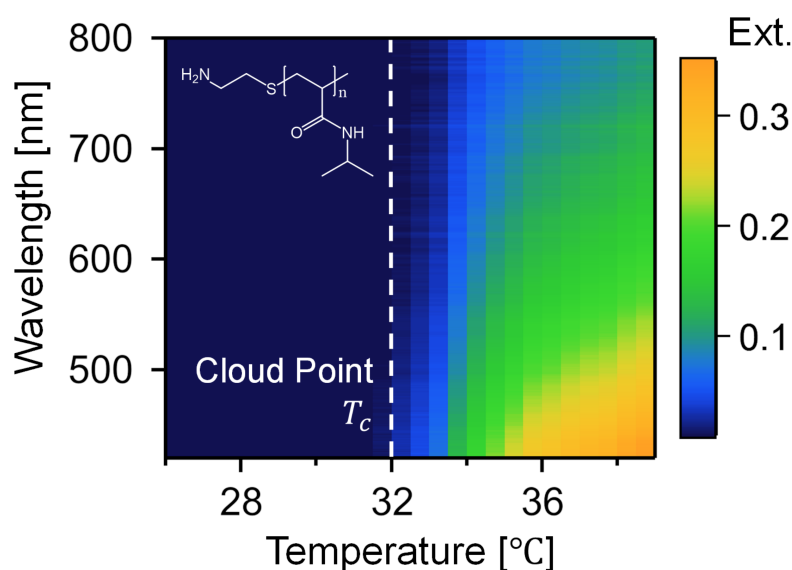


Fig. 1.10 Extinction spectra map of a 20 μM amine-terminated PNIPAM (5.5 kDa, molecular structure is shown in the inset) aqueous solution during heating. The solution cloud point at 32°C indicates the critical solution temperature T_c of the polymer. A 2 min. equilibration time was used for each temperature step.

The reversible swelling and de-swelling of the PNIPAM with temperature can apply mechanical forces and move objects on the nanoscale. In addition, the interchain interactions enable the reversible self-assembly of colloids in aqueous solutions [34]. To further understand these behaviours, the relevant forces on the nanoscale must be considered.

1.4 Forces on the Nanoscale

The interparticle forces between colloids in solution are well described by extended DLVO theories. The DLVO theory is named after Derjaguin, Landau, Verwey, and

Overbeek [35, 36]. It predicts the interaction potentials between objects with nanoscale separations by combining the van der Waals, U_{vdW} , and coulombic, U_{Coulomb} , interactions [37],

$$U_{\text{tot}} = U_{\text{Coulomb}} + U_{\text{vdW}}. \quad (1.20)$$

The total interaction potential, U_{tot} , between two identical spherical colloids with radius R can be described analytically. Beginning with the electrostatic interaction, the repulsion between two identical spherical colloids at a distance r between the two surfaces is [38]

$$U_{\text{Coulomb}}(r) = \frac{1}{2} RZ \exp(-\kappa r). \quad (1.21)$$

The interaction constant Z is given by

$$Z = 64\pi\epsilon_0\epsilon \left(\frac{k_B T}{e} \right)^2 \tanh\left(\frac{ze\psi_0}{4k_B T} \right), \quad (1.22)$$

and κ is the inverse of the Debye screening length, λ_D , such that [39]

$$\kappa = \lambda_D^{-1} = \left[\frac{e^2 N_A (1000 \times 2I_{\text{ion}})}{\epsilon_0 \epsilon k_B T} \right]^{\frac{1}{2}}. \quad (1.23)$$

Here, ψ_0 is the surface charge of the colloids, e is the electron unit charge, N_A is Avogadro's number, and $I_{\text{ion}} = \frac{1}{2} \sum c_i z_i^2$ is the ionic strength of the solution. The ionic strength is a function of the molar concentration, c , and ion charge, z , for all ion species i in solution. For monovalent electrolyte solutions at room temperature ($T = 298$ K), the Debye length simplifies to

$$\lambda_D = \frac{1}{\sqrt{8\pi\lambda_B N_A (1000 \times I_{\text{ion}})}} = \frac{0.304}{\sqrt{I_{\text{ion}} [\text{M}]}} \text{ [nm]}, \quad (1.24)$$

where the Bjerrum length, $\lambda_B = \frac{e^2}{4\pi\epsilon_0\epsilon k_B T}$, defines the separation at which the electrostatic interaction between two elementary charges is comparable in magnitude to the thermal energy, $k_B T$. For aqueous solutions at room temperature, $\lambda_B \approx 0.7$ nm.

For identical colloids, $U_{\text{Coulomb}}(r)$ is always positive, as similarly charged colloids have repulsive electrostatic interactions. The repulsion is reduced by increasing the ionic strength of the solution or by reducing the surface charge of the particles. Added

ions in solution effectively screen the surface charge by forming an electrical double layer that consists of a layer of associated counter ions (Stern layer) and a diffuse layer of loosely interacting ions, as depicted in Figure 1.11a [40].

In contrast to the electrostatic contribution, the van der Waals interaction potential $U_{\text{vdW}}(r)$ is always negative, as induced dipole-dipole interactions are always attractive. The equation of the van der Waals interaction is [39]

$$U_{\text{vdW}} = -\frac{A_H}{6} \left[\frac{2R^2}{r^2 + 4rR} + \frac{2R^2}{(r + 2R)^2} + \ln \frac{r^2 + 4rR}{(r + 2R)^2} \right], \quad (1.25)$$

where the A_H is Hamaker constant. The Hamaker constant is defined as $A_H = \pi^2 C \rho^2$ for the interaction between identical materials, where C is the atom-atom pair interaction coefficient and ρ is the density of atoms in the material [38].

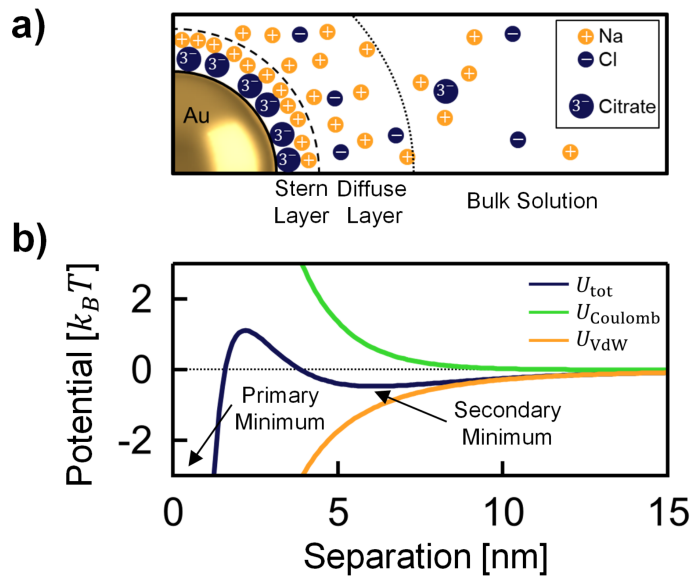


Fig. 1.11 Electrostatic and van der Waals interactions between two gold nanoparticles. a) Illustration of the ion distribution around a citrate-stabilised gold nanoparticle. b) Interaction potential between two gold particles in a monovalent electrolyte solution plotted with respect to the closest surface-to-surface separation distance. The parameters $T = 298$ K, $R = 8$ nm, $A_H = 3.8 \times 10^{-19}$ J, $\psi_0 = 100$ mV, $\kappa = 7.3 \times 10^8$ m $^{-1}$ are used to calculate these interaction potentials.

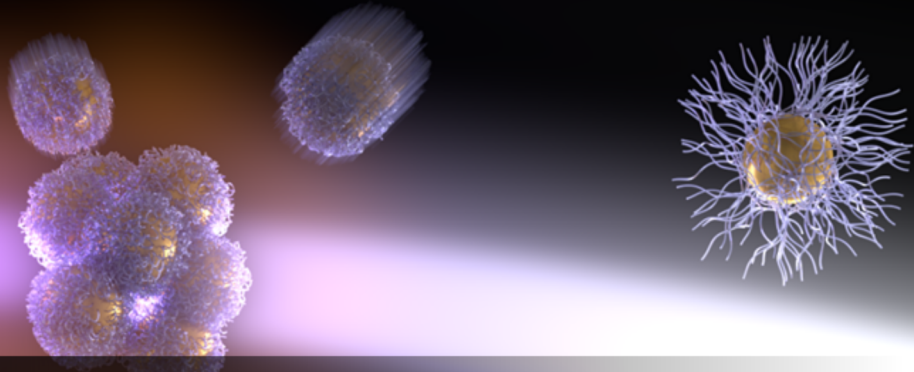
The combination of the electrostatic and van der Waals interactions results in different potential profiles for colloids in close proximity. Large positive potential barriers indicate that the particles are highly repulsive and will not aggregate. The

theory predicts that by regulating the colloid surface charges, thermally stable or metastable flocculation states can exist. For these states, an attractive potential well (at the secondary minimum) exists where the colloids are optimally positioned at set distances away from each other as shown in Figure 1.11b. They are very interesting for self-assembly processes because the colloids can reversibly arrange themselves at set distances from each other. If colloids happen to approach one another at very close distances, they can fall into the primary minimum potential well, which causes their irreversible aggregation.

DLVO theory is very useful for predicting the stability of colloids in solution. However, there are several other interactions between particles that are not accounted for in the theory, such as hydrophobic and steric effects. Steric effects from long, soluble ligands bound to colloids can sufficiently inhibit the irreversible aggregation of colloids without electrostatic repulsion by preventing their close approach. Other interactions include hydration forces, and the nuclear repulsion from the Pauli exclusion principle at sub-nm separations. These forces are included in extended DLVO theory models [41].

1.5 Summary

The fundamentals of light interactions with plasmonic particles and the thermoresponsive properties of PNIPAM were introduced in this chapter. Plasmonic systems allow for highly tunable photonic properties with changes in their environment, and stimuli-responsive polymers can readily change material properties with external stimuli. In particular, the thermoresponsive polymer PNIPAM undergoes a reversible coil-to-globule transition and forms aggregates above the critical temperature of $\approx 32^\circ\text{C}$. This aggregation of PNIPAM is caused by interchain hydrophobic and cohesive interactions. The aggregation behaviour of colloids is dictated by electrostatic and van der Waals interaction potentials, and other potentials as described by extended DLVO models. The following chapters use these principles to explain the interesting behaviours of ANTs which emerge from the synergistic interplay between plasmonic nanoparticles and PNIPAM.



2. Actuating Nanotransducers

In this chapter, the switchable properties of plasmonic particles coated with thin thermoresponsive shells are introduced. In particular, the dynamic response of composite materials that consist of interacting gold nanoparticles and the thermoresponsive polymer PNIPAM (Au@PNIPAM) are presented. This chapter draws from previous studies of ANT particles (as indicated in the text) and provides an overview of their known properties prior to the research discussed in the later chapters.

2.1 Au@PNIPAM Core-shell Nanoparticles

Au@PNIPAM nanoparticles are referred to as actuating nanotransducers (ANTs) because they convert light into mechanical force on the nanoscale. A schematic of the core-shell nanoparticles in the cold and hot state is shown in Figure 2.1. The high absorption cross-section of the plasmonic cores enables local light-induced heating. This triggers the shell phase transition and causes particles to approach within the attractive regime of the extended DLVO potential [42, 41]. Therefore, it induces their aggregation. Light-induced aggregation allows for interesting optical behaviours based on the interplay between the dynamic optical properties of ANT systems and the light that drives their transitions.

Au@PNIPAM core-shell particles have been studied with growing interest over the last decade [43]. Their tunable colour, hydrophobicity, and mechanical switching have been investigated for many research applications. Their change in shell hydrophobicity at physiological temperatures as been studied for catch and release systems for drug delivery [44–46]. In addition, this property has also been used to drive colloidal self-assembly [47–51]. Their optical effects have been used in the design of colorimetric sensors for temperature and pH [52, 53]. Also, the reversible change in size of the PNIPAM shell has been used for the switching of surface-enhanced Raman scattering (SERS) [54–56], as well as the development of colour displays [57–59] and fast mechanical actuation on the order of 10–100 ns for stroke lengths of ≈ 10 nm [60].

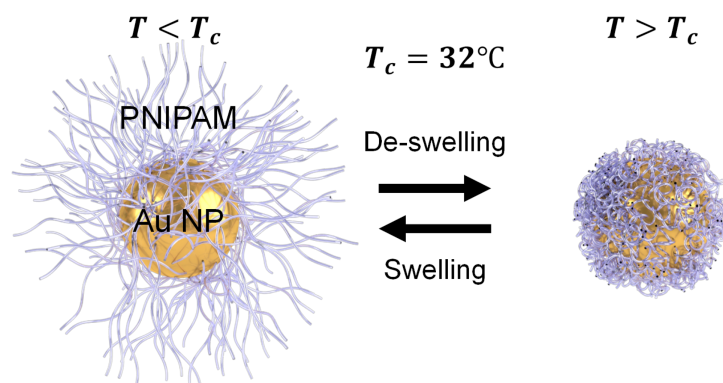


Fig. 2.1 Schematic of the temperature response of an ANT particle in an aqueous medium with a critical solution temperature, T_c , of 32°C .

The preparation of the Au@PNIPAM core-shell particles varies significantly between different studies, resulting in different shell thicknesses and densities. These differences have an impact on the swelling and de-swelling ratios of the shells. The shells can be ‘grafted-from’ or ‘grafted-to’ the gold nanoparticles, which are methods discussed in further detail in Section 3.1.2. In this work, the ANTs are prepared by synthesising or procuring the particles and polymers separately, then coating the particles via the ‘grafting-to’ method. The PNIPAM is grafted at a solution temperature above T_c , such that the polymer is in the globule state, to reduce surface density of the bound PNIPAM. The full synthesis and preparation details are described in Section 3.1.

In order to attach PNIPAM strands to the gold nanoparticles, the PNIPAM is terminated with binding functional groups. Amine-terminated PNIPAM is most commonly used in this work. It is well-known that amine functional groups adsorb to citrate-stabilised gold surfaces. However, it is still under debate whether the amine group is associated with the surface-bound negative ions by an ionic interaction or if it partially displaces the bound ions via a ligand-exchange interaction [61–63]. Regardless, the effective binding of the amine group to the surface of gold nanoparticles is sufficient to pin the PNIPAM to the gold nanoparticles. Alternative binding ligand groups, such as thiols, also bind the PNIPAM chains effectively. For the case of the thiol-gold interaction, it is understood that the thiol covalently binds to the gold surface [64, 65]. The effects of the different binding functionalisations are discussed in further detail in Section 4.3.1.

The PNIPAM shell affects the stability of ANTs in solution. The colloidal stabilisation mechanism changes from electrostatic to steric stabilisation. This is inferred from

the difference in zeta potentials of gold nanoparticles and ANTs. Synthesised 16 nm citrate-capped gold particles initially have a zeta potential of $\approx -30 \pm 7$ mV. Upon adding 20 μM of amine-terminated PNIPAM to form ANTs, the magnitude of the zeta potential reduces to -5 ± 3 mV. In general, colloid zeta potentials with absolute values below 20 mV are insufficient for charge stabilisation, and hence this suggests that the particles are sterically stabilised.

The molecular weight of the amine-terminated PNIPAM is 5.5 kDa, giving an average degree of polymerisation of ≈ 49 monomer units. From this, the contour length of the chains is ≈ 12 nm and the polymer length (l_p) in the extended coil state from the Flory diameter is estimated to be $l_p = 2\sqrt{aN^{3/5}} = 5.2$ nm [66]. Here, a is the length of a NIPAM monomer unit in the polymer backbone. An estimate can also be made for the Flory diameter of the polymer in poor solvent conditions, when $T > T_c$, where $l_p = 2\sqrt{aN^{1/3}} = 1.8$ nm. The change in Flory diameter of the polymer gives an initial approximation to the actuation length of the individual PNIPAM chains.

The addition of the PNIPAM shell also affects the refractive index surrounding the gold nanoparticles. The refractive index of PNIPAM at 25°C is $n = 1.34$ [67]. This is only slightly different than that of the aqueous medium, $n_m = 1.33$, and thus, only small differences are observed between the extinction spectra of ANT particles and uncoated gold nanoparticles, Au NPs (Figure 2.2a). A similar, weak redshift of the plasmon resonance is observed regardless of the initial particle diameter, as shown in Figure 2.2b. These small spectral changes are not discernible by eye.

Heating the ANT solution beyond T_c increases the refractive index of the PNIPAM to $n = 1.42$, but also decreases the shell thickness [67]. These combined effects only further redshift the plasmonic resonance of the ANTs by ≈ 10 nm. However, redshifts > 50 nm are observed experimentally when the suspension is heated. This large plasmon shift with temperature is caused by the flocculation of ANT particles and the subsequent plasmonic coupling between the gold nanoparticle cores [49].

2.2 ANT Flocculation

2.2.1 Heating-induced Flocculation

At temperatures above T_c , the hydrophobic and cohesive interactions between PNIPAM shells induce flocculation. The close proximity of the gold nanoparticle cores inside

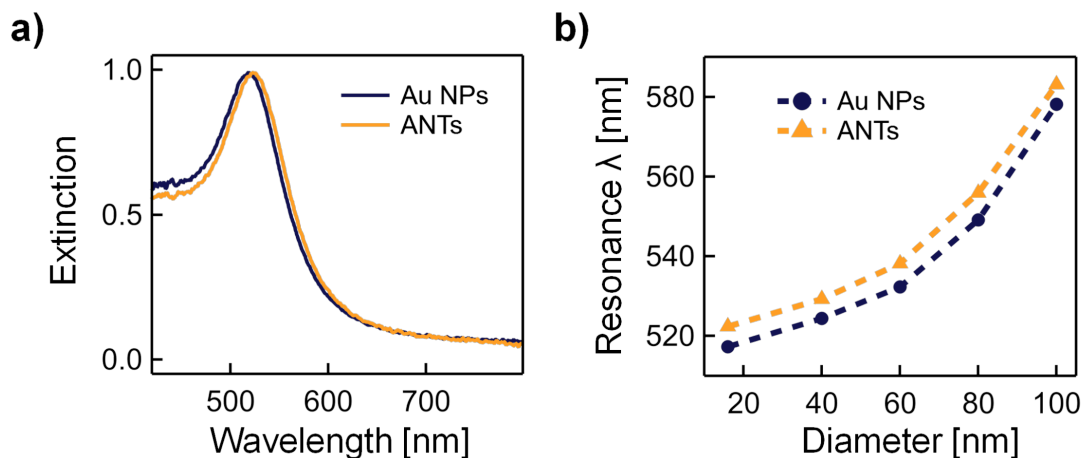


Fig. 2.2 Spectroscopy of gold nanoparticles (Au NPs) and ANTs in aqueous solution at 25°C. a) Normalised extinction spectra of 16 nm Au NPs and ANTs. b) Plasmonic resonance wavelengths, λ , of Au NPs and ANTs with diameters of 16, 40, 60, 80, and 100 nm.

the clusters results in large plasmonic resonance shifts and colour changes observable by eye (Figure 2.3a). Plasmon shifts, $\Delta\lambda$, are calculated from the difference between the peak extinction wavelengths for the individual ANTs, λ_{NP} , and the ANT clusters, λ_{cluster} . From Figure 2.3b, a redshift of $\Delta\lambda \approx 70$ nm is observed.

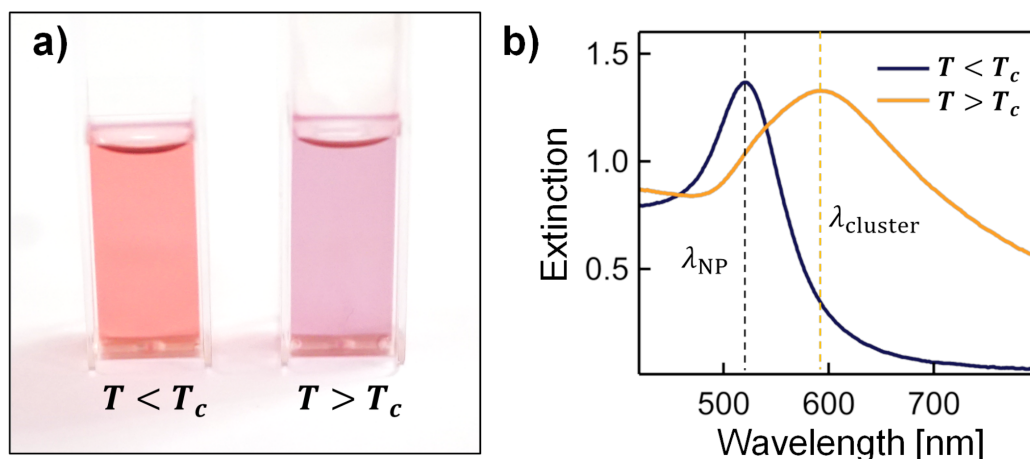


Fig. 2.3 Temperature-induced flocculation of ANTs. a) Photograph of cuvettes with 16 nm ANTs below (left) and above (right) the critical solution temperature, T_c , at 25°C and 40°C. The cuvettes are 1 cm wide. b) Corresponding extinction spectra at temperatures below and above T_c .

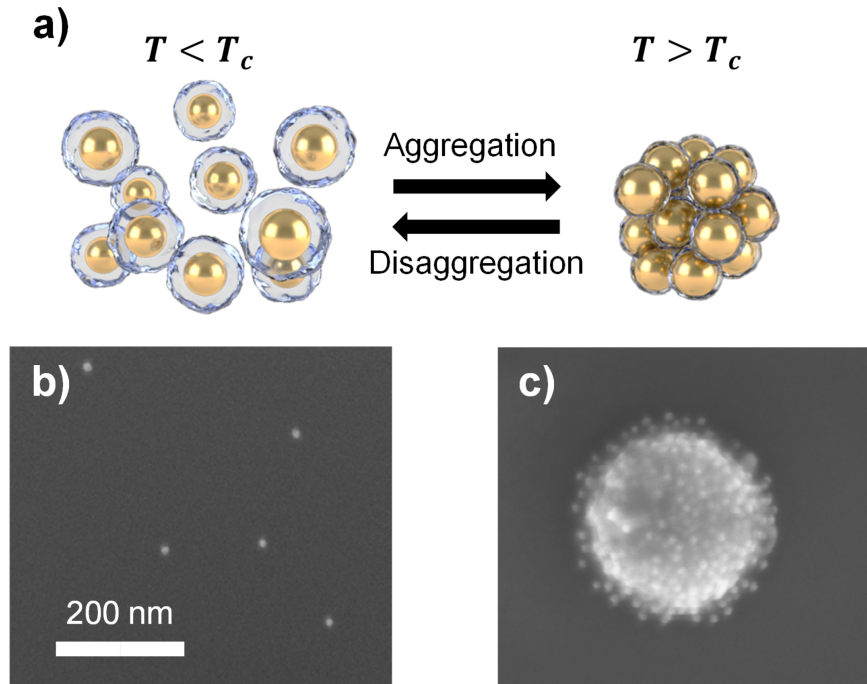


Fig. 2.4 ANT solution clusters. a) Schematic of the reversible flocculation of ANTs with temperature. b) SEM image of 16 nm ANT solution deposited on silicon at a temperature below the critical solution temperature, T_c , and c) SEM image of 16 nm ANT solution deposited on silicon at a temperature above T_c . Images b) and c) are at the same scale.

Evidence for the flocculation of the ANTs in solution is obtained by dynamic light scattering (DLS) and electron microscopy. A large increase in the hydrodynamic radius of the colloids is observed when the solution is heated from 25°C to 40°C. For 16 nm ANTs, the measured hydrodynamic diameter increases from ≈ 60 nm in the cold state to ≈ 440 nm in hot state. The aggregation is further confirmed by scanning electron microscopy (SEM) in Figure 2.4. These SEM samples are prepared by drop casting ANT solution on silicon substrates at temperatures below and above T_c .

The flocculation of ANTs is completely reversible with temperature. When the clusters are cooled below T_c , the ANT polymer shells rapidly swell and the clusters disaggregate. UV-Vis extinction time-series spectra elucidate part of the cluster formation mechanism (Figure 2.5). These spectra are captured while slowly heating the ANT solution in 1°C steps. While heating from 25°C to 40°C, the extinction spectrum remains constant until T_c . Above T_c , the ANT particles begin to aggregate. As the temperature and time increase, the extinction peak redshifts until it eventually stabilises. Here the stabilisation is observed at $\Delta\lambda \approx 100$ nm. While held at temperatures above

T_c , the magnitude of the extinction slowly decreases due to sedimentation of the aggregated ANTs. During cooling, no changes are observed until the temperature again reaches T_c , where the extinction spectrum rapidly reverts back to the initial state. As shown in Figure 2.5, the plasmon resonance consistently shifts with temperature over many cycles. This highlights the ability of ANTs to achieve reversible, strong optical responses to small temperature changes of $\approx 2^\circ\text{C}$.

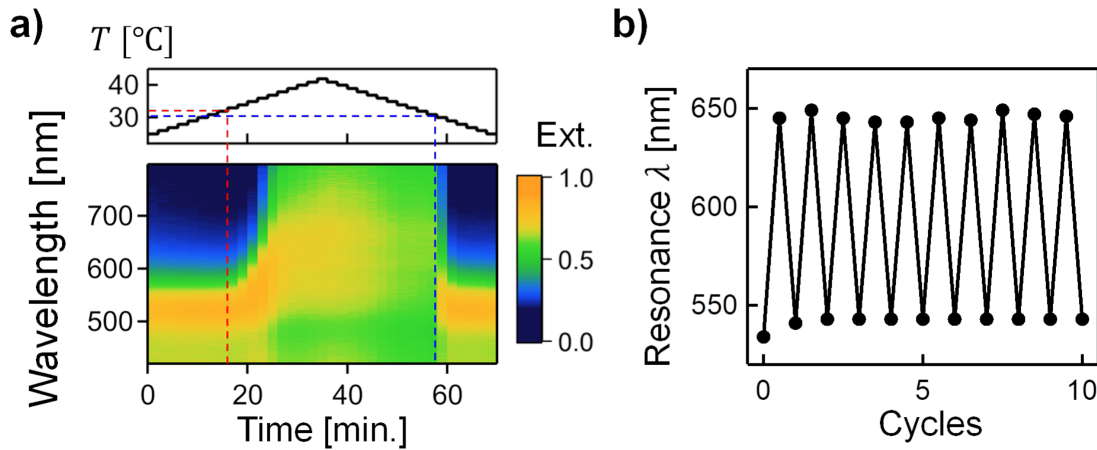


Fig. 2.5 Step heating and temperature cycling of an ANT suspension. a) Step heating of 16 nm with 1°C steps and a 2 min. equilibration time from 25°C to 42°C and then back to 25°C . The dashed lines mark the transition temperatures for heating (red) and cooling (blue). b) Peak extinction wavelength during 10 cycles of heating and cooling between 25°C and 40°C . The plot in b) is reproduced from Ding et al. [49].

The concentration of PNIPAM used to make ANTs affects the aggregation. As shown in Figure 2.6, there is an optimal concentration of PNIPAM to maximise plasmonic redshift at $\approx 20 \mu\text{M}$. At lower concentrations a peak remains at $\approx 520 \text{ nm}$, which indicates that either the individual ANT particles do not fully aggregate or smaller aggregates are formed. At concentrations $> 20 \mu\text{M}$ the peak shift diminishes. This is caused by a reduction in plasmonic coupling strength, which in turn is likely caused by an increase in spacing between the ANT particles inside the clusters. The interparticle spacing could increase due to the increased amount of excess unbound PNIPAM in the solution, which can fill the gaps between the particles. Regardless of the PNIPAM concentration in solution, the plasmon resonance in the cold state remains stable, which indicates that the colloids remain dispersed below T_c .

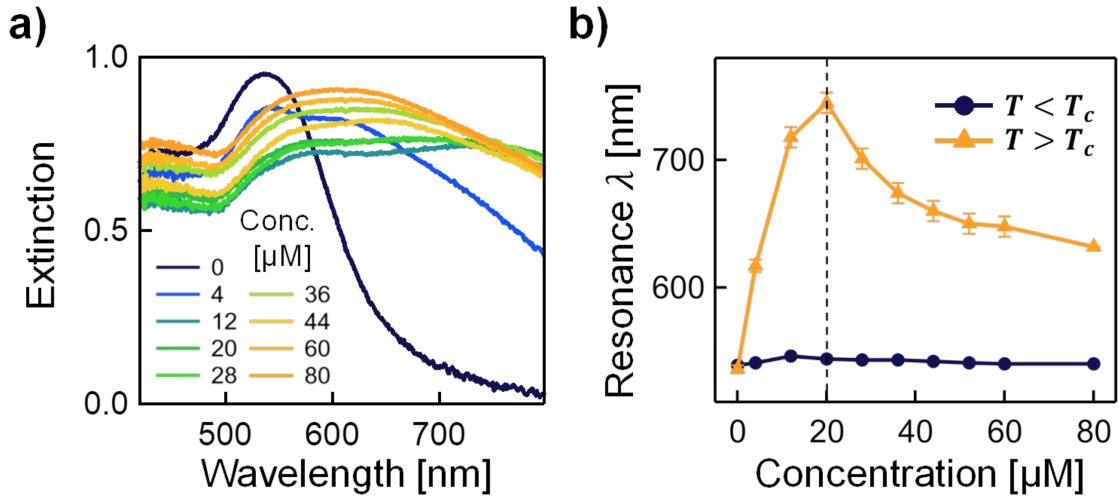


Fig. 2.6 Effect of PNIPAM concentration on the optical properties of the heated ANT solutions. a) Extinction spectra of 60 nm ANTs with different amine-terminated PNIPAM (5.5 kDa) concentrations. b) Peak extinction wavelength for heated ANT solutions with varying PNIPAM concentration. This figure is adapted from Ding et al. [49].

Other factors that influence the aggregation and optical response of the ANTs, include the termination of PNIPAM, the solution ionic strength, and the presence of excess PNIPAM. The effects of these parameters are studied in detail in Chapter 4.

2.2.2 Light-induced Flocculation

Plasmonic gold nanoparticles efficiently convert light to heat via absorption. This allows for the light-induced flocculation of ANTs in solution. As discussed in Section 1.2.3, the shells surrounding the gold nanoparticles with different thermal conductivity from the surrounding medium affect the particle temperature. Li et al. studied the change in thermal conductivity of aqueous solutions of PNIPAM in response to temperature and found that, for 25 g L⁻¹ PNIPAM solutions, it does not deviate further than $\approx 10\%$ from water [68]. Therefore, it is assumed that the most prominent effect of the PNIPAM shell on the plasmonic heating is the strong increase in absorption cross-section of the particle clusters in comparison to individual particles. The extinction spectra of 16 nm ANTs over time under 10 W irradiation at 532 nm is shown in Figure 2.7a. For this measurement the beam is blocked at 10 s intervals to acquire the spectra without saturation from laser scatter [49].

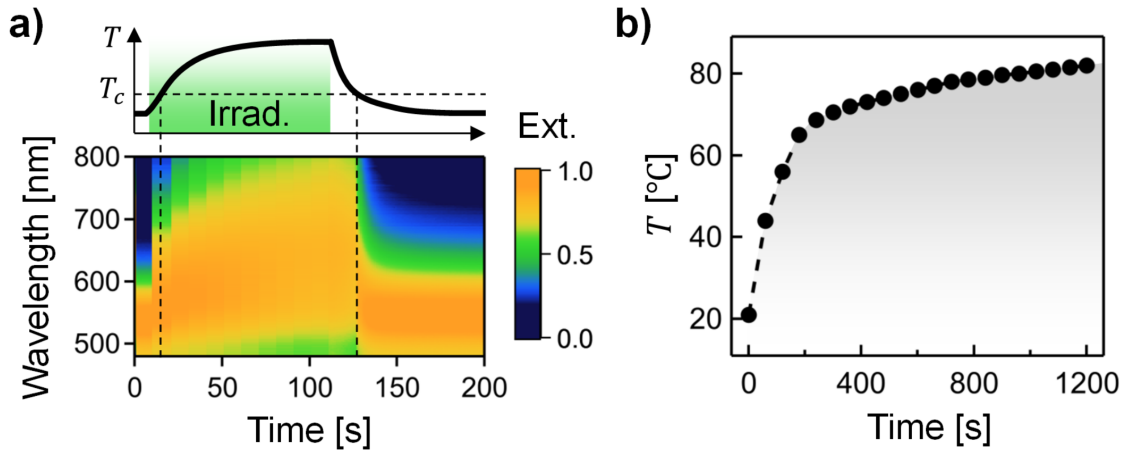


Fig. 2.7 Light-induced flocculation of 60 nm ANT particles. a) Extinction spectra evolution over time under 10 W irradiation at 532 nm. The beam is blocked at 10 s intervals to capture the spectra without saturating laser scatter. b) ANT solution temperature response during continuous irradiation. This figure is adapted from Ding et al. [49].

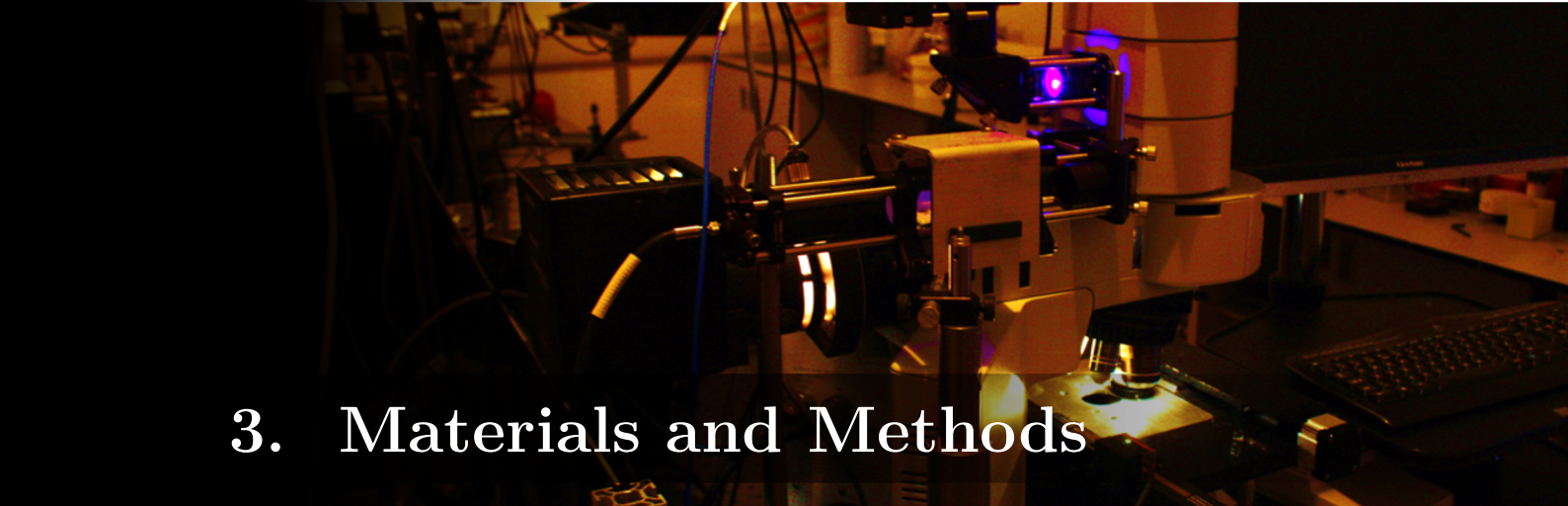
As observed in the direct heating case, when the solution temperature increases above T_c the extinction redshifts and broadens as ANT particles flocculate. The clusters rapidly disaggregate when the temperature drops below T_c . The measured increase in solution temperature as a result of the exposure to irradiation is plotted in Figure 2.7b. Over 2 minutes of constant irradiation, the temperature of the solution rises to $\approx 55^\circ\text{C}$.

In principle, the basic properties described here are not exclusive to Au@PNIPAM systems. Alternative plasmonic materials, such as silver, copper, and aluminium or even other highly absorbing materials, such as carbon nanoparticles, could be used depending on application constraints. Similarly, other thermoresponsive polymers could be used as the shell material. One could select polymers with different critical temperatures to satisfy the requirements of specific ANT system applications [69].

2.3 Summary

In this chapter, the dynamic assembly of PNIPAM-coated gold nanoparticles was introduced. These particles have been used for many applications that take advantage of their tunable optical and physical properties. The swelling and de-swelling of the PNIPAM shells and their ability to induce highly reversible colloidal flocculation in solution are presented. Furthermore, the self-assembly of ANTs is shown to strongly

change the plasmonic resonance of the colloids due to plasmonic coupling of gold nanoparticles inside clusters. These large physical and optical changes are triggered by bulk or light-induced heating above 32°C and reset by cooling back below the critical temperature. The assembly and disassembly of ANT clusters is revisited in Chapter 4 to propose a mechanistic model for the formation of the clusters after examining the effects of PNIPAM termination, concentration, and the ionic strength of ANT suspensions.



3. Materials and Methods

This chapter presents the methods used for fabricating and characterising ANT systems. The optical techniques and experimental setups designed to both control and characterise the behaviour of ANT systems are detailed. The following chapters regularly refer to the specific sections in this chapter to avoid repeating experimental details.

3.1 ANT Synthesis

The ANT nanoparticles consist of plasmonic cores surrounded by stimuli-responsive shells. Throughout this work, gold nanoparticles are used as the cores and the shells are poly(N-isopropylacrylamide) (PNIPAM). The materials and chemicals used for the preparation of ANTs are summarised in Table 3.1.

3.1.1 Gold Nanoparticle Cores

The plasmonic cores of ANT particles are monodisperse citrate-stabilised gold nanoparticles with selected diameters varying from 14 to 100 nm. As discussed in Section 1.2, the optical properties of plasmonic particles depend on their size. Advantageously, larger particles have greater absorption and scattering cross-sections as well as greater sensitivity to interparticle plasmonic coupling. The increase in the absorption cross-section reduces the irradiation power required for plasmonic heating. Also, the greater scattering cross-section and stronger plasmonic coupling enhance the optical signals of particles. This is very helpful for observing the behaviours of individual particles using optical microscopy, as presented in Chapter 5.

Although larger nanoparticles (> 40 nm) have advantageous optical properties, they are more challenging to produce. They suffer from greater polydispersity and generally require slow multi-step synthesis procedures to mitigate this, as compared to one-step synthesis procedures for small nanoparticles [70]. In addition, increasing size decreases particle sphericity, as crystal shapes with larger facet sizes become more dominant [71].

Table 3.1 List of materials and chemicals used for ANT preparation.

Component	Type	Size	Source
Nanoparticles	Au NPs	14 nm	Synthesised
	Au NPs	16 nm	Synthesised
	Au NPs	20 nm	BBI Solutions
	Au NPs	40 nm	BBI Solutions
	Au NPs	60 nm	BBI Solutions
	Au NPs	80 nm	BBI Solutions
	Au NPs	100 nm	BBI Solutions
PNIPAM	PNIPAM-NH ₂	5.5 kDa	Merck
	PNIPAM-SH	15 kDa	Synthesised ¹
	PNIPAM-COOH	6 kDa	Merck
	PNIPAM-H	10 kDa	Merck
Chemicals	Gold(III) Chloride Trihydrate		Merck
	Trisodium Citrate		Merck

Interpreting the optical signatures from ANT systems is more challenging with the loss of particle sphericity, as the complexity of the system greatly increases. Due to these disadvantages, the smaller 14 and 16 nm particles are predominantly used in this work. Beyond the differences in optical properties, the observed physical behaviours of ANTs do not change greatly with size, hence the choice of nanoparticle size is not crucial for many of the studied systems.

As indicated in Table 3.1, some gold nanoparticles are purchased while others are synthesised. The 20 to 100 nm particles ($CV < 8\%^2$) are procured from BBI Solutions. Smaller particles with diameters of 14 and 16 nm are synthesised in-house by modified Turkevich methods [72–74]. The 16 nm particles are prepared by refluxing an aqueous solution of 0.26 g L^{-1} gold(III) chloride trihydrate and abruptly adding trisodium citrate to reach a concentration 0.60 g L^{-1} . The reaction proceeds for 10 minutes, turning from a light-yellow solution, to black, and finally wine red, the characteristic colour of 16 nm gold particles. The size of the nanoparticles is confirmed

¹Synthesis conducted by Dr. Steven Barrow, Department of Chemistry, University of Cambridge

²Coefficient of Variation, $CV = \frac{\sigma}{\mu}$, where σ and μ are the standard deviation and mean of the particle diameters, respectively.

with a combination of UV-Vis extinction spectroscopy and electron microscopy (LEO GEMINI 1530VP FEG-SEM).

The 14 nm particles are synthesised by an adapted method with the purpose of increasing the particle density. This increases the extinction of the suspension and also simplifies post-synthesis processing to achieve dense slurries of ANT particles. The dense suspensions are used for the ANT systems described in Chapters 6 and 7. The particle density is increased during synthesis by proportionally increasing the concentrations of reagents. However, this only works up to a certain concentration before the quality of the nanoparticles diminishes. Li et al. proposed that the increased acidity of the trisodium citrate is the source of reduction in quality of nanoparticles when synthesised at higher concentrations [75]. They developed the simple strategy of compensating for the acidity of the trisodium citrate by adding sodium hydroxide. Adapting from their procedure, the 14 nm particles are synthesised by refluxing 1.0 g L⁻¹ gold(III) chloride trihydrate and 0.30 g L⁻¹ sodium hydroxide. Trisodium citrate is then rapidly added to reach a concentration of 1.3 g L⁻¹. The change in procedure increases the particle density from 3.1 × 10¹² mL⁻¹ for the 16 nm particles to 1.8 × 10¹³ mL⁻¹ for the 14 nm particles.

3.1.2 Grafting PNIPAM Shells

PNIPAM shells can be prepared by either ‘grafting-to’ or ‘grafting-from’ the surface of colloids. The method of ‘grafting-to’ involves adsorption of the polymer onto the colloid surface. On the other hand, the method of ‘grafting-from’ the colloids relies on surface initiated polymerisation from which the polymer is grown during synthesis [76]. Typically, polymer shells prepared by the ‘grafted-from’ method have greater surface density than shells prepared by ‘grafting-to’ the colloid [77]. Increasing the surface density tends to reduce the switching response of thermoresponsive polymers. For example, Malham and Bureau observed that high surface densities limit the thickness variation of PNIPAM layers in response to temperature cycling [78].

Consequently in this work, the ANT particles are coated with PNIPAM via the ‘grafting-to’ method in the globule state. Short-chain amine-terminated PNIPAM (PNIPAM-NH₂) is predominantly used; the effects of different terminations are explored in Chapter 4 including, thiol-terminated PNIPAM (PNIPAM-SH), carboxylic acid terminated PNIPAM (PNIPAM-COOH), and PNIPAM without a functional termination (PNIPAM-H). These polymers were purchased from Merck, formerly

Sigma-Aldrich, except the PNIPAM-SH, which was provided by Dr. Steve Barrow. When possible, PNIPAM with similar molecular weights (5 to 15 kDa) were selected to mitigate any effects from changing the length of the polymer.

The ANTs are prepared by coating the gold nanoparticle cores with non-crosslinked PNIPAM polymer shells. The standard preparation consists of adding 0.11 g L^{-1} of PNIPAM in two steps to the gold nanoparticle suspension as synthesised or purchased. Two aqueous stock solutions of the PNIPAM are prepared, one at a concentration of 0.1 g L^{-1} and the other at 1.0 g L^{-1} . First, the 0.1 g L^{-1} solution of PNIPAM is added to the particle suspension and heated to 40°C in a 1:8 (V:V) ratio. Subsequently, the 1.0 g L^{-1} stock is added to the heated solution in a 1:9 (V:V) ratio for a final PNIPAM concentration of 0.11 g L^{-1} ($20 \text{ }\mu\text{M}$ for 5.5 kDa). The two step addition sequence is adopted to reduce the irreversible aggregation of the nanoparticles during addition of the PNIPAM. It is observed that the gold nanoparticles remain more stable, with less aggregation during preparation, when adding the polymer ligands in two steps rather than all at once. Upon adding the second solution of PNIPAM, the ANTs form and immediately begin flocculating, which is marked by a change in solution colour from red to violet. The ANTs are prepared in the hot state such that the colloids are initially coated with collapsed PNIPAM. This leads to a lower surface density coating that exhibits better actuating properties. After one minute, the ANT solution is passively cooled and the red colour returns when the temperature drops below the critical temperature, T_c .

Once the standard ANT solutions are prepared, they can be further processed depending on their application. For some applications, the excess PNIPAM and ions in solution are removed by sequential sedimentation of the particles via centrifugation and redispersion in de-ionised (DI) water. Other applications require very dense particle solutions beyond what can be synthesised with current techniques. To achieve extremely dense particle solutions, the ANTs are sedimented by centrifugation. After decanting the supernatant, the dense solution is re-spun above an equal volume of chloroform to sediment the ANTs in the chloroform phase. The centrifugation of 14 and 16 nm gold nanoparticles is conducted with a minicentrifuge (Minispin Plus, Eppendorf) at 14.5 krpm for 15 minutes. After removing the aqueous and chloroform supernatants, the ANT slurry is dried in an oven at 70°C . The dried particles are then stored and redispersed in DI water prior to use.

3.2 Substrates for ANT Systems

The ANT systems discussed in later chapters make use of various important substrates. These include ultra-flat gold surfaces for the nanoparticle on mirror plasmonic structure presented in Chapter 5 and nanoporous membranes for the controllable exchange of fluids to dynamic thin-films which is studied in Chapter 6.

3.2.1 Template-stripped Gold

Template-stripping is a method for generating wafer-scale ultra-flat gold surfaces developed by Hegner et al. [79]. The gold substrates are prepared in a clean room facility with an electron beam (e-beam) evaporator (Kurt J. Lesker Company PVD 200)¹. The substrate preparation begins with a cleaned 4" silicon wafer (<100>) as illustrated in Figure 3.1. The wafer is cleaned by sequential rinses of Decon90, DI water, ethanol, isopropanol, and DI water. Then it is dried with a nitrogen gun. A 100 nm thick gold film is deposited at a rate of 1 \AA s^{-1} on the wafer without an adhesion layer. Drops of Epo-Tek 377 epoxy glue ($\approx 3 \text{ \mu L}$) are cast on the film and diced pieces ($\approx 1 \times 1 \text{ cm}$) of silicon wafer are placed on the drops. The glue is cured at 150°C for 2 h and slowly cooled to room temperature at 10°C h^{-1} to avoid cracking from temperature gradient-induced film stresses. Prior to use, individual silicon dice are pried from the gold coated wafer. The low adhesion between the gold and silicon wafer allows for the gold to be easily stripped off with the glued silicon wafer dice. The released gold surface is near atomically-flat and dust free. This is ideal, since the low surface roughness minimises sharp features on the gold surface which can greatly affect plasmonic field enhancement profiles. These flat gold surfaces play a crucial role in Chapter 5, where individual ANT particles plasmonically couple to their image charges in the gold substrate.

3.2.2 Semi-permeable Membranes

Semi-permeable membranes made of thin nanoporous materials are used to allow water to flow through while inhibiting the flow of ANT particles. These membranes enable the exchange of water to and from ANT particles for reversible hydration and dehydration.

¹The evaporation of gold was conducted by Dr. Bart de Nijs, Department of Physics, University of Cambridge

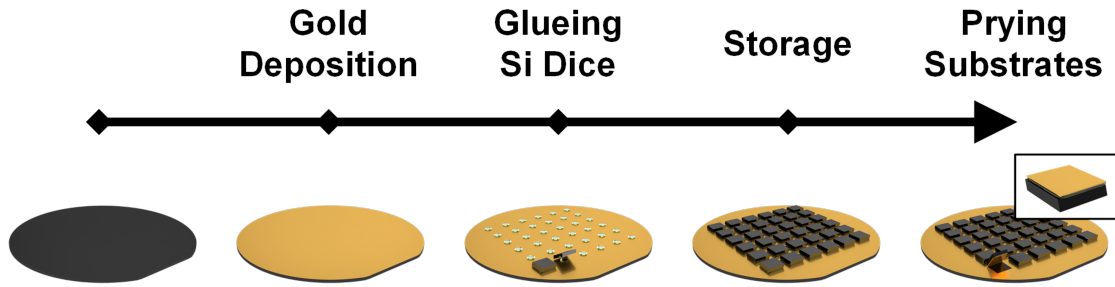


Fig. 3.1 Schematic of the template-stripped gold preparation procedure.

This type of system is explored in Chapter 7, where porous aluminium oxide (Al_3O_2) is used as the model membrane. The Al_3O_2 membranes with a 25 mm diameter and 20 nm pore size (50% porous) are procured from ThermoFisher (Whatman Anodisc). The membrane thickness is $\approx 60 \mu\text{m}$ and the pore density is 10^{11} cm^{-2} . The pores are small enough to prevent the 14 nm ANT particles ($\approx 60 \text{ nm}$ in size with the PNIPAM shell) from diffusing through, while retaining the ability for water to wick across.

3.3 Optical Setups and Techniques

3.3.1 Extinction Spectroscopy

Extinction spectroscopy is used to study the size and concentration of gold nanoparticles and probe the aggregation behaviour of ANTs suspensions [80]. The extinction spectra are highly sensitive to the size and spacing between the nanoparticles when forming clusters. Hence, it is a useful technique for analysing the temperature response of ANT suspensions.

Collimated white light from a fibre-coupled (50 μm diameter) Xenon lamp (HPX-2000-HP-DUV) is passed through a sample cuvette with a fixed length of 1 cm. The transmitted light is focused into a 50 μm diameter fibre connected to a spectrometer (Ocean Optics QE Pro), as illustrated in Figure 3.2. The illumination area through the sample is $\approx 2 \text{ mm}$ in diameter. The cuvette holder has 2 pairs of orthogonal optical ports which allows for the simultaneous free-space coupling of a 532 nm laser. The laser can optically heat the ANT solutions during extinction measurements and a heated metal cuvette holder is used to bias the temperature of the suspensions.

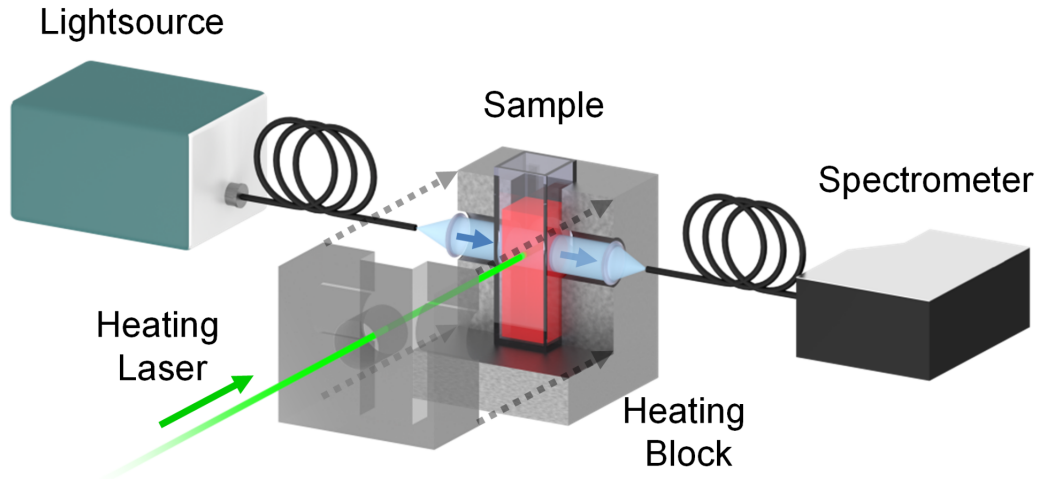


Fig. 3.2 Schematic of the extinction spectroscopy setup. The sample temperature is controlled optically with a free-space coupled laser and electrically by adjusting the temperature of the cuvette holder with a heating plate.

The transmitted light intensity, I , through the sample is referenced to the transmitted light intensity through a cuvette with DI water, I_0 . The ANTs partially scatter and absorb the incident light depending on the wavelength, which results in an attenuation of the transmitted light. The attenuation follows Beer-Lambert's law and directly relates to the sample transmittance, T , by

$$T = \frac{I}{I_0} = \exp(-\sigma_{\text{ext}} N \ell), \quad (3.1)$$

where σ_{ext} is the extinction cross-section ($\sigma_{\text{ext}} = \sigma_{\text{abs}} + \sigma_{\text{scat}}$), N is the particle number density, and ℓ is the sample path length ($\ell = 1$ cm). In relation, the extinction, ε_{ext} , is conventionally defined as

$$\varepsilon_{\text{ext}} = -\log_{10}(T) = -\log_{10}\left(\frac{I}{I_0}\right). \quad (3.2)$$

Given that the aggregation of ANT particles greatly changes the extinction properties of solutions, these measurements give insight into the structure of ANT clusters. The extinction is closely tied to σ_{ext} from equation 1.10. This means it is directly dependent on the ANT colloid polarisability, which also implies that ε_{ext} relates to both the size of clusters and proximity of the gold nanoparticles within. These relations are explored in greater detail in Chapter 4.

3.3.2 Dynamic Light Scattering

Dynamic light scattering (DLS) is an optical technique for determining the hydrodynamic size of colloids suspended in solution. The hydrodynamic radius refers to the radius of an effective slipping plane surrounding an arbitrarily shaped colloid. The slipping plane defines an interface near the surface of a colloid, which divides solvent molecules that behave as if they are bound to the colloid and solvent molecules that behave freely as if they are far away in the bulk solution. For ANT solutions, the hydrodynamic size is determined by the combination of gold nanoparticle core size, the thickness of the PNIPAM shell, and the additional thickness of a bound water or diffuse ion shell. It is assumed that the excess bound water layer (≈ 2 nm from the Debye screening length) is negligible compared to the PNIPAM thickness shell, such that the slipping plane of the ANT particles approximately contours the PNIPAM shell surface.

Briefly, DLS involves irradiating dilute solutions of colloids with coherent light. The intensity of light scattered by the colloid dispersion projects a fluctuating speckle pattern that is recorded. These fluctuations are caused by the Brownian motion of the suspended colloids. The decay rate of the time dependent intensity-autocorrelation function of these fluctuations relates directly to the translational diffusion coefficient of the colloids. The second order autocorrelation, g^2 , is determined from the recorded intensity over time, $I(q, t)$, [81]

$$g^2(q, \tau) = \frac{\langle I(q, t)I(q, t + \tau) \rangle}{\langle I(q, t) \rangle^2} = 1 + \exp(-q^2 D_t \tau), \quad (3.3)$$

where $q = \frac{4\pi n}{\lambda} \sin\left(\frac{\theta}{2}\right)$ and τ is the delay time. The scattering vector q is related to the incident laser wavelength, λ ; the sample refractive index, n ; and the angle of detection, θ , with respect to the angle of the incident laser. The hydrodynamic radius, R_h , of a sphere can be calculated from translational diffusion coefficient, D_t , using the Stokes-Einstein equation, [82, 83]

$$D_t = \frac{k_B T}{6\pi\eta R_h}, \quad (3.4)$$

where, k_B is the Boltzmann constant, T is the sample temperature, and η is the viscosity of the medium.

The DLS measurements of ANT colloids were conducted with a Zetasizer Nano (Malvern). They are used to estimate the changes in the size of the dispersed ANT particles and aggregates with temperature. Although, these measurements are very convenient for studying the dynamic behaviours of ANT suspensions, they suffer from systematic errors. The sedimentation of the colloids partially segregates the aggregates by size vertically along the sample cuvette. In addition, The absorption of light by the ANT particles generates local thermal gradients as discussed in Section 1.2.3. These gradients can drive convective flows, which cause additional motion of the colloids on top of their typical Brownian motion. The drawbacks of DLS measurements prevent the precise measurement of the size ANT particles and aggregates. However, the relative changes in size estimated by DLS, in conjunction with electron microscopy, do provide useful insights on the interactions of ANT particles.

The Zetasizer Nano instrument is also used for measuring the zeta potentials of ANT colloids. Unfortunately, it does not resolve the location of charges on ANT colloids, which can be at the surface of the gold nanoparticle cores or trapped within the polymer shell. However, relative changes in the zeta potential are indicative of differences between ANT colloid solutions as discussed in Chapter 4.

3.3.3 Microscopy Techniques

The primary technique used to characterise the behaviours of ANT systems is optical microscopy. The microscope used consists of a modified Olympus BX51 coupled with a spectrometer (Ocean Optics QE65000), laser (Coherence CUBE), camera (Teledyne Lumenera Infinity 2 or Photron FASTCAM for high speed imaging) and a removable heating stage (Linkam). The microscope can be reconfigured for bright-field (BF) and dark-field (DF) reflection imaging and spectroscopy, as well as BF transmission imaging and spectroscopy. These configurations have different illumination paths, but share collection paths.

The DF reflection configuration is used to image scattering objects. In this configuration, only scattered light from the sample is collected while light that is specularly reflected is omitted, as illustrated in Figure 3.3a. Among several lenses, the illumination path consists of a halogen lightsource (Philip 7023), an aperture diaphragm (AD), a field diaphragm (FD), an elliptical mirror, and an objective lens. The light from the source is guided by a series of lenses through the aperture and field diaphragms in an illumination arm above the sample. The light is reflected off an elliptical ring mirror

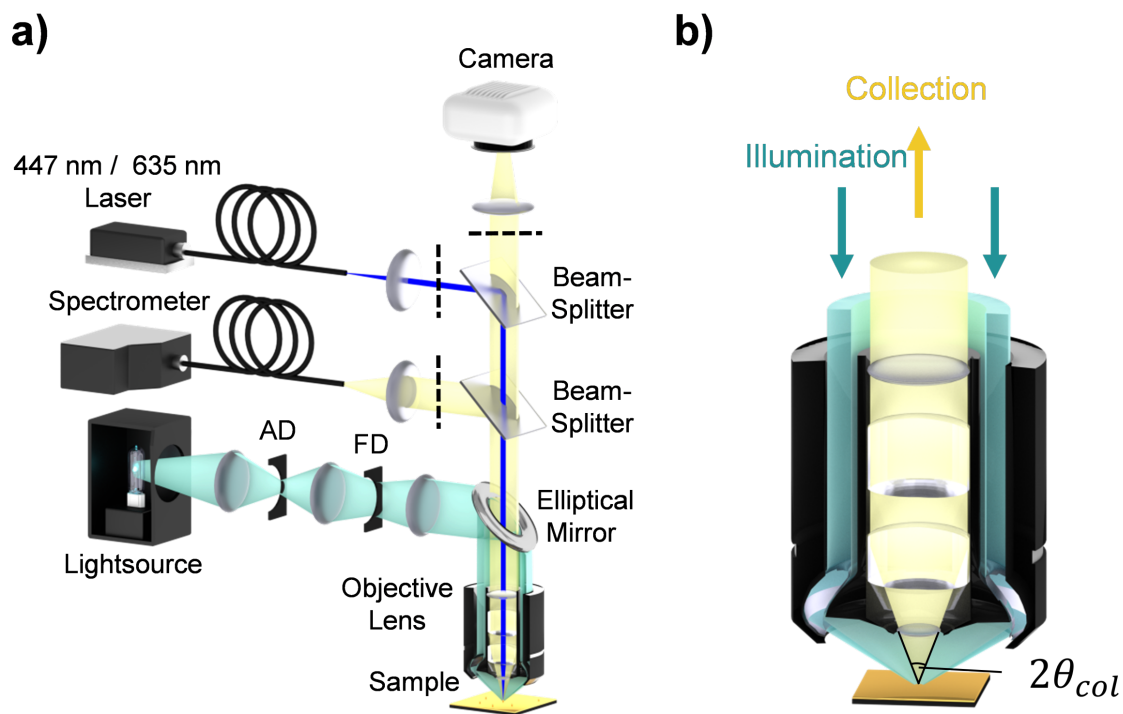


Fig. 3.3 Schematic of the microscope setup in the dark-field illumination configuration. a) Microscope setup with the illumination path in teal and the collection path in yellow. The laser irradiation path is shown in blue. Black dotted lines mark slots for optical filters. The abbreviations AD and FD refer to the aperture and field diaphragms. b) Illustration of the DF objective lens cross-section with the illumination path in teal and the collection path in yellow. Only light that is scattered from the sample within the cone defined by the angle θ_{col} is collected.

and the lightsource is imaged at the back focal plane of the objective to satisfy the Köhler illumination criterion. This defocuses the light source on the sample plane to uniformly illuminate the sample without introducing features from the lightsource filament. The iris for the aperture diaphragm limits the brightness by reducing the solid angle of light projected from the lightsource. It lies on a focal plane conjugate to the back focal plane of the objective. Whereas the field diaphragm controls the illumination area size on the sample. It lies on a focal plane conjugate to the sample surface, such that the iris and sample surface are in focus simultaneously. This implies the iris can be imaged on the camera to focus the sample surface, which is very helpful for imaging samples with weak contrast.

The microscope uses specialised DF objectives, as shown in Figure 3.3b, with distinct illumination and collection paths for DF microscopy. The microscope objectives and

their optical specifications are listed in Table 3.2. The elliptical ring mirror couples a ring of light into the illumination path of the objective. This illuminates the samples at an angle θ_{inc} which is larger than the collection angle θ_{col} . In this configuration, high-angle specular light reflected from the sample is not collected, whereas light that is scattered within the cone defined by the solid angle $2\theta_{col}$ is collected. The collection angle relates to the numerical aperture, NA , by

$$NA = n \sin(\theta_{col}), \quad (3.5)$$

where n is the refractive index between the objective and the samples, which in this case is $n = 1$ for air.

Table 3.2 List of microscope objectives and their optical specifications.

Magnification	NA	WD	Source
5x	0.15	20 mm	Olympus BD MPlanFL N
20x	0.45	3.1 mm	Olympus BD MPlanFL N
50x	0.8	1.0 mm	Olympus BD MPlanFL N
100x	0.8	3.3 mm	Olympus BD LMPlanFL N

The BF configuration is very similar to that of DF except the centre light path of the objective is used simultaneously for the illumination and collection paths. The elliptical ring mirror is replaced with a 50:50 beamsplitter and a ring-shaped beam stop to block the DF illumination path. In this configuration both specular and diffuse reflected light are collected within the solid angle $2\theta_{col}$.

The setup can also be configured for BF transmission microscopy to characterise transparent or semi-transparent samples. In this case a different illumination arm is used. It contains similar a lightsource, lenses, and diaphragms and is positioned below the sample plane. The sample is illuminated from below using the a similar component arrangement as the reflective illumination arm, but the illumination and collection paths are decoupled. A condenser lens focuses the light on the sample and sharpens the transmission images by increasing the light incident angles.

The collection paths for the different imaging and spectroscopy configurations are shared. The light collected by the objective is collimated towards the lens that focuses

the sample image onto the camera. A removable 50:50 beamsplitter is inserted to simultaneously conduct imaging and spectroscopy. The beamsplitter sends 50% of the collected light towards a lens ($f = 15$ cm) that focuses the light into a $50\ \mu\text{m}$ multimode fibre connected to the spectrometer. The fibre lies on a conjugate plane to the sample surface and only collects light from a small area on the sample. The size of the area depends on which objective is used. For instance, with the 100x objective the fibre collects light from the sample surface in an $\approx 2\ \mu\text{m}$ diameter spot.

Another removable beamsplitter is inserted into the collection path to deliver laser irradiation onto the sample. This irradiation is used to drive the actuation of ANT systems. It is coupled to a single-mode optical fibre with its end positioned on another conjugate sample surface plane. The beam is collimated and projected onto the objective back aperture with a 90:10 beamsplitter, and then focused into a tight spot on the sample surface. Two lasers with emission wavelengths of 447 nm ($P_{\text{max}} = 40$ mW) and 635 nm ($P_{\text{max}} = 25$ mW) are interchangeably coupled. The laser is connected to a function generator (Hewlett Packard 33120A) for modulation at frequencies up to 15 MHz. Optical filters are placed in front of the camera, spectrometer, and laser during irradiation experiments, as marked by the black dashed lines in Figure 3.3a. Various optical filters are used to reduce the laser spectral linewidths and to remove the saturating laser reflection and scattering from images and spectra during measurements. The filters are specified in the following chapters where they are relevant.

3.4 Summary

The experimental methods for preparing ANTs and characterising their behaviours in various systems were described in this chapter. ANT solutions are prepared from gold nanoparticles with different sizes and PNIPAM with different termination groups. The solutions can be further processed to reduce the excess PNIPAM and ions in solution, or to increase particle density, depending on their application. In addition, important substrates for various ANT systems were discussed, including template-stripped gold and semi-permeable membranes. Lastly, the methods used to characterise the behaviours of ANT systems, including extinction spectroscopy, DLS, and microscopy techniques, were presented. The next chapters rely greatly on these methods to provide evidence for their respective conclusions.

The top of the page features three circular micrographs showing the reversible assembly of ANTs. The leftmost micrograph shows a dark red liquid containing several bright yellow-gold spherical particles. The middle micrograph shows a clear, colorless liquid with a few yellow-gold particles. The rightmost micrograph shows a purple liquid with a cluster of yellow-gold particles. The background is a dark, textured surface.

4. Formation of ANT Clusters

This aim of this chapter is to investigate the underlying mechanisms driving the reversible assembly and disassembly of ANT colloids. Chapter 2 introduced the reversible flocculation behaviour of ANTs and it was demonstrated that the optical properties of ANT clusters depend on the concentration of PNIPAM in solution. Here, other parameters that affect the flocculation of ANTs are studied. The effects of the PNIPAM terminal group on the cluster formation are discussed, followed by the effects of salt concentration, and the role of excess PNIPAM in solution. In addition, the optical response of nanoparticle clusters is modelled to predict the internal structure of the ANT clusters and explain the observed behaviours of ANTs in different solution conditions. It is shown that these factors are responsible for the multi-stable nano-configurations observed in ANT particle assembly.

4.1 Cluster Formation Mechanism

It is observed that clusters form when ANT suspensions are heated above the critical temperature T_c . These clusters have very different hydrodynamic sizes and plasmon shifts depending on their solution conditions. This suggests that the structures formed by the reversible assembly of ANT colloids can be controlled. This could be of great interest for regulating the self-assembly of complex nanostructures [84].

Initially, the effects of different PNIPAM terminations and solution ionic strengths are studied. The size, zeta potential, and plasmon shift of the ANTs in the cold state ($T = 25^\circ\text{C}$) and hot state ($T = 40^\circ\text{C}$) are measured, both with and without an added 50 mM NaCl, as summarised in Table 4.1. The plasmon shifts are measured from the difference between the resonance peak wavelengths in the hot state and cold state extinction spectra. These solutions are prepared using 16 nm particles with low-molecular weight PNIPAM as described in Section 3.1. The polymer chains coat the surface of the gold, forming ANTs which reversibly aggregate with cycling temperature. The sizes of the ANT particles and colloids are approximated by their

hydrodynamic radii, which are measured by Dynamic Light Scattering (DLS). This technique is discussed in further detail in Section 3.3.2.

Table 4.1 Effects of PNIPAM termination and salt on ANT cluster formation.¹

Sample NaCl [mM]	PNIPAM-H 0 / 50	PNIPAM-NH ₂ 0 / 50	PNIPAM-SH 0 / 50	PNIPAM-COOH 0 / 50
Diameter (25°C) [nm]	50 / 94	60 / 75	60 / 120	40 / 60
Diameter (40°C) [nm]	50 / 520	440 / 460	150 / 680	76 / 450
Plasmon Shift [nm]	2 / 40	30 / 105	4 / 42	3 / 75
Au NP Gap (est.) @40°C [nm]	41 / 8.4	10 / 2.5	44 / 9.4	38 / 3.8

Interestingly, without the addition of NaCl, only ANTs prepared with PNIPAM-NH₂ show a significant spectral redshift and a large increase in hydrodynamic radius when heated. This suggests that the amine termination group plays an important role in the aggregation of the particles. It is also observed that the addition of NaCl increases the size of the clusters in the hot state and the plasmon shift for all PNIPAM terminations. In addition, the plasmon shift is not simply dependent on the size of the clusters, as the largest clusters do not exhibit the largest plasmon shifts. For instance, the 680 nm diameter clusters that are formed with PNIPAM-SH, when 50 mM of NaCl is added, have plasmon shifts of 42 nm. Whereas, smaller 460 nm clusters formed with PNIPAM-NH₂ show much larger plasmon shifts of ≈ 105 nm. Furthermore, for the PNIPAM-SH without NaCl, 150 nm clusters are formed, yet the observed plasmon shift is negligible at ≈ 4 nm. These observations can be attributed to differences in the proximity and number gold nanoparticles within the clusters.

The unintuitive results obtained here are explained with a cluster formation model where the ANTs can form distinct cluster configurations depending on the electric potential (ϕ) of the gold nanoparticles within the clusters. Initially, the particles are assumed to be uniformly distributed within the clusters, but retain mobility such that they can migrate to reduce their interparticle distance, as illustrated in Figure 4.1.

¹The DLS data for this table was acquired by Dr. Tao Ding, Department of Physics, University of Cambridge

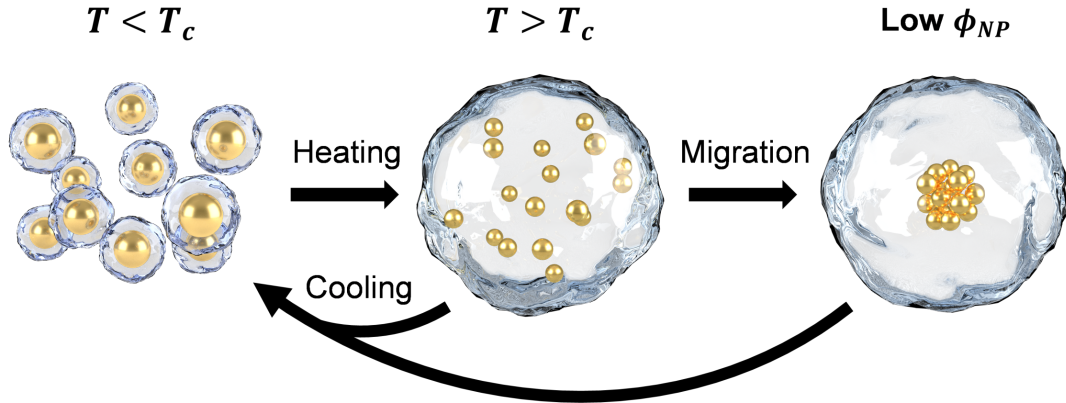


Fig. 4.1 Schematic of the ANT cluster formation. When heated above T_c , the ANTs aggregate with excess PNIPAM forming clusters with a roughly uniform distribution of ANT particles. These particles can subsequently migrate closer together within the cluster to set distance depending on the electric potential between the particles (ϕ_{NP}). This assembly is reversibly controlled by cycling the temperature of the solution below and above $T_c = 32^\circ\text{C}$.

The initial mean separation of the ANTs in the cold state (d_{NP}) can be approximated by the Wigner-Seitz radius, where $d_{NP} \approx (3/(4\pi N_{NP}))^{\frac{1}{3}} = 460 \text{ nm}$ and N_{NP} is the particle number density. Similarly, the mean separation of the polymer strands in solution can be estimated, giving $\approx 30 \text{ nm}$ for 0.11 g L^{-1} PNIPAM-NH₂. Because the hydrodynamic radius of the polymers is also much smaller than that of the gold nanoparticles (for 5.5 kDa PNIPAM this is $\approx 1.4 \text{ nm}$), the PNIPAM chains are able to diffuse much faster [85]. Hence, it is expected that PNIPAM clusters form before encountering ANTs in solution. This process spaces the ANTs within the clusters. Therefore, in this mechanistic model, the PNIPAM tethers the ANTs together, but they remain mobile within the cluster to reach a final proximity set by the electric potential repulsion between them. This proposed model can explain the discrepancies between the optical properties and sizes of the clusters.

4.2 Modelling ANT Clusters

Before further analysing the experimental results, a mathematical model is developed to describe the effects of cluster size and gold particle separation on the plasmon resonance. The model predicts plasmon shifts for clusters with respect to the gap size between the particles at given cluster sizes. The model is based on transition matrix (T-matrix) simulations of gold colloids inside a spherical PNIPAM matrix.

Extrapolation is required for the largest aggregate sizes due to the heavy computational resources required for these simulations.

4.2.1 Multisphere T-matrix Simulations

Mackowski's Multiple Sphere T-matrix (MSTM, v3.0) code (available open source) is used to compute the extinction cross-sections of the ANT clusters [13]. The T-matrix simulations are performed for varying interparticle distances and aggregate sizes. The arrangements of particles in the clusters are generated quasi-randomly using a step-wise addition growth method (Figure 4.2). Beginning from a randomly orientated dimer, individual 16 nm spherical gold particles are randomly adhered to the surface of the growing cluster with a fixed interparticle distance, d . The incident particles are allowed to relax to the nearest surface dimer while maintaining a constant interparticle distance. The clusters are grown using this method until a specified total diameter, D , is reached. The relaxation step mitigates the rapid formation of fractal chains, which are not observed experimentally.

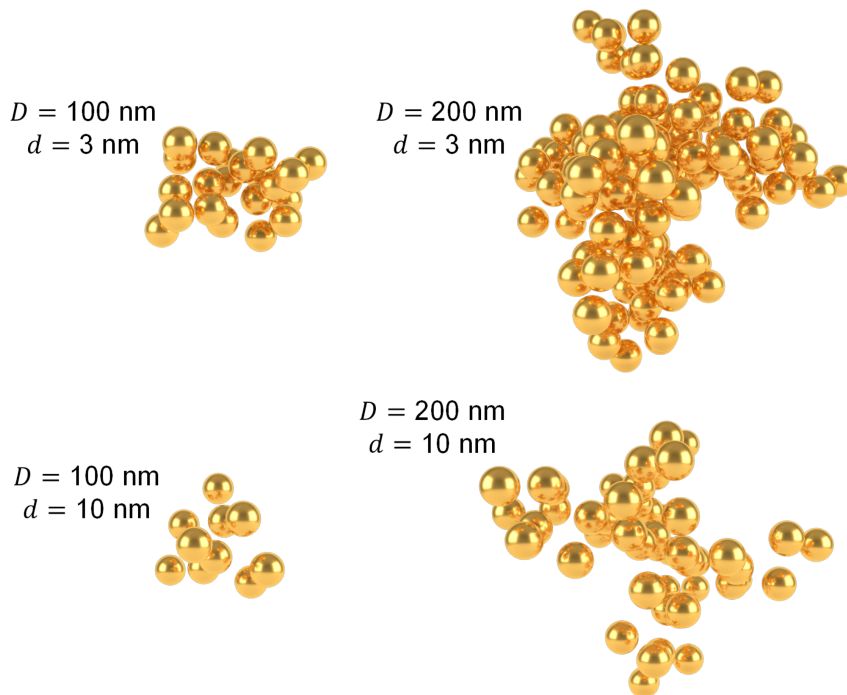


Fig. 4.2 Instances of randomly generated 16 nm gold particle clusters with set nearest-neighbour interparticle separations, d , and cluster diameters, D . Each particle has a coordination number greater than or equal to 2 within the clusters.

The T-matrix simulations are performed on the clusters after they are enveloped in a spherical PNIPAM medium ($n = 1.42$ [67]) with an external aqueous medium ($n = 1.33$) (Figure 4.3). The dielectric function of the gold is interpolated from Johnson and Christy [8].

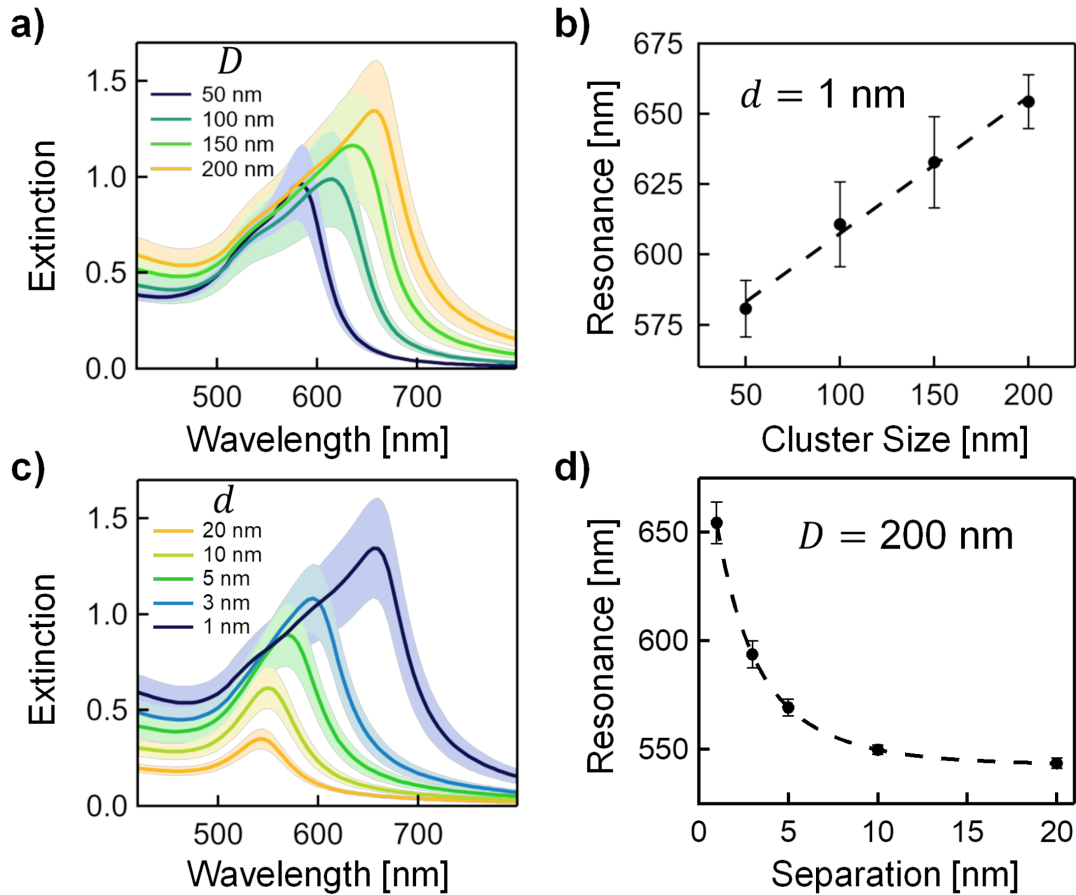


Fig. 4.3 Simulated extinction spectra of ANT clusters with 16 nm particles from T-matrix calculations with cluster diameter, D , and particle separation, d . a) Extinction spectra, and b) plasmon resonance response to changing cluster diameter for 1 nm gaps between the nearest particles. c) Extinction spectra, and d) plasmon resonance for different particle separations inside an aggregate with a 200 nm diameter. The shaded areas correspond to the standard deviation from many (≥ 50) quasi-randomly generated aggregates and the solid line is the mean extinction.

Fixing the interparticle spacing to 1 nm and increasing the size of the ANT cluster results in a redshift of the extinction peak (Figure 4.3a). This approximately linear response (Figure 4.3b) is similar to redshifts observed for one-dimensional plasmonic particle chains with increasing length [86]. It is also shown that decreasing the

interparticle distance in the cluster induces a significant redshift (Figure 4.3c and 4.3d). The plasmon shifts for larger (> 200 nm) clusters, as measured by DLS in Table 4.1, must be extrapolated due to the excessive computational resources required to calculate the extinction cross-sections (> 600 particles are used here already).

4.2.2 Extrapolated Cluster Model

The aim of the extrapolated model is to generate an analytical expression for the plasmon shift that takes into account the effects of interparticle separation and the overall cluster size. The strategy begins with an analytical expression for estimating the plasmon shifts, $\Delta\lambda_d$, from dimers based on the gap size, d . The expression is then modified with a model for one-dimensional particle chains with increasing length to approximate the effect of growing larger clusters with diameter, D .

Benz et al. derived the analytical expression for the plasmon resonance wavelength of dimers, λ_d , which is [87]

$$\lambda_d = \lambda_p \sqrt{2\varepsilon_m + \varepsilon_\infty + 4\varepsilon_m \eta}, \quad (4.1)$$

where λ_p is the plasma frequency, ε_m is the permittivity of the medium, ε_∞ is the high frequency limit of the permittivity, and $\eta \equiv C_g/C_s = n_g^{2.5} \times \ln \left[1 + \frac{aR}{d} \right]$ is the ratio of the gap capacitance and the capacitance due to the fringing field between the particles. The gap refractive index is n_g , R is the radius of the particles, and a is a fitted parameter related to the area of interaction between the dimer particles. This expression is derived from a capacitance model where the coupling between plasmonic particles is mediated by a gap capacitance, C_g , which redshifts the resonance frequency of the single particles and provides a good prediction for the plasmon shift of dimers. The plasmon shift is the difference between the dimer resonance, λ_d , and the single nanoparticle resonance, λ_{NP} , where $\lambda_{\text{NP}} \approx \lambda_p \sqrt{2\varepsilon_m + \varepsilon_\infty}$ from the Drude model. Therefore, substituting in Equation 4.1 gives

$$\Delta\lambda = \lambda_d - \lambda_{\text{NP}} = \lambda_p \sqrt{2\varepsilon_m + \varepsilon_\infty} \left(\sqrt{1 + \left(\frac{4\varepsilon_m}{2\varepsilon_m + \varepsilon_\infty} \right) n^{2.5} \times \ln \left[1 + \frac{aR}{d} \right]} - 1 \right). \quad (4.2)$$

This is the basis for expressing the plasmon shift as a function of the fitted parameters a , b , and c in the form

$$\Delta\lambda = b \left\{ \sqrt{1 + c \ln \left[1 + \frac{aR}{d} \right]} - 1 \right\}, \quad (4.3)$$

where c is constrained to $c = n_g^{2.5} \times 4\epsilon_m / (2\epsilon_m + \epsilon_\infty) = 0.43$, and $aR = 1.48$ nm. The parameter b is selected to contain the right dependence on cluster size in the form $\Delta\lambda \propto (N - 1)^\beta$ where β is fitted to the T-matrix simulation results giving $\Delta\lambda \propto (N - 1)^{0.55}$ and $N = \frac{D}{2R}$. The final fitted expression for the extrapolated plasmon resonance shift, $\Delta\lambda$, of clusters of 16 nm particles with respect to cluster size, D , and gap size, d , is

$$\Delta\lambda[nm] = 175[nm] \times \left(\frac{D}{16} - 1 \right)^{0.55} \left\{ \sqrt{1 + 0.43 \ln \left[1 + \frac{1.48}{d} \right]} - 1 \right\}. \quad (4.4)$$

The extrapolated model is presented in Figure 4.4 along with the T-matrix simulation results, demonstrating good agreement. The T-matrix calculations and the extrapolated model allow for the correlation of the cluster size, interparticle spacing, and the plasmon shifts reported in Table 4.1.

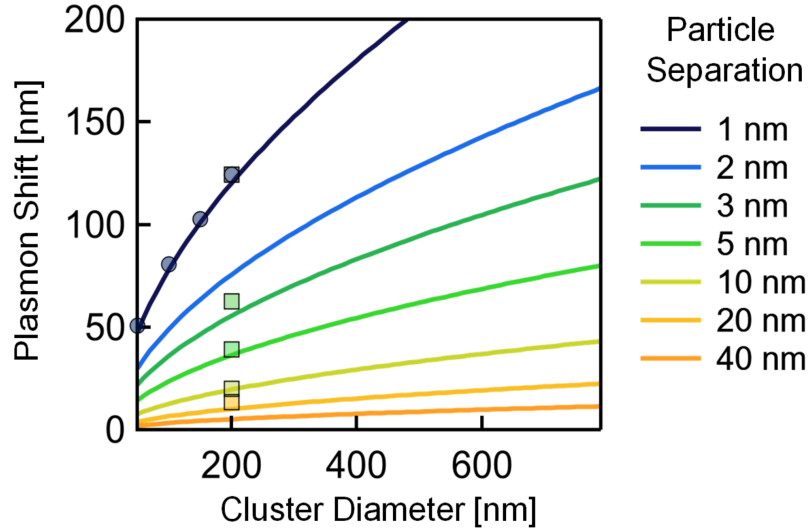


Fig. 4.4 Extrapolated model for ANT clusters in water with 16 nm particles. The circles mark the plasmon shifts from the T-matrix calculations with a fixed particle separation of 1 nm, while the squares mark the plasmon shifts for 200 nm diameter clusters with particle separations of 1, 3, 5, 10 and 20 nm.

4.3 Effects on ANT Cluster Formation

In this section, further experimental results are presented that support the proposed ANT cluster formation mechanism. The effects of PNIPAM termination, ionic strength, and excess PNIPAM suggest that electrostatic interactions play a key role in the size and plasmon shift of clusters.

4.3.1 Effects of PNIPAM Termination

It is not intuitive that the end-group of a macromolecule ($N = 49$ repeat units) would drastically change the properties of the molecule. To examine the effect of the termination group, the temperature response of the ANT clusters with PNIPAM-NH₂ and PNIPAM-SH are compared in Figure 4.5. The ANTs prepared with PNIPAM-NH₂ have very different characteristics to the ANTs coated with PNIPAM-SH in response to temperature cycling. They have a greater plasmon shift when heated, as well as a lower zeta potential, and a larger cluster diameter. The larger shift is attributed to a combination of smaller gaps in the cluster and the formation of a larger cluster overall.

At temperatures below T_c , both types of ANTs look similar with swollen shells of ≈ 20 nm, giving a total diameter of ≈ 60 nm. When heated, ANTs prepared with PNIPAM-NH₂ form much larger aggregates than those prepared with the thiolated PNIPAM, as seen in Figure 4.5d. In the aggregated state, it is expected that the particles have similar separations due to their similar initial shell thicknesses. However, using the extrapolated plasmon shift model with $D = 440$ nm and $\Delta\lambda = 30$ nm for the PNIPAM-NH₂, and $D = 150$ nm for the PNIPAM-SH with $\Delta\lambda = 4$ nm for PNIPAM-SH, it is found that the predicted gap sizes are $d \approx 10$ nm and $d > 30$ nm, respectively. This implies that the termination has an effect on both the cluster sizes and particle separations. This result can be explained by the contrasting interactions of the positively charged amines and thiols with the surface charges of the gold nanoparticles.

The zeta potentials, ζ , of the ANT clusters highlight the stark difference between the electric potentials of the particles in the clusters. It is a measure of the residual electric potential at the hydrodynamic radius of the ANT particles and clusters from the gold core surface charge. Initially the gold nanoparticles have $-\zeta = 30 \pm 7$ mV, which is greatly reduced to $-\zeta < 10$ mV after grafting the PNIPAM shell. The reduction in $-\zeta$ is

¹The data for this figure was acquired by Dr. Vladimir Turek and the SEM images were provided by Dr. Tao Ding, Department of Physics, University of Cambridge

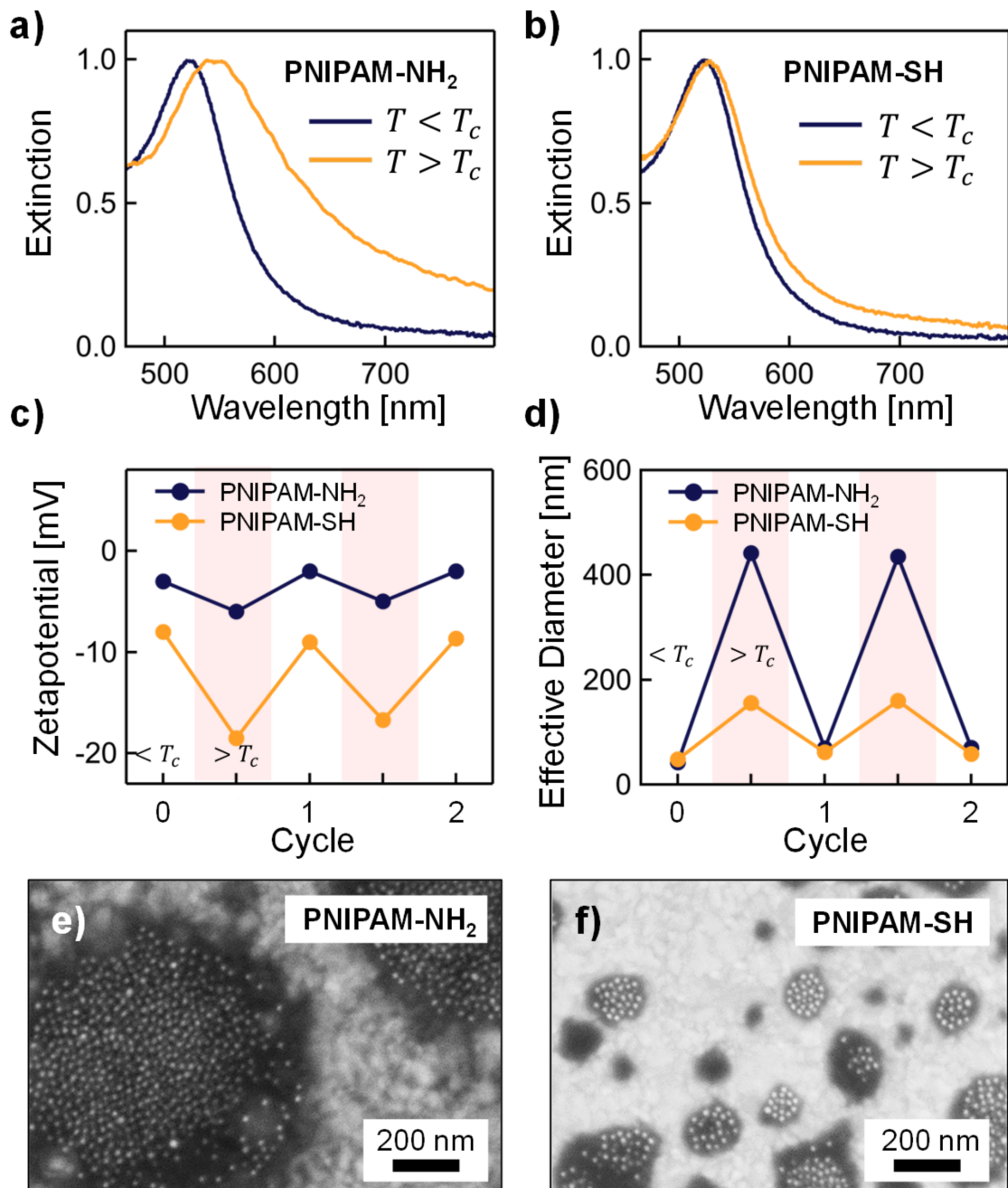


Fig. 4.5 Temperature response of ANT clusters formed with PNIPAM-NH₂ and PNIPAM-SH. a) and b) Extinction spectra of 16 nm ANTs in the hot ($T = 40^\circ\text{C}$) and cold states ($T = 25^\circ\text{C}$). c) Zetapotential and d) cluster size measurements during temperature cycling. e) and f) SEM images of hot dried aggregates formed with PNIPAM-NH₂ and PNIPAM-SH. No extra salt is added to the solutions.¹

caused the displacement of citrate molecules, the screening of the citrate charge (in the case of the positively charged PNIPAM-NH₂), and the increase in hydrodynamic radius which sets the slipping plane further from the charged gold surface. The remaining negative potentials are from trapped citrate molecules and ions bound to the gold surfaces or trapped within the PNIPAM shell.

The charge plays a role in the both assembling larger aggregates and reducing the particle separation in clusters. It is not fully understood how the termination group affects the size of ANT clusters, but it could be linked to the increase in zeta potential in the hot state (Figure 4.5c). The collapse of the PNIPAM shell surrounding the ANTs increases the zeta potentials by reducing the hydrodynamic radius and expelling screening ions from the polymer shell. During growth, it is possible that the clusters accumulate charge, which eventually limits their size due to charge repulsion effects. In this case, the positively charged PNIPAM-NH₂ is expected to better screen the negatively charged gold surface, hence allow for large clusters to form. The scanning electron microscopy (SEM) images confirm the large size difference measured by DLS in Figures 4.5e and 4.5f.

4.3.2 Effects of Ionic Strength

The importance of electrostatics in the formation of ANT clusters is demonstrated further by changing the ionic strength of the solution with the addition of known concentrations of salts. Increasing the concentration of ions in the solution decreases the Debye screening length as mobile ions diffuse to compensate surface charges. As shown in Figure 4.6, adding 50 mM of NaCl drastically increases the plasmon redshift of the clusters. Maji et al. [52] also demonstrate similar effects of salt concentration on Au@PNIPAM core-shell particles. The effect of added NaCl on the extinction saturates at a concentration near 50 mM, as shown in the inset.

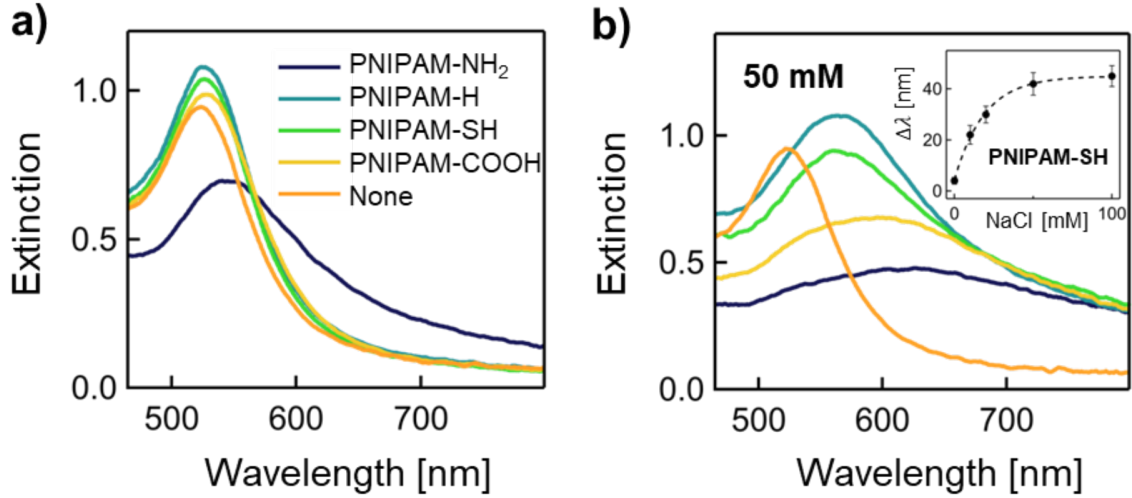


Fig. 4.6 UV-Vis extinction spectra of ANTs with different solution ionic strengths. a) Extinction spectra of ANTs using different functionalised PNIPAM without and b) with added 50 mM NaCl. The inset in the top-right of b) shows the plasmon shift, $\Delta\lambda$, as a function of NaCl concentration for ANTs prepared with PNIPAM-SH.¹

The magnitude of the redshift depends on the polymer termination, with $\text{PNIPAM-NH}_2 > \text{PNIPAM-COOH} > \text{PNIPAM-SH} \approx \text{PNIPAM-H}$. The predicted particle separations for all termination groups is greatly reduced with the increase in ionic strength. In fact the separations decrease well below what is expected from the shell thickness. The first layer of grafted chains extends a distance $L = Na\sigma^{1/3}$ for a degree of polymerisation N with back-bone spacing a and typical close-packed surface density of $\sigma \approx 0.3$ [66]. Using the variations in molecular weight described in Table 3.1, the different lengths L are approximately 8.2 nm (PNIPAM-NH₂), 7.4 nm (PNIPAM-COOH), 15 nm (PNIPAM-H), and 22 nm (PNIPAM-SH) for well solvated polymers, which is the case when $T < T_c$. Similarly, L in a poor solvent ($T > T_c$), the typical swelling ratio for the PNIPAM branches follows $\alpha = R_f(\text{cold})/R_f(\text{hot}) \approx N^{0.27}$ which approximates the swelling ratio of grafted layers $\alpha \approx L_{\text{cold}}/L_{\text{hot}}$ [88, 78]. Therefore, the expected minimum spacing between the gold particles, $2L_{\text{hot}}$, are 5.8 nm (PNIPAM-NH₂), 5.4 nm (PNIPAM-COOH), 9.0 nm (PNIPAM-H), and 12 nm (PNIPAM-SH). Agreeably, these values are smaller than the predicted spacings in Table 4.1 without added salt, but they do not agree when 50 mM NaCl is added. For instance, in the case of PNIPAM-NH₂ the predicted gap size is 2.5 nm, which is far lower than estimate from the branch lengths $2L = 5.8$ nm. To explain this discrepancy, the ability for ANTs to diffuse

¹The data for the inset in this figure was acquired by Dr. Vladimir Turek, Department of Physics, University of Cambridge

inside the clusters and displace the polymers from within the gaps are considered. The result suggests that the particles can squeeze out polymer from within the gap if the electrostatic repulsion between the gold surfaces is sufficiently small. Since the amine group partially compensates for the negative citrate charge, it can screen the repulsion between the particles and allow them to approach more closely (enhanced by their van der Waals attraction).

Zhang et al. report that the temperature response of PNIPAM is affected by specific ions according to the Hofmeister series [89]. However, as shown in Figure 4.7 the counterion does not appear to play a significant role in this system. Regardless of the sodium salt used, the extinction spectra and plasmon shifts remain consistent with $\Delta\lambda \approx 42$ nm, as reported in Table 4.1 for NaCl.

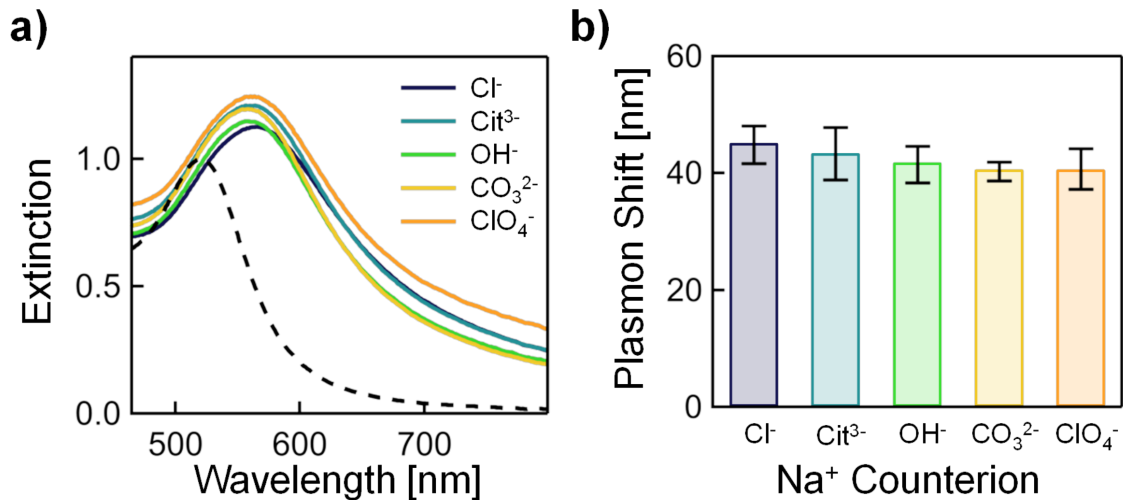


Fig. 4.7 Specific ion effects on ANT cluster formation. a) Extinction spectra of 16 nm ANTs made with PNIPAM-SH. Various sodium salts are added at a concentration of 50 mM. b) Comparison of the extinction peak shift for the different salts.

The main contribution of NaCl in this system is to reduce the screening length, which implies that the total redshift of the plasmon resonance is governed by electrostatics. The reduction in net charge on the gold cores allows them to approach more closely, while also allowing the cluster to grow larger to produce $\Delta\lambda > 100$ nm strongly redshifted resonances even for such small plasmonic particles.

4.3.3 Effects of Excess PNIPAM

The need for excess PNIPAM is still an outstanding question that must be discussed. Even for the PNIPAM-NH₂ there seems to be an optimum concentration of 0.11 g L⁻¹ for the plasmon redshift, as demonstrated in Figure 2.6. Jones et al. also reported that the flocculation of Au@PNIPAM particles only occurs in the presence of free PNIPAM (PNIPAM_{aq}) strands in solution [48]. However, as presented in Figure 4.8, PNIPAM_{aq} is not required to achieve large plasmon shifts when the solution ionic strength is sufficiently high.

In this case, excess PNIPAM is removed by repeated centrifugation. A negligible optical response is observed for the ANTs without 50 mM NaCl nor excess PNIPAM. When the excess PNIPAM is left in the solution, the extinction of the solution increases with temperature. This effect is observed with and without added NaCl or even without ANT particles, as the free PNIPAM aggregates above T_c to form scattering colloids. When the excess PNIPAM is removed and 50 mM of NaCl is added, strong plasmonic shifts are observed with heating. This implies that excess PNIPAM is not required for aggregation, which is helpful for applications where having excess PNIPAM in solution is not feasible, such as in physiological conditions.

4.4 Conclusion

In summary, as reported in previous literature, the reversible aggregation of ANTs is caused by the increase in hydrophobic and cohesive interactions of PNIPAM when heated above the critical temperature. However, it is now clear that the internal structure and size of the clusters depend greatly on the local charges of the particles within the aggregates. High ionic strengths, and charged PNIPAM terminations help screen the surface charges. This enables the particles to approach closer within the clusters and increases the overall cluster size. These effects work in conjunction to increase the plasmonic resonance shift of the clusters. This optical response is captured in a proposed analytical model that is based on the size and separation of coupled plasmonic chains. Although these findings rely on the observed plasmonic response of the solution, they are also applicable much more generally to polymer-assisted colloidal self-assembly.

¹The data for this figure was acquired by Dr. Vladimir Turek, Department of Physics, University of Cambridge

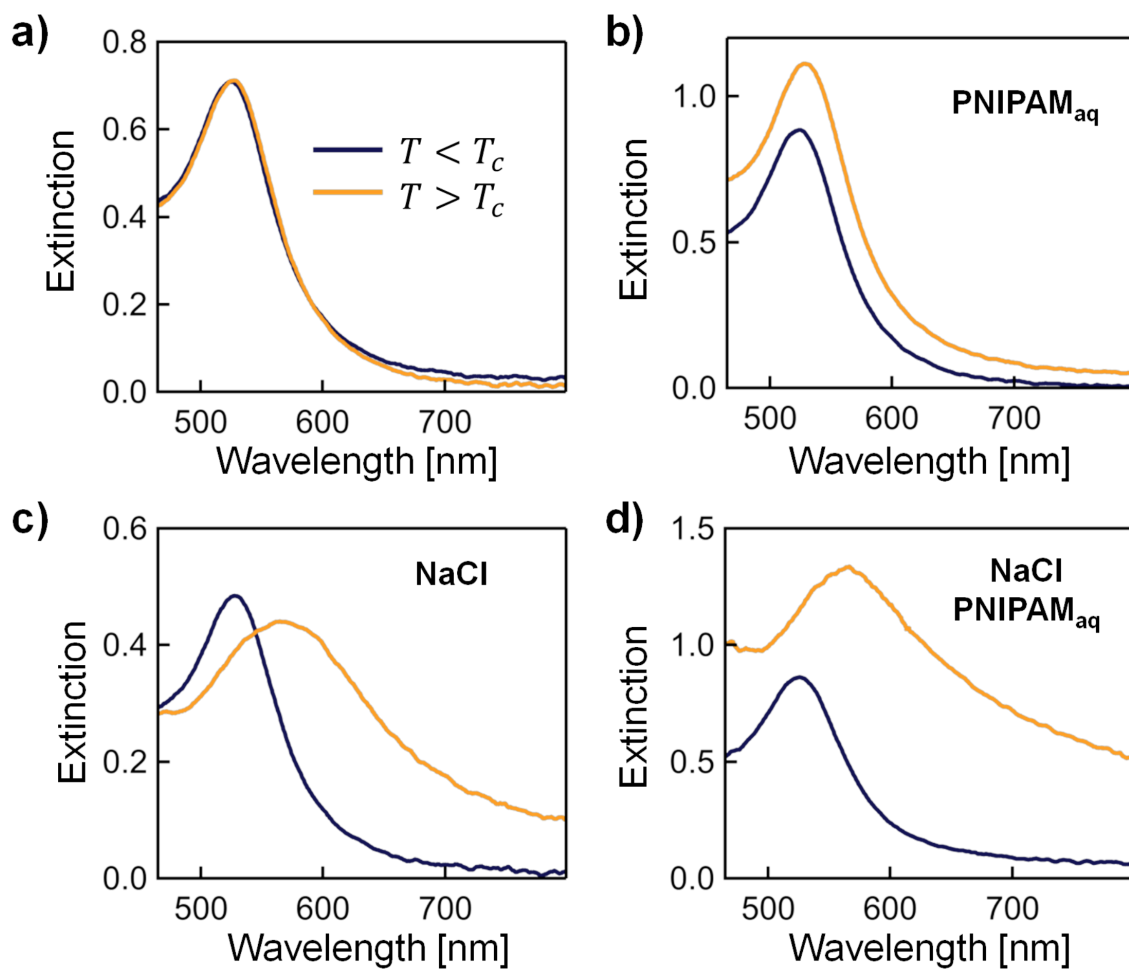


Fig. 4.8 Effect of excess PNIPAM on the optical response of ANT clusters prepared with PNIPAM-SH. a) Extinction spectra of ANT clusters without NaCl or free PNIPAM_{aq} (removed by repeated centrifugation), and b) with excess PNIPAM_{aq} but no NaCl. c) Extinction spectra with 50 mM NaCl, but without excess PNIPAM_{aq} and d) with excess PNIPAM_{aq}.¹



5. ANT on Mirror

This chapter describes the mechanical characteristics of individual ANT particles using a plasmonic geometry designed for the simultaneous probing and actuation of the particles with light. The structure consists of a plasmonic particle positioned above a metal film with a sufficiently small separation for plasmonic coupling. In general, this system is called the Nanoparticle on Mirror (NPoM) structure, and here the term ANT on Mirror (ANToM) is used to specifically describe NPoM structures made with ANT particles.

First, the relevant theory for the key properties of the ANToM geometry are described. Then, the collective reversible switching behaviour of the ANToM structures is demonstrated when controlled with temperature, followed by the local light-induced switching of individual ANToMs. The response of the ANToM structures is compared to simulations to extract the changes in the PNIPAM shell thickness as well as the characteristic forces and efficiencies of the actuation. Finally, the potential use of the NPoM geometry for giving insight into the dynamics of other switchable polymeric nano-shells is highlighted with electronically modulated polymers.

5.1 ANT on Mirror Structure

The NPoM geometry consists of a plasmonic nanoparticle, typically 40-100 nm in diameter, deposited on a flat plasmonic substrate, where the spacing, d , between the nanoparticle and the substrate is much smaller than the radius of the nanoparticle (typically $d < \frac{R}{2}$). The close proximity of the nanoparticle and substrate creates a plasmonic cavity that supports plasmonic coupled modes between the nanoparticle and its induced image charge in the substrate [90, 91, 71].

A schematic of an ANToM structure with scanning electron microscopy (SEM), dark-field spectroscopy, and dark-field (DF) microscopy characterisation are shown in Figure 5.1. Unlike in previous chapters, 80 nm gold particles are used instead of the 16 nm particles. Larger nanoparticles have greater scattering cross-sections, which

enhances their brightness in DF microscopy. This facilitates the optical characterisation of individual ANT particles.

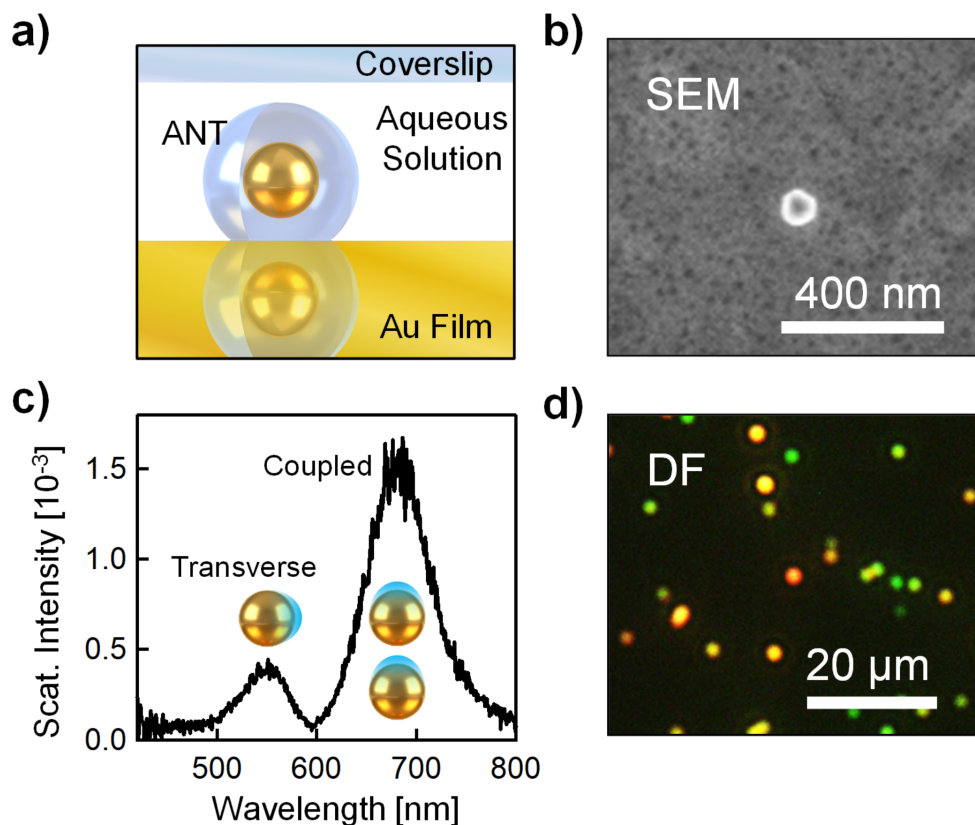


Fig. 5.1 ANToM sample characterisation. a) Schematic of an individual particle on an ANToM sample. The ANToM samples are submerged in an aqueous solution of 50 mM NaCl and sealed under a coverslip. b) Scanning electron microscopy (SEM) image of an individual ANToM. c) Scattering intensity spectrum of a typical ANToM structure at room temperature, and d) 100x DF microscope image of ANToM structures. The two peaks in the scattering spectrum are associated with the transverse and coupled plasmonic modes, as labelled.

Samples are prepared by sparsely drop-casting ANT suspensions on template-stripped gold substrates. The suspension is quickly rinsed away with de-ionised (DI) water and dried with a nitrogen gun. The preparation of ANT suspensions with amine-terminated PNIPAM and the template-stripped gold are discussed in detail in Section 3.1.

The ANToM structures are submerged in an aqueous solution with 50 mM NaCl and protected with a microscope coverslip. SEM imaging is used to confirm that

the structures consist of well distributed individual ANT particles with an average spacing greater than 10 μm , such that NPoM structures are non-interacting and can be individually addressed optically. The SEM technique does not resolve the thin PNIPAM coatings on the ANT particles, but it reveals the faceted nature of the particles. There are many geometries for gold nanoparticles which impact the plasmonic properties of the NPoM structure as highlighted in the work published by Benz et al. [71].

Figure 5.1c and 5.1d show a typical dark-field spectrum and image of the ANToM structures. The spectra contain two characteristic peaks near the wavelengths of 550 nm and 700 nm. The peak near 550 nm is associated with the transverse plasmon resonance mode of the ANT particle and is observed regardless of the underlying substrate, whereas the peak near 700 nm is ascribed to the lower energy coupled mode between the ANT particle and the underlying gold substrate. The ANToM structure can support many other higher-order modes, but these generally occur at higher energies and have lower radiative efficiencies. Therefore, the ANToM scattering spectra are dominated by the transverse mode and the coupled mode.

In comparison to the transverse mode, the coupled mode exhibits greater sensitivity to its local structure and environment. Changes in particle type, size, shape, and the refractive index of the surrounding medium, significantly affect the coupled mode. In particular, the coupled mode is extremely sensitive to changes in the refractive index and size of the gap between the particle and the substrate [92–94, 59]. The size of the gap is defined by the thickness of the PNIPAM shell. Since, the size of the PNIPAM coating is not precisely controlled, there is significant variation in the coupled mode position between ANToM structures and the effective colour of the particles observed by microscopy.

The plasmonic properties of the NPoM structure are analogous to that of a nanoparticle dimer for the half-space $Z > 0$, as shown in Figure 5.2. Both configurations exhibit confined volumes with strong field enhancement when excited at particular frequencies and polarisations. These local volumes of confined light are referred to as hotspots.

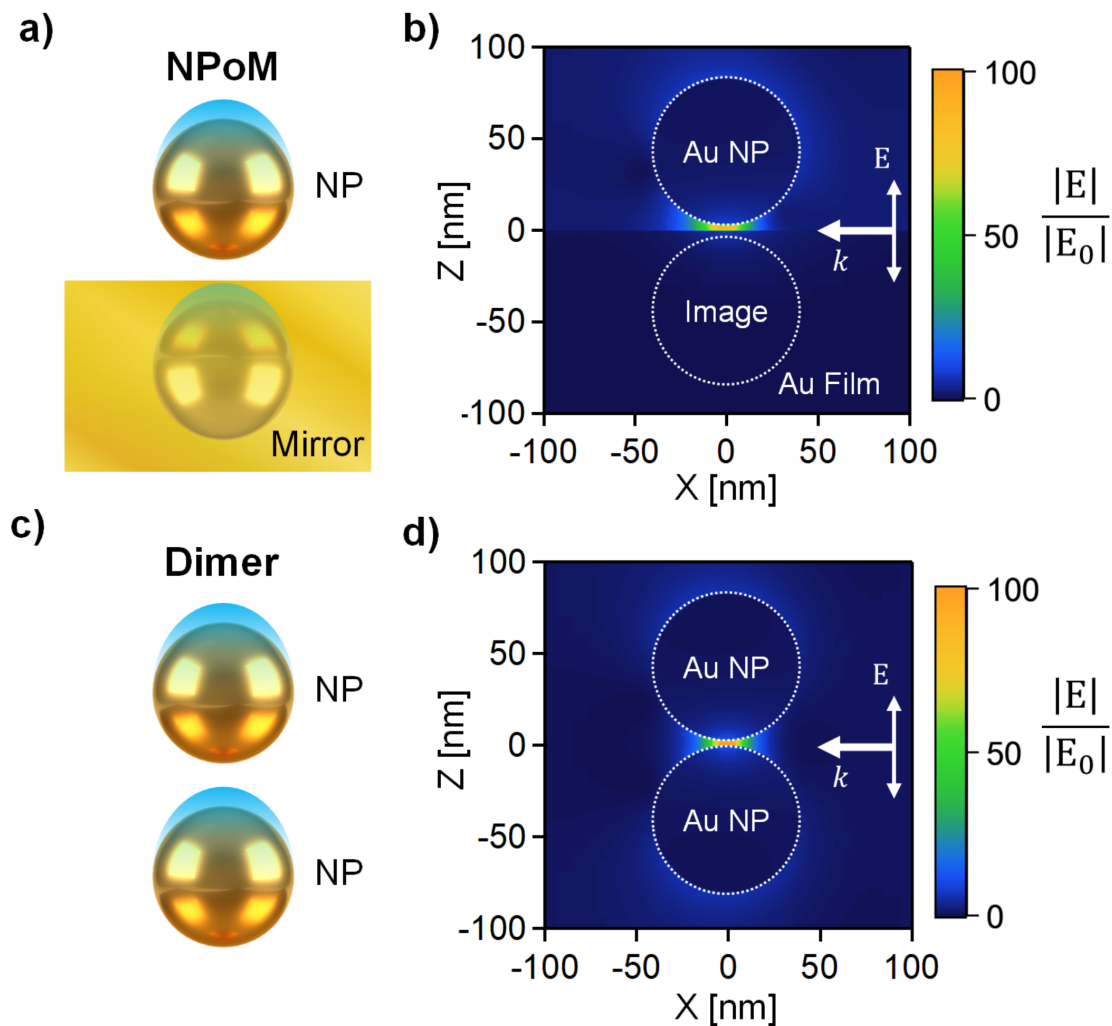


Fig. 5.2 Comparison of the plasmonic coupling between NPoM and dimer structures. a) and c), Schematics of the plasmonic structures. b) and d), FDTD simulated near-field enhancement at resonance for the NPoM and dimer structures. The gold nanoparticles are 80 nm in diameter and the gap is 3 nm for both structures. The near-field enhancement was calculated at a wavelength of 730 nm for the NPoM and 700 nm for the dimer.

Although, dimer and NPoM structures share many similarities, there are some key distinguishing features. The predominant advantage of NPoM structures is the ease of fabricating the structures with single plasmonic cavities. A major drawback, however, is the fixed orientation of the NPoM structure. The coupled antenna mode oscillates along the normal of the film and hence, radiates orthogonally to the film's normal. This fixed orientation makes it more challenging to excite the coupled mode

of NPoM geometry using conventional microscopy techniques. In comparison, the dimer structures can be orientated horizontally to the collection and incident angles for effective excitation of the coupled mode. Fortunately, due to the large difference in dielectric permittivity between the plasmonic film and the surrounding medium of nanoparticle, the far-field emission pattern of the coupled mode bends towards the incident and collection areas, as shown in Figure 5.3.

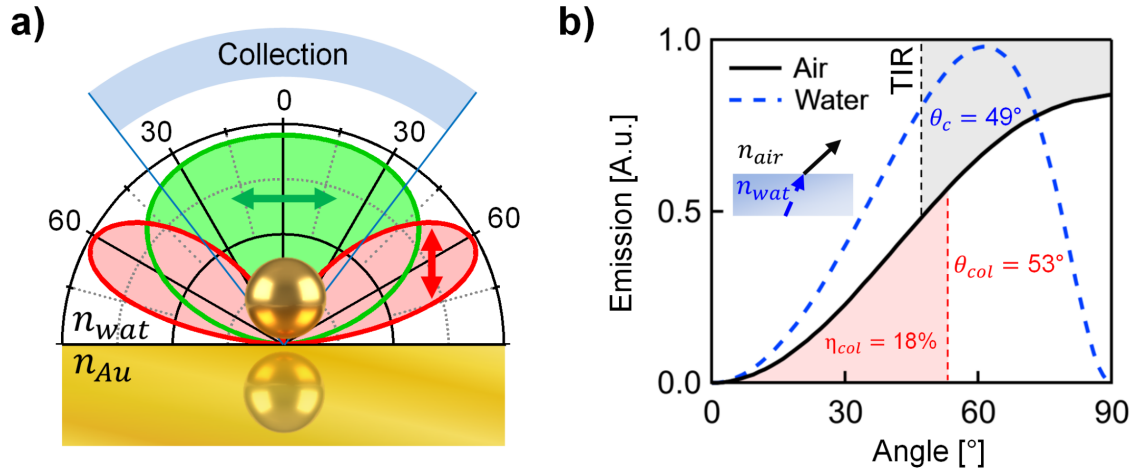


Fig. 5.3 Emission angles and collection of the dominant radiative plasmonic modes of an ANToM structure submerged in water. a) Normalised angular emission power calculated at 550 nm (green) and 730 nm (red), with horizontal and vertical dipole orientations resonant with transverse mode and coupled modes, respectively. The effective collection angle of the 100x DF objective used and a schematic of the ANToM structure is overlaid. b) Angular emitted power of the coupled mode corrected for transmission from water to air and total internal reflection (TIR) at emission angles greater than the critical angle, $> \theta_c$. For collection using a 100x DF objective with $NA = 0.8$ (i.e. $\theta_{col} = 53^\circ$), integrating the emitted power below the maximum collection angle gives an optimum collection efficiency of $\eta_{col} = 18\%$.

The bending of the emission pattern is estimated by modelling the NPoM structure as a radiating dipole at the interface of two continuous phases with different dielectric constants (n_1 and n_2 , respectively) where $n = n_2/n_1$. W. Lukosz [95] derived these emission patterns in terms of power, P , for arbitrarily oriented radiating electric dipoles in the half-space $Z > 0$ for both s - and p -polarisations,

$$P_p(\alpha_1, \alpha_2, \phi, \theta) = \frac{3}{2\pi} \frac{\cos^2 \alpha_1 (n \cos \theta \sin \alpha_1 - \sin \theta \cos \phi \cos \alpha_2)^2}{(n \cos \alpha_1 + \cos \alpha_2)^2}, \quad (5.1)$$

and

$$P_s(\alpha_1, \alpha_2, \phi, \theta) = \frac{3}{2\pi} \frac{\cos^2 \alpha_1 \sin^2 \theta \sin^2 \phi}{(\cos \alpha_1 + n \cos \alpha_2)^2}, \quad (5.2)$$

where θ is the dipole orientation, ϕ is the azimuth angle, α_1 is the angle between the normal of the interface and the propagation direction vector of the radiation, and α_2 is the transmitted angle into the second medium defined by $n \sin \alpha_2 = \sin \alpha_1$. These equations are valid for $0 \leq \alpha_1 \leq \frac{\pi}{2}$ for $n > 1$ and $0 \leq \alpha_1 \leq \alpha_{1,c}$ for $n < 1$, where $\alpha_{1,c} \equiv \arcsin(n)$ is the critical angle. Therefore, for the case of a radiating dipole at the interface of water and gold $n < 1$, and for the angles $\alpha_{1,c} \leq \alpha_1 \leq \frac{\pi}{2}$ the radiation patterns are

$$P_p(\alpha_1, \phi, \theta) = [\cos^2 \theta \sin^2 \alpha_1 + n^{-4} \sin^2 \theta \cos^2 \phi (\sin^2 \alpha_1 - n^2)] g_p(\alpha_1), \quad (5.3)$$

and

$$P_s(\alpha_1, \phi, \theta) = [\sin^2 \theta \sin^2 \phi] g_s(\alpha_1), \quad (5.4)$$

where $g_s(\alpha_1) = \frac{3}{2\pi} (1 - n^2)^{-1} \cos^2 \alpha_1$ and $g_p(\alpha_1) = n^2 [(1 + n^{-2}) \sin^2 \alpha_1 - 1]^{-1} g_s(\alpha_1)$ [95]. Since the ideal NPoM structure is azimuthally symmetric, the angle $\phi = 0$ is set and the radiated s -polarisation reduces to zero for all projection angles, α_1 , and dipole orientations, θ . Now the emission pattern can be re-written as

$$P(\alpha_1, \alpha_2, \theta) = \begin{cases} \frac{3}{2\pi} \frac{\cos^2 \alpha_1 (n \cos \theta \sin \alpha_1 - \sin \theta \cos \alpha_2)^2}{(n \cos \alpha_1 + \cos \alpha_2)^2}, & 0 \leq \alpha_1 < \alpha_{1,c} \\ [\cos^2 \theta \sin^2 \alpha_1 + n^{-4} \sin^2 \theta (\sin^2 \alpha_1 - n^2)] g_p(\alpha_1), & \alpha_{1,c} \leq \alpha_1 < \frac{\pi}{2}. \end{cases} \quad (5.5)$$

From equation 5.5, the emission patterns are plotted for the traverse mode with a horizontal dipole ($\theta_{\perp} = 0^\circ$) and the coupled mode with a vertical dipole ($\theta_{\parallel} = 90^\circ$). Note that the refractive index of water is relatively constant in the visible regime, near $n_{wat} = 1.33$, while the different gold refractive indexes at the appropriate resonance wavelengths for each mode must be taken into account. From the polar plot in Figure 5.3a, it is observed that the traverse mode is emitted diffusely in the vertical direction, while the coupled mode emits at higher angles with maximum intensity near 62° .

Although the model holds well for an ideal NPoM structure, it does not account for the effects of surface roughness and particle faceting. These break the azimuthal symmetry of the NPoM structure and may broaden the emission angles. Currently, there are no theoretical models directly relating nanoparticle facet properties to their

NPoM emission angles. However, the model can be used to estimate the maximum collection efficiency of the ANToM structures. Using real parameters from the DF microscopy setup as described in Section 3.3.3, the maximum collection angle for a 100x DF objective with $NA = 0.8$ is $\theta_{col} = 53^\circ$. It is also important to consider that the light is emitted into an aqueous solution and collected in air. Therefore, the emitted angles are further shifted to higher angles, as the light is transmitted from the aqueous phase, through the coverslip, and into air before collection. Using Snell's law, $n_1 \sin \theta_1 = n_2 \sin \theta_2$, the highest emission angle that is collected is $\theta_{col}^* = 34^\circ$. This gives a maximum collection efficiency of $\eta_{col} = 18\%$ from integrating the emitted intensity within the collection area. Although, most of the emitted light from the coupled mode is lost, it remains easier to optically resolve the coupled mode than the traverse mode due to the large field enhancement in the NPoM hotspot.

5.2 Numerical Modelling of ANToM

The ANToM geometry is used to measure the actuation stroke length and speed of individual nanoparticles, which relate to the force and efficiency of these nano-actuators. However, these measurements are only possible by correlating the change in thickness of the PNIPAM shell with the plasmonic response of the ANToM structure. Here, the change in thickness of the PNIPAM is expressed as a changing gap spacing between the gold nanoparticle core and the gold substrate.

The scattering cross-sections of ANToM structures with different gap sizes are simulated with a finite-difference time-domain (FDTD) model using Lumerical solutions, as shown in Figure 5.4. The calculations are performed with an 80 nm gold nanoparticle on a 100 nm thick gold film with gap spacings varying from 1 to 20 nm. The particles are surrounded by a 20 nm PNIPAM cladding. The dielectric function of gold is interpolated from Johnson and Christy [8], while the PNIPAM refractive index is set to $n = 1.34$ for the cold state and $n = 1.42$ for the hot state [67]. The calculations use a broadband plane-wave source incident parallel to the gold film and polarised normal to the film. This orientation of the incident light efficiently excites the coupled plasmonic resonance of the ANToM structure.

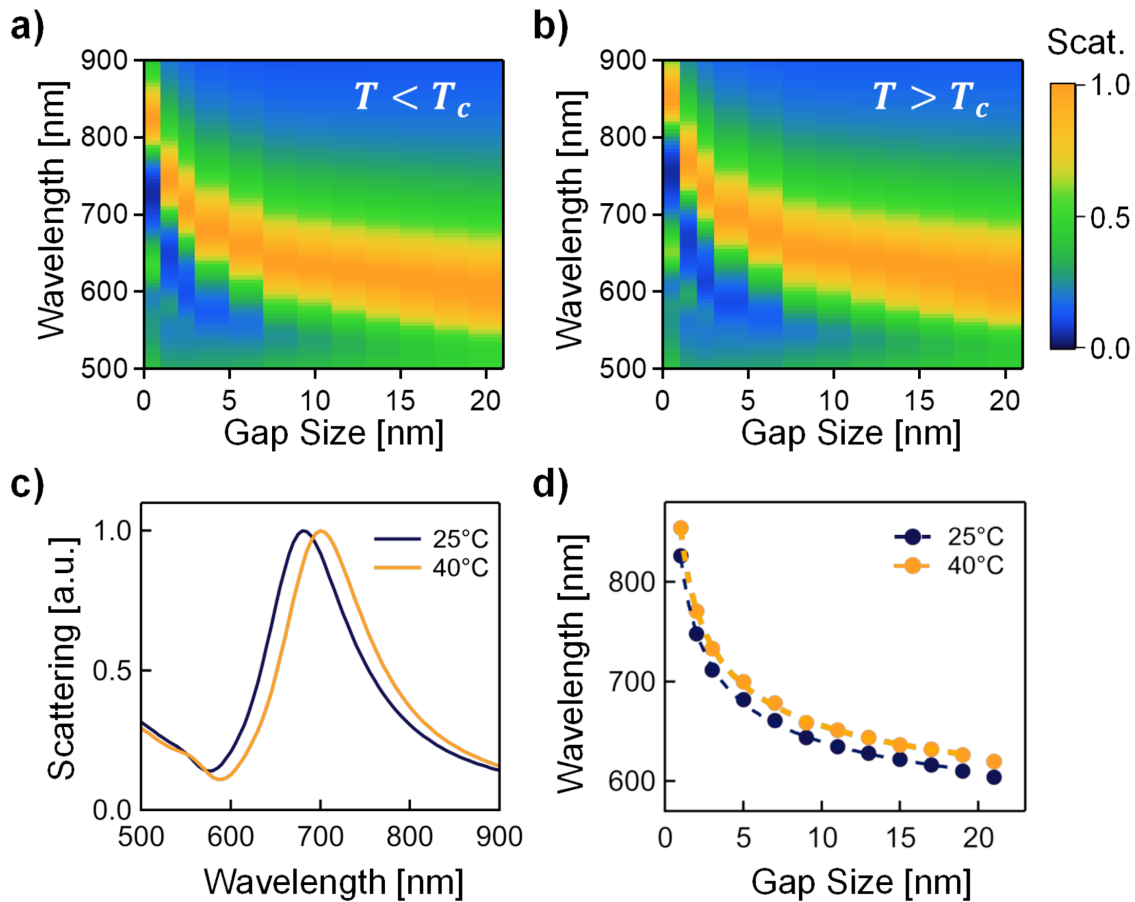


Fig. 5.4 Simulated scattering from FDTD simulations of ANToM for different gap sizes. a) and b) Scattering spectra maps of ANToM structures with PNIPAM claddings of varying thickness with $T < T_c$ ($n=1.34$) and $T > T_c$ ($n=1.42$). c) Scattering spectra of an ANToM structure with a fixed 3 nm gap at 25°C and 40°C. d) Plasmon resonance wavelength of ANToM coupled mode with different gap sizes at 25°C and 40°C.

The FDTD modelling shows the sensitive plasmonic response of the ANToM structure with gap sizes below 20 nm. While the change in PNIPAM refractive index is shown to only have a minor effect on the coupled plasmons, giving redshifts of less than 15 nm, as shown in Figure 5.4c [90]. The combination of these contributing factors to the plasmon shift is summarised in Figure 5.4d. The correlation of gap sizes and plasmonic resonances effectively creates a nano-ruler that estimates the gap sizes of ANToM structures from their optical signatures.

These calculations assume that the gold particle and PNIPAM shell are spherical and the gold mirror is perfectly flat. In reality, the faceting of ANT particle gold cores and variance of the PNIPAM shells between ANT particles is uncertain. Due to

the lack of available theory and experimental means to characterise and correlate the exact geometries of the ANToM structure, measurements are compared to this ideal model. However, the effects of nanoparticle faceting on the plasmonic coupled-mode resonance can be examined using the FDTD simulations. Here, the facet at the base of the gold particle is modelled by cutting the bottom of the spherical particle to make a circular facet. As presented in Figure 5.5, increasing the amount cut off from the sphere base increases the facet width, w . The FDTD simulations show that the resonance wavelength redshifts from 740 to 785 nm as the bottom facet grows until a critical size, where the resonance begins to blueshift. The blueshift is attributed to the decrease in the overall size of the NPoM antenna structure.

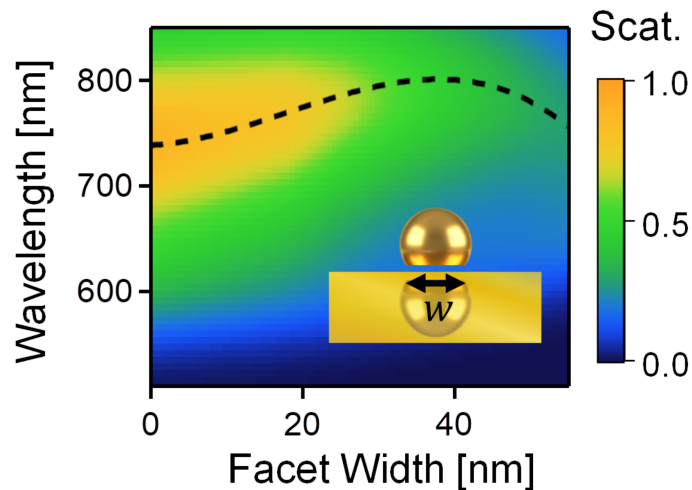


Fig. 5.5 FDTD-simulated scattering spectra as a function of nanoparticle facet size. The diameter of the spherical particle is fixed at 80 nm while the base of the sphere is cropped to generate a circular facet at the bottom of the nanoparticle. The gap between the nanoparticle and the mirror is set to 3 nm. The dashed line marks the coupled plasmon resonance.

In previous work with the NPoM geometry using self-assembled monolayers to form well-defined gaps between 80 nm gold nanoparticles and a gold mirror, it has been predicted that the bottom facet width generally ranges from 20 to 40 nm [71]. This facet size does not scale linearly with the size of the particle, since different crystal structures are more prominent for different sizes. Although, it is evident that the faceting of the nanoparticle plays a role in the peak position of the coupled mode, currently there are no simple methods to determine the facet properties and orientation of the ANT particles as they deposit on the surface. Therefore, ANT particle gold cores are assumed to be spherical.

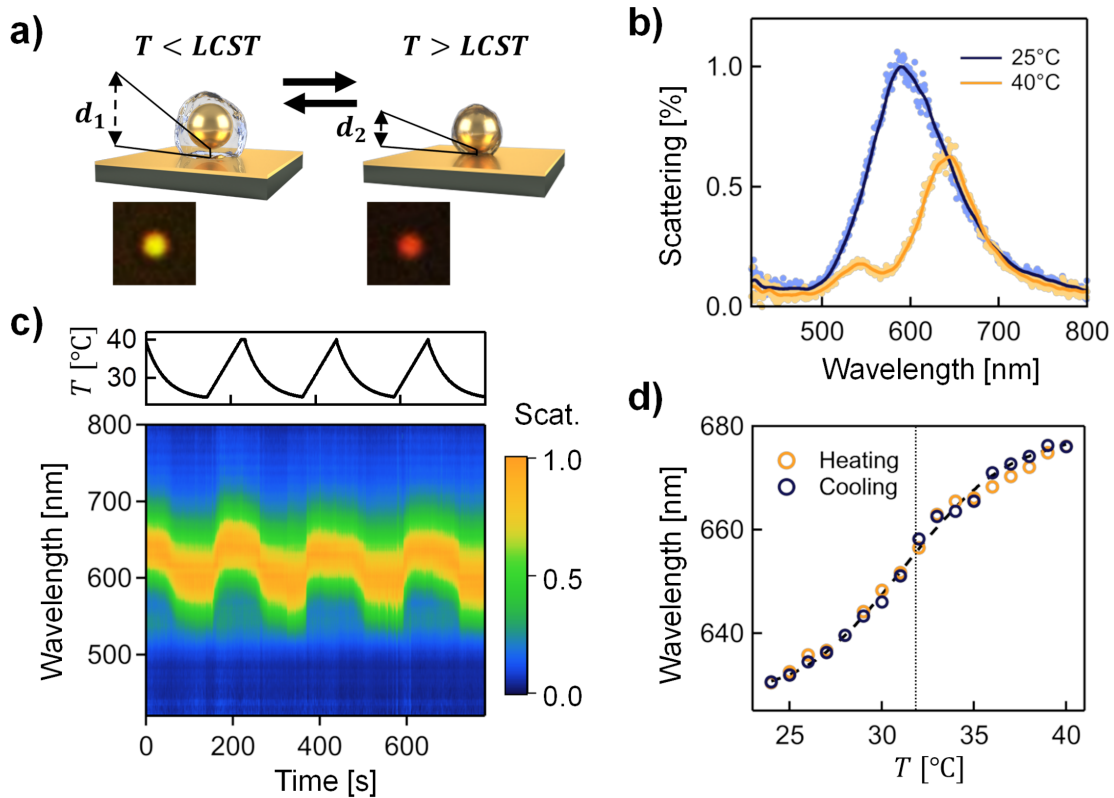


Fig. 5.6 Thermally-induced switching of the coupled plasmon resonances in ANToM structures. a) Schematic switching and dark-field images ($3 \times 3 \mu\text{m}$) at 25°C and 40°C. b) Scattering spectra of ANToM at 25°C and 40°C. c) Scattering spectra map over time with reversible switching of coupled plasmons with several temperature cycles. d) Plasmon resonance wavelength response to stepwise heating and cooling with a 1 minute equilibration time for each step. The dashed line is a polynomial fit for the coupled mode resonance and the vertical dotted line marks the critical temperature T_c .

5.3 Heat-induced Switching

The ANToM structures actuate individually with focused light or collectively with bulk heating. Heating the entire sample from 25°C to 40°C switches the dark field image of a typical ANT from red to green or green to red depending of the thickness of the PNIPAM, as shown in Figure 5.6. The coupled plasmon resonance of the ANToM redshifts from 590 to 645 nm, demonstrating that the thermoresponsive actuation of PNIPAM indeed changes the gap size.

Using the FDTD simulation results in Figure 5.4d, the gap size is estimated from the coupled mode peak position. It is found that the gap size, d , decreases from

$d_1 = 21 \pm 2$ nm to $d_2 = 12 \pm 1$ nm upon heating above T_c . Cooling down the sample to 25°C causes the coupled plasmon resonance to switch back to its initial state. This can be reproduced for many cycles as shown in the scattering spectra map in Figure 5.6c. This indicates that the PNIPAM shell can re-swell inside the plasmonic cavity, resulting in good reversibility for this system. In addition, it is demonstrated that the high sensitivity of the plasmonic resonance to the gap size provides an effective measure for the thickness of ANT particle shells.

Interestingly, the step-wise heating and cooling of the sample between 25°C and 40°C shows slow redshifting of the coupled mode with temperature in Figure 5.6d. Usually PNIPAM systems show sharp transitions over $\approx 2^\circ\text{C}$ around the critical temperature, T_c . This may suggest that PNIPAM confined in the NPoM gap behaves differently than in bulk systems. The surface confinement of the PNIPAM and considerable van der Waals pressure in the gap may be responsible for such effects.

5.4 Light-induced Switching

Alternatively to heating samples, individual ANToMs can be locally switched using a focused irradiation. This is achieved with a 447 nm pump laser, which is easily spectrally filtered from the coupled-mode resonance and excites the interband transitions of the gold nanoparticle cores for efficient heating. Faster switching rates are achieved using light, because the temperature changes occur over much smaller volumes. The switching of an ANToM structure is demonstrated in Figure 5.7.

The coupled plasmon resonance reversibly shifts between 655 and 710 nm as the laser is modulated on and off. The change in plasmon resonance is indicative of changes in the cavity size. In this case, the size oscillates between $d_1 = 7 \pm 1$ nm and $d_2 = 4 \pm 1$ nm, when the pump laser is off and on, respectively. The difference in plasmon wavelengths of the ANToM structures in Figure 5.6 and 5.7 is caused by differences between the individual structures, such as the shell thickness, and the nanoparticle size and faceting [71].

Similar to the case with bulk heating, the actuation driven by light-induced heating is reversible. The dynamics of switching in Figure 5.7c reveals both fast and slower effects. The slow effect is likely caused by the accumulation of residual PNIPAM in solution onto the ANToM structure. The effect of laser power in Figure 5.7d shows that there is a minimum power to sufficiently heat the ANToM structures. However,

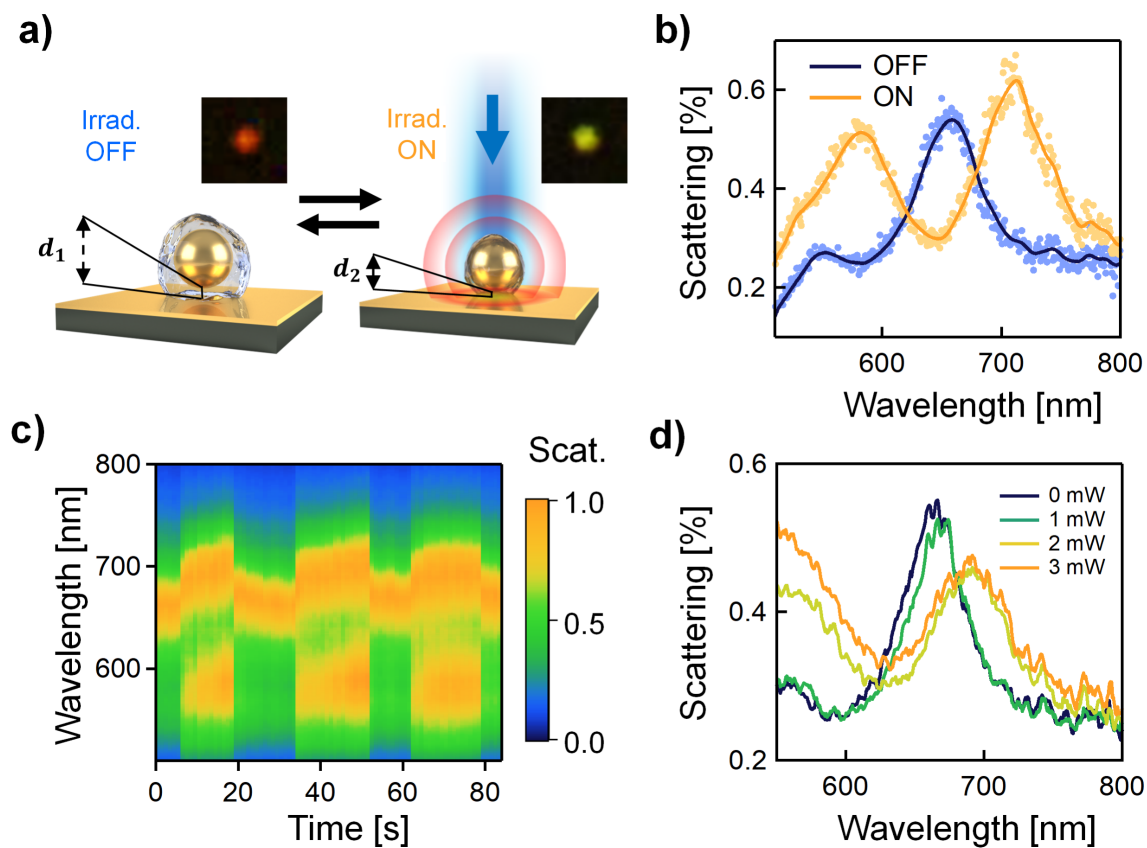


Fig. 5.7 Light-induced oscillation of an individual ANToM structure biased at 29°C. a) Schematic of switching for a laser-irradiated ANToM structure, insets show corresponding dark-field images ($3 \times 3 \mu\text{m}$) in the hot and cold states. b) Scattering spectra with laser irradiation on and off. c) Scattering spectra over time with 3 on/off irradiation cycles. d) Scattering spectra with increasing irradiation powers.

there is also a high power limit since the laser can damage or restructure the polymer coating [96–98]. This is discussed in greater detail in Section 5.4.1.

The ANToM switching is much faster than typical PNIPAM systems, which mostly transition with timescales on the order of seconds to minutes [99, 100]. The speed is measured by modulating the CW pump laser at a set frequency, while recording changes in the plasmon resonance, as shown in Figure 5.8. The pump modulation frequency is limited to 90 Hz by the detector exposure time, because at higher frequencies the amount of scattered light from the ANToM structure is reduced. However, the sub-millisecond half-cycles observed are already much faster than current molecular machines, and it is understood that the actuation of PNIPAM can be extremely fast for nanoscale volumes [101]. Murphy et al. reported PNIPAM re-swelling times < 100 ns for 13 nm gold nanoparticles coated with 85 nm PNIPAM shells in response to 10 ns light pulses [60].

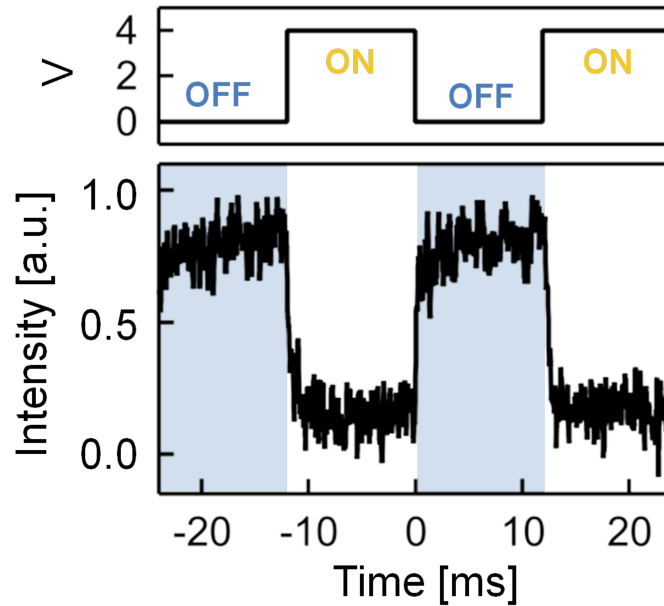


Fig. 5.8 High-speed ANToM oscillation with a laser modulated with a drive voltage. The dark-field scattering intensity is spectrally integrated over $550 \text{ nm} < \lambda < 650 \text{ nm}$.

The fast response of the ANToM structure is mainly due to local laser-induced heating and rapid cooling inside the sub-20 nm gap volumes, which allows water to rapidly swell the PNIPAM [102]. The heated volume can be approximated by the area heated by the irradiation of a gold nanoparticle. The thermal diffusion length, l_d , of water that is significantly heated around the particle is given by

$$l_d = \sqrt{\tau D_m}, \quad (5.6)$$

where D_m is the thermal diffusion coefficient $D_m = \frac{\Lambda_m}{C_m}$, C_m is the heat capacity (per unit volume) of water, and Λ_m its thermal conductivity. The characteristic cooling time, τ , of the particle is

$$\tau = \frac{R^2 C_{\text{NP}}^2}{9 C_m \Lambda_m}, \quad (5.7)$$

given the heat capacity of the nanoparticle, C_{NP} [19]. This gives a cooling time of $\tau \approx 430$ ps for 80 nm gold particles and a thermal diffusion length in the water of $l_d \approx 8$ nm. For the ANToM structure, the gold substrate can improve this cooling rate as the heat is more rapidly dissipated inside the gold substrate than in water. However, in the cold state, ANT particles with thicker coatings are essentially thermally decoupled from the substrate since $l_d < d$. Other effects such as thermofluidic forces and nanoscale convection are not accounted for here as they are not well studied in such nanoscale geometries.

5.4.1 Light-induced Damage

Although, light-induced switching is observed, the ANToM system is less robust when switched with light in comparison to bulk heating. The power needed to heat the constructs is on the same order as the irreversible damage threshold. The response of the ANToM structures under continuous irradiation over time is shown in Figure 5.9. Consistent spectral drifts are observed for three similar ANToM structures with irradiation powers of 2.5 mW, 5.0 mW, and 7.5 mW. This drift is likely caused by the deformation of the gold cores. This effect has been reported before at the similar irradiation powers with 80 nm gold particles deposited on various 2D materials and SAM layers by Mertens et al. [96].

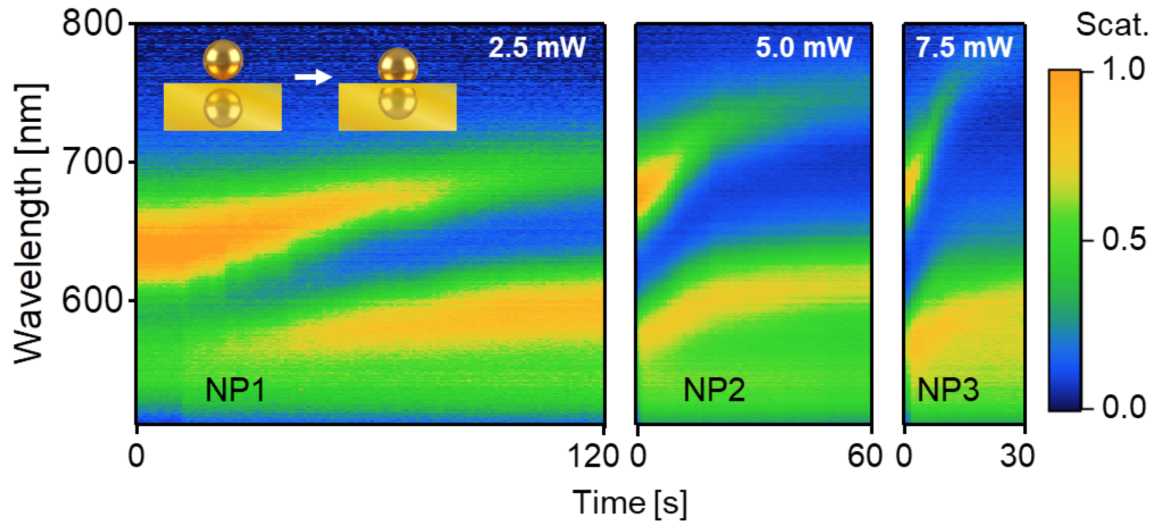


Fig. 5.9 Scattered spectra map over time of three ANToM structures under continuous 447 nm irradiation at 2.5 mW, 5.0 mW, and 7.5 mW. The laser is focused to a 2 μm spot. The inset schematic depicts the growing facet at the bottom of the nanoparticle due to light-induced damage.

A significant, slow redshift is observed in the coupled mode over time while under irradiation. The rate of irreversible redshifting is accelerated with increasing power. Further irradiation and higher powers can generate new modes or completely extinguish the scattered signal in the visible range [96]. The threshold power as well as the extent and rate of shifting varies between individual particles. It is predicted that there is a correlation between the combination of gap size and facet properties of the particles, and their threshold power for damage.

Damage to the PNIPAM shell could also explain the irreversible change in response to light. Aibara et al. [103] reported the irreversible transition of the PNIPAM shell for 100 nm Au@PNIPAM particles with irradiation power ($3.5 \text{ mW } \mu\text{m}^{-2}$, $\lambda = 488 \text{ nm}$), which is similar to the damage threshold observed in the case of ANToMs. The cause of this irreversible switch is unknown, but it is suggested that thermally-induced flows could displace the shell strands within the gap or vitrification of the shell could occur. Interestingly, this irreversible change is not observed for ANTs dispersed in solution when they are irradiated under the same conditions.

5.5 ANT Force and Efficiency

An estimate for the forces generated from the fast expansion of the ANTs is found by considering the state just after the PNIPAM cools below T_c . At this moment, the $t = 21$ nm thick PNIPAM layer is elastically squeezed down to $d = 12$ nm with maximum strain $e = (t - d)/t = 40\%$ which exerts a strong vertical force (Figure 5.6). This resulting force is estimated as $F = Y_{cold}\sqrt{R}(t - d)^{1.5}$ [49, 104], where $Y_{cold} = 1.8$ MPa is the Young's modulus of PNIPAM in the cold state [99]. For a 80 nm diameter particle with a 21 nm PNIPAM coating, the forces during the oscillation are ≈ 0.3 nN, directed away from the substrate. Forces on this order of magnitude are required to overcome the van der Waals attraction between the gold nanoparticle and the substrate. For the small gaps and large nanoparticles, the van der Waals attraction force, F_{VdW} , for a spherical particle of radius R is approximated by $F_{VdW} = \frac{A_H}{6d^2}$ [105], where A_H is Hamaker constant ($A_H = 2.5$ eV) and d is the gap size [106, 107]. For the ANToM structure in Figure 5.7, the gap size is $d = 4$ nm. This gives an attractive force of $F_{VdW} \approx 0.2$ nN, which is overcome by the shell expansion.

In addition to the force calculations, the work done and energy efficiency of the nano-oscillating system can be estimated. The efficiency is defined as $\eta = 100\% \times \frac{W}{Q}$ where the work done, W , is expressed as $W \approx \frac{1}{2}F(t - d) \approx 2$ aJ. The thermal input, Q , to heat the $l_d = 8$ nm thick shell of water around the ANT above the transition temperature by $\delta T = 2^\circ\text{C}$ is $Q \approx 4\pi R^2 l_d C_f \delta T \approx 1$ fJ. Therefore, the efficiency of this nano-oscillator is on the order of $\eta \approx 0.1\%$. These force and efficiency estimates for the ANTs are already impressive without optimisation. They demonstrate that the particles could be used to separate nano-objects that would normally be fixed together due to strong van der Waals or ionic interactions.

5.6 Dynamics of Polymer Nano-shells

The ability to optically characterise the behaviour of stimuli-responsive nano-coatings with the NPoM geometry can be used to study the dynamics of other polymers. For instance, the switching of electrically-modulated polymers is observed, which could be applied in plasmonic sensing devices and tunable colour displays [108, 109]. The tunable plasmon resonance of NPoM structures is demonstrated with the electrochemical and electrical switching by replacing the PNIPAM shell of ANTs with polyaniline (PANI) and polystyrenesulphonate (PSS) (Figure 5.10).

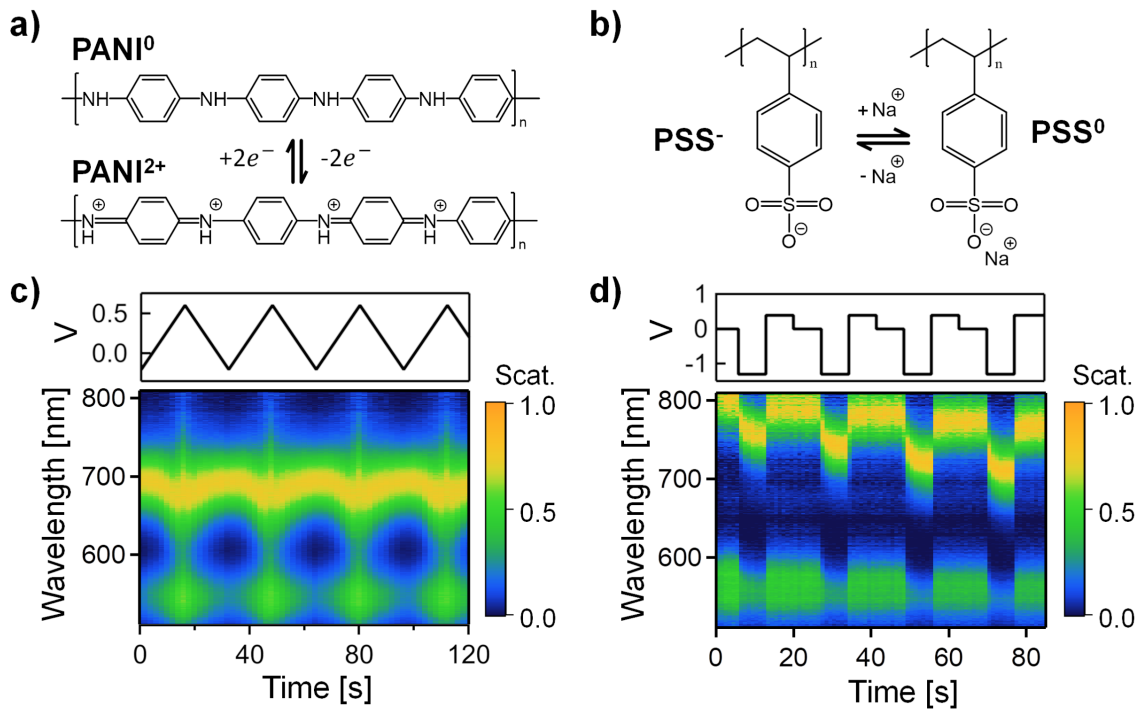


Fig. 5.10 Dynamic NPoMs with different stimuli-responsive polymer nano-shells. a) Polyaniline (PANI) chemical structure change with an electrochemical redox reaction. b) Polystyrenesulphonate (PSS) chemical structure with and without sodium ion association. c) Switching of the NPoM with a 20 nm thick PANI coating via electrochemical cell biasing.¹ d) Switching of a NPoM structure prepared with a thin PSS shell around the nanoparticle. The shell is switched with an applied bias, V , on the gold mirror.

Large changes in refractive index for the PANI coated NPoM structure in response to electrochemical potential reversibly tune the plasmon modes, as demonstrated by Peng et al. (Figure 5.10c) [110]. Similarly, electrically biasing the gold substrate tunes the coupled plasmon mode of polyelectrolyte-coated NPoM structures. In this case, the large plasmon shifts are observed due to the swelling and de-swelling of the PSS shell by moving the counter ions in the bulk solution with the applied electric field [111]. Further work on integrating active polymers with the NPoM geometry could lead to the discovery of more efficient nano-actuating systems.

¹The data for the PANI NPoM scattered intensity plot was acquired by Jialong Peng and Dr. Hyeon-Ho Jeong, Department of Physics, University of Cambridge

5.7 Conclusion and Outlook

In conclusion, the temperature and light-induced response of individual ANTs are revealed using the Nanoparticle on Mirror plasmonic structure. The measured dark-field scattering spectra of 80 nm ANTs are compared to FDTD calculations to precisely measure the gap size between the particle and the mirror. This gap is set by the PNIPAM shell thickness that can expand and contract with cycling temperature. The change in gap size is monitored in real-time with the coupled mode of the NPoM structure. The stroke lengths of the individual particles are found to be ≈ 8 nm, with sub-ms switching times. The force of expansion of the PNIPAM shell is observed to be > 0.3 nN giving an actuating efficiency of $\approx 0.1\%$. This demonstrates that ANTs can overcome the strong van der Waals forces at nm separations and thus, they are promising candidates for powering nanomachines. Lastly, the ability of the NPoM system to track the dynamics of colloid shells demonstrates a useful method for studying other active polymer chain dynamics, which could lead to the development of more efficient nano-actuators.



6. Dynamic ANT Films

This chapter presents the dynamic properties of dense ANT thin-films. These plasmonic films exhibit unusual optical behaviours arising from a combination of the macroscale effective medium response and microscopic interactions of the gold nanoparticles. They are observed to undergo a reversible metal-insulator transition and a semi-fluid to semi-solid transition by direct- and light-induced heating. Furthermore, self-healing properties and 2D gold microstructure printing are studied in this system. These films can be used for different applications such as sensing, imaging optics, displays and dynamic metamaterials or metasurfaces.

6.1 ANT Film Preparation

ANT particle films are prepared by drop-casting or spinning dense ANTs onto flat substrates. The preparation of dense ANT solutions with amine-terminated PNIPAM is described Section 3.1. The films are prepared with small 14 and 16 nm particles because they are easier to synthesise in large quantities and empirically form films with lower roughness. They consist of gold particles embedded in a non-crosslinked PNIPAM medium where the voids between ANT particles are filled with excess PNIPAM.

Initially, dense ANTs are drop-cast and dried on a silicon wafer and examined with reflection spectroscopy, as shown in Figure 6.1. Interestingly, the observed reflectivity is very different compared to PNIPAM and the extinction spectra of the nanoparticles.

Dispersing highly absorbing colloids, such as ANTs, in a transparent dielectric medium normally creates a highly absorbing medium, however here a reflective surface emerges. In fact, the spectrum and high reflectivity (≈ 0.2) more closely resemble a mixture of the spectra from a PNIPAM film and that of a gold mirror. Based on the structure of the film, this coloured reflection must arise from the interface between air and a metamaterial formed of randomly dispersed plasmonic particles interacting on a scale much smaller than the wavelength of visible light.

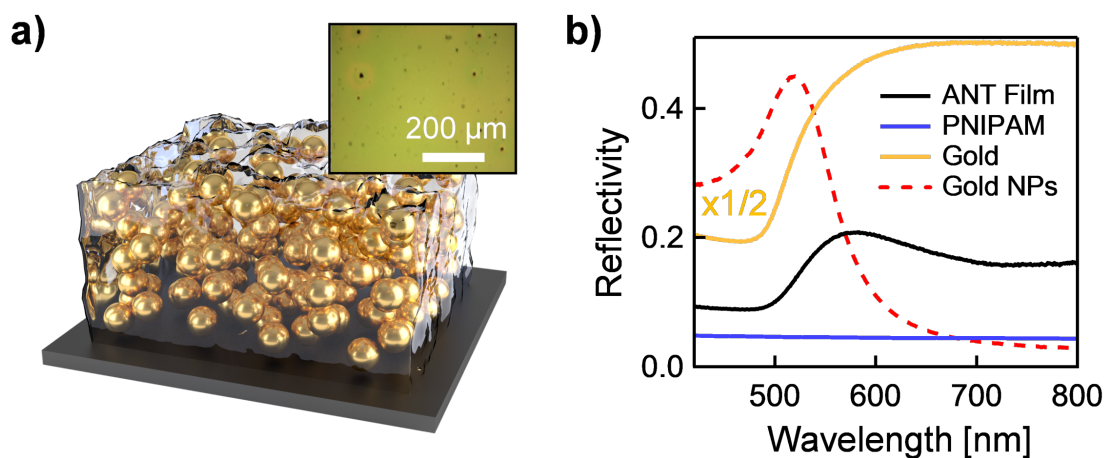


Fig. 6.1 Dense 16 nm ANT particle film dried on a silicon substrate. a) Schematic of ANT films on silicon with nanoparticles embedded in PNIPAM matrix. The inset is a BF microscope image of the film. b) Reflection spectra of the ANT films compared to gold and PNIPAM films as well as the extinction spectra of a 16 nm gold nanoparticle suspension.

6.2 ANT Film Structure

The thickness and distribution of ANTs inside the films drastically affect the optical properties of the films. In order to resolve the thickness and particle distribution, the dried structure of the ANT films is characterised with electron microscopy (FEI Helios NanoLab) and correlated optical microscope imaging in Figure 6.2. The film shown in this figure was prepared with triple the amount PNIPAM to reduce the nanoparticle volume fraction and improve film homogeneity. Focused ion beam (FIB) milling is used to mill wedge structures in the films for cross-sectional electron imaging. Prior to imaging, the films are coated with 200 nm of gold by e-beam evaporation, followed by 80 nm of platinum by ion-beam-induced gas deposition. The gold layer serves to reduce charging during imaging and the platinum improves the perpendicularity of the milled cross-section.

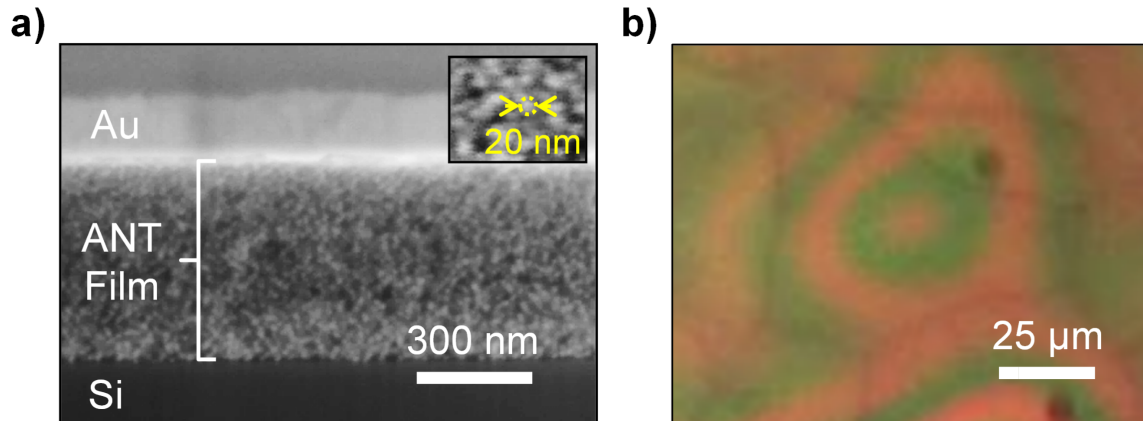


Fig. 6.2 Images of ANT films dried on silicon. a) Focused ion beam (FIB) cross-section image of a 600 nm thick ANT film and b) BF image in reflection. For the FIB imaging the films are coated with a 200 nm layer of gold by e-beam evaporation and 80 nm of platinum by ion-beam-induced gas deposition to mitigate charging effects.

The FIB cross-section images reveal that the gold particles are randomly dispersed in the film (Figure 6.2a). In addition, it is observed that reducing the film thickness as well as the gold volume fraction allows incident light to pass through the film and reflect back from the silicon substrate. Reflected light from the air-film and film-silicon interfaces give rise to thin-film interference effects which form rings on the films in Figure 6.2b. This optical behaviour implies that light can pass through the films even though they are composed of highly absorbing particles. This property can be used to optically probe the composition and thickness of the film using an effective medium approximation.

6.3 Modelling Optical Properties

6.3.1 Effective Medium Approximation

Since the ANT particles and their separations are much smaller than the wavelength of light, the impinging photons do not interact with the particles and continuous PNIPAM medium discretely. The photons interact with an effective medium based the local distribution of the gold nanoparticles. Under the assumption that the particles are spatially uniform and isotropic on average, the films can be modelled with an effective medium approximation [112, 113]. The optical constants of the constituents

in a heterogeneous medium are essentially mixed to form effective parameters related to the relative volume fractions, Φ , as illustrated in Figure 6.3. This approximation greatly simplifies calculations as the effects of individual interstitial particle interactions are disregarded and only averaged interaction effects are considered.

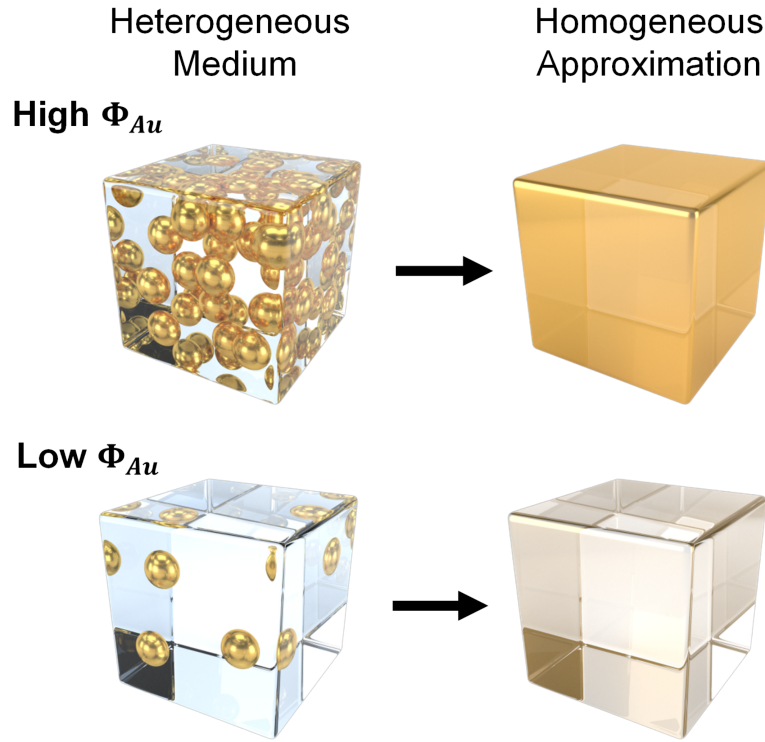


Fig. 6.3 Schematic of the effective medium approximation of gold nanoparticles in a dielectric matrix with high and low gold volume fraction, Φ_{Au} .

Effective medium approximations have been extensively studied and there have been many successful methods, such as Bruggeman, Maxwell-Garnett, Drude, and Lorentz-Lorenz models [114–117]. Here it is found that the Maxwell-Garnett (MG) approximation provides the best fit to observed results. This is not surprising as the MG method is derived specifically for spherical interstitial colloids randomly distributed in a continuous medium [112, 118]. In this approximation, the effective permittivity of the film, ε_{eff} , is determined by the permittivity of the film matrix, ε_m , the interstitial particles, ε_i , and relative volume fraction, Φ_i , of the particles in the film,

$$\varepsilon_{\text{eff}} = \varepsilon_m \frac{2\varepsilon_m + \varepsilon_i + 2\Phi_i(\varepsilon_i - \varepsilon_m)}{2\varepsilon_m + \varepsilon_i + \Phi_i(\varepsilon_m - \varepsilon_i)}. \quad (6.1)$$

The effective permittivity relates to the effective refractive index with $n_{\text{eff}} = \sqrt{\varepsilon_{\text{eff}}}$. The real and imaginary parts of the effective medium are shown in Figure 6.4, where the complex refractive index defined as $\tilde{n} \equiv n - ik$ and $\varepsilon \equiv \varepsilon' + i\varepsilon''$ for the the complex permittivity. Although the MG model appropriately converges to the ε_m of PNIPAM at $\Phi_{Au} = 0$ and ε_{Au} at $\Phi_{Au} = 1$, the maximum expected volume fraction Φ for spherical interstitial particles is $\Phi_{Au} \approx 0.74$ for crystalline close-packed spheres and $\Phi_{Au} \approx 0.64$ for random close-packed spheres [119].

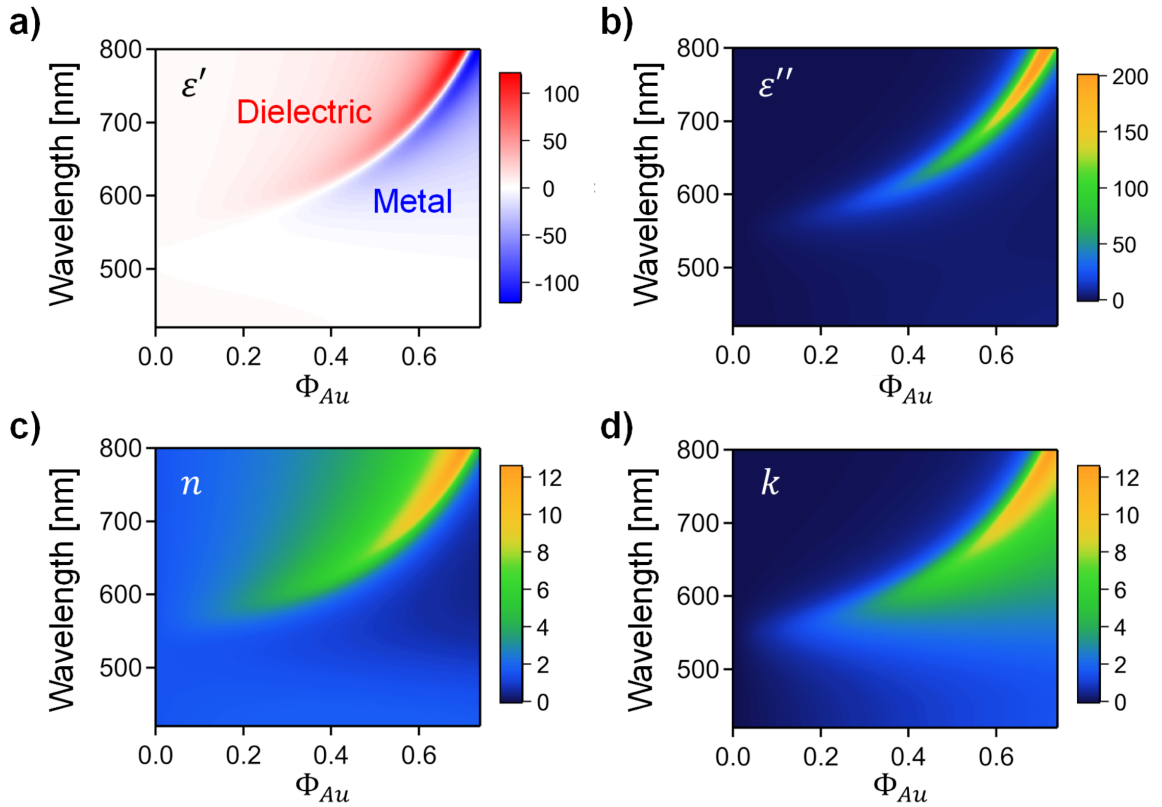


Fig. 6.4 Effective medium approximation of optical constants for different gold volume fractions, Φ_{Au} . a) Real and b) imaginary parts of the effective dielectric constant. c) Real and d) imaginary parts of the effective refractive index.

The MG model predicts the optical constants for the ANT films with any nanoparticle volume fraction. It shows a strong changes in optical properties with Φ_{Au} as expected. The real part of the dielectric constant ε' notably changes from positive to negative with increasing gold concentration for wavelengths above ≈ 520 nm. This marks the insulator-metal transition for the films, where they switch from behaving like insulators that resist electric field flux to conductors that compensate changes in electric field with de-localised electrons. In addition, the redshifting of both the

dielectric constant and refractive index reflects the observed plasmonic shift when gold nanoparticles are brought into close proximity.

6.3.2 Thin-film Interference

Now the reflected spectra from ANT films can be calculated using Fresnel coefficients with the effective refractive index from the MG model. The calculations begin with the generic form of the Fresnel equations for the interface between two mediums defined by refractive indices n_i and n_{i+1} , where light is incident from the n_i side with an angle θ_i . The reflection and transmission coefficients for both s - and p -polarisations are [120]

$$r_{i,i+1}^{(p)} = \frac{n_{i+1} \cos \theta_i - n_i \cos \theta_{i+1}}{n_i \cos \theta_{i+1} + n_{i+1} \cos \theta_i}, \quad (6.2)$$

$$r_{i,i+1}^{(s)} = \frac{n_i \cos \theta_i - n_{i+1} \cos \theta_{i+1}}{n_i \cos \theta_i + n_{i+1} \cos \theta_{i+1}}; \quad (6.3)$$

and

$$t_{i,i+1}^{(p)} = \frac{2n_i \cos \theta_i}{n_i \cos \theta_{i+1} + n_{i+1} \cos \theta_i}, \quad (6.4)$$

$$t_{i,i+1}^{(s)} = \frac{2n_i \cos \theta_i}{n_i \cos \theta_i + n_{i+1} \cos \theta_{i+1}}, \quad (6.5)$$

where the refracted angle, θ_{i+1} , is correspondingly found from $n_i \sin \theta_i = n_{i+1} \sin \theta_{i+1}$. These coefficients define the light interactions at a single interface. The reflectance and transmittance of the interface are expressed as $R^{(p,s)} = \left(r^{(p,s)}\right)^2$ and $T^{(p,s)} = \frac{n_{i+2} \cos \theta_{i+2}}{n_i \cos \theta_i} \left(t^{(p,s)}\right)^2$, respectively. For the case of multiple interfaces, the light transmitted and reflected from the interfaces can interfere. Constructive interference occurs when the light reflected from different interfaces is in phase, whereas destructive interference occurs when it is out of phase. The phase, ϕ , evolves periodically as a function of the optical path length, where $\phi = \frac{2\pi}{\lambda} n_{i+1} d \cos \theta_{i+1}$. The interference of light from multiple interfaces results in effective Fresnel coefficients [121, 122]. For the case of a thin-film with a refractive index of n_1 on a substrate with n_2 , the effective coefficients are

$$r_{eff}^{(p,s)} = \frac{r_{0,1}^{(p,s)} + r_{1,2}^{(p,s)} e^{-2i\phi}}{1 + r_{0,1}^{(p,s)} r_{1,2}^{(p,s)} e^{-2i\phi}}, \quad (6.6)$$

and

$$t_{eff}^{(p,s)} = \frac{t_{0,1}^{(p,s)} t_{1,2}^{(p,s)} e^{-2i\phi}}{1 + t_{0,1}^{(p,s)} t_{1,2}^{(p,s)} e^{-2i\phi}}. \quad (6.7)$$

From these equations, the effective reflectance and transmittance of the film are expressed as

$$R^{(p,s)} = \left(r_{eff}^{(p,s)}\right)^2, \quad (6.8)$$

and

$$T^{(p,s)} = \frac{n_{i+2} \cos \theta_{i+2}}{n_i \cos \theta_i} \left(t_{eff}^{(p,s)}\right)^2. \quad (6.9)$$

Since the light transmitted through the ANT film, T , and into the silicon substrate is quickly absorbed, it can be neglected. Whereas, the reflectance, R , determines the colour of the films.

Combining both the MG effective medium approximation and the thin-film calculations provides accurate fits to the ANT thin-films, as shown in Figure 6.5. Spectral line scans across the film show periodic microcavity modes from the interference of light reflected from the top and bottom interfaces. In order to fit these interference modes, the gold volume fraction must be known. It can be inferred by fitting the position of the constant reflection band around 570 nm, where strong absorption and scattering prevent thin-film interference effects. Both the position and width of the reflection band depends on the gold fraction, giving $\Phi_{Au} = 3.5\%$.

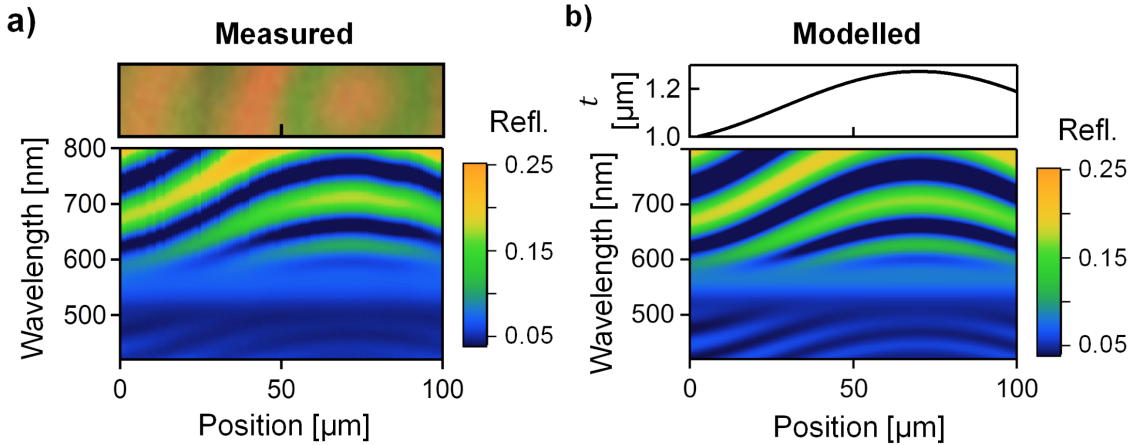


Fig. 6.5 Fitting of the reflected spectra of dried ANT thin-films with an effective medium approximation model. a) Measured ANT thin-film spectra line scan and b) fitted effective medium approximation with a volume fraction $\Phi_{Au} = 3.5\%$ and varying thickness, t .

The thickness of this ANT film sample is accurately fitted with this model as the sample region varies in thickness with $t \approx 1.0 \pm 0.5 \mu\text{m}$ determined by SEM. Furthermore, the agreement of the MG model fit with the ANT films is very helpful

for approximating the separation of the nanoparticles. The fitted particle volume fraction, Φ_{Au} , implies a mean spacing between the particle surfaces of $\langle d \rangle \approx 2R \left[\left(\frac{\sqrt{2}\pi}{6\Phi_{Au}} \right)^{1/3} - 1 \right] \approx 28$ nm. Therefore, the MG model allows for the determination of the composition of ANT films based on their optical properties.

6.4 ANT Film Switching

6.4.1 Bulk Heating

The dynamic properties of ANT films are studied on porous aluminium oxide substrates rather than silicon. As demonstrated in previous chapters, the ANT systems rely on an aqueous environment for their dynamic temperature responses. Unfortunately, adding water to the dried ANT films on silicon rapidly destroys the films by dissolution. This problem could be mitigated by crosslinking the film, however this is challenging because of the high interstitial particle density in the films. In addition, crosslinking reduces the transition rate of PNIPAM [123, 124]. Hence, an alternative solution is used. The films are deposited on aluminium oxide membranes with 20 nm pores. The properties of these membranes are described in more detail in Section 3.2. They are water permeable but remain impermeable to the nanoparticles allowing water to wick in and out of the film when they are placed over a water reservoir, as shown in Figure 6.6. Unlike samples deposited on silicon, thin-film interference is not observed for these films as the underlying aluminium oxide membrane is rough and optically diffusive.

Below the critical temperature $T_c = 32^\circ\text{C}$, the films draw water through the membrane and swell. Whereas, above T_c , the films expel the water back through the membrane and de-swell due to the phase transition of the PNIPAM. This swelling and de-swelling induces a strong optical response. The colour changes from green, in the cold state, to bright-yellow when heated. This dynamic response is driven by the change in the separation of the plasmonic particles in the film, and likewise, the gold volume fraction.

Upon heating above T_c , the peak reflectivity redshifts from ≈ 570 to 600 nm and the reflectivity doubles as shown in Figure 6.6b. This transition is completely reversible over > 1000 cycles with fast modulated light-induced heating. However, only 3 cycles are shown in Figure 6.6c, where the temperature is controlled with a heating stage, because the bulk heating and cooling are slow (≈ 20 minutes).

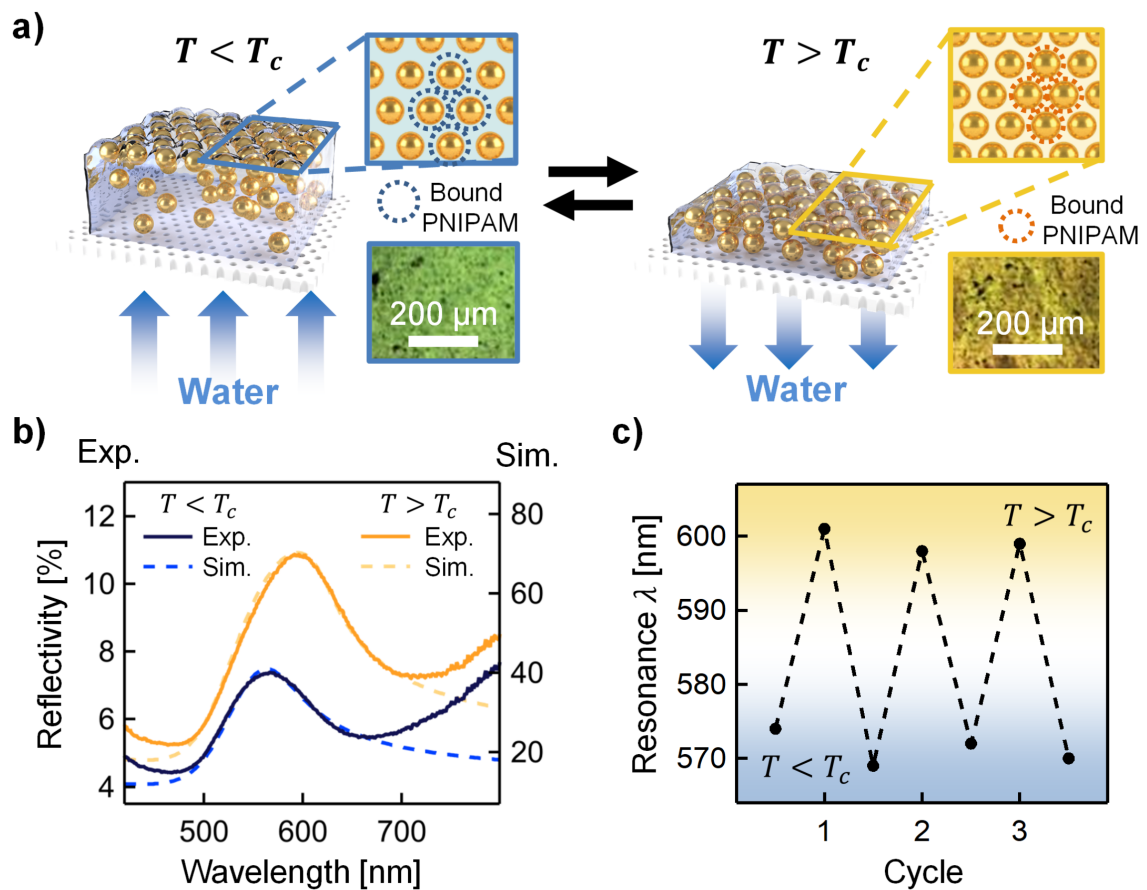


Fig. 6.6 Temperature response of ANT Film on anodised aluminium (Al_2O_3) membranes when heated to 40°C and cooled to 25°C , where is $T_c = 32^\circ\text{C}$. a) Schematic ANT films exchanging water between the film and the reservoir below with temperature. Top-right insets highlight the changing spacing between the ANT particles adsorbed to the surface of the film. Bottom-right insets display BF reflection microscopy images of the film. b) Reflectance spectra of the films above and below T_c along with the reflectance of the fitted MG effective medium model. c) Plasmon resonance wavelength over several temperature cycles.

Similar to the films dried on silicon, the optical properties of the films on anodised aluminium can be extracted by fitting the MG model and reflectance calculations at the air-film interface. The peak positions and shapes agree well in Figure 6.6b, but do not capture the tails of increased reflectance attributed to additional scattering from the porous aluminium oxide membrane. The model implies that the volume fraction of gold is significantly higher when the film is wet, although the peak reflected intensity is smaller than expected from the model. This discrepancy is likely due to diffusive scattering losses from the rough substrate. The inferred gold volume fractions are $\approx 35\%$ for the swollen state and $\approx 50\%$ for the collapsed state, suggesting mean particles separations of 4.5 nm and 2.2 nm. Accounting for these results suggests that a very dense, nearly close-packed layer of ANTs accumulate at the air-film interface and dominate the reflectance of the wetted films. This agrees well with previous studies of core-shell gold nanoparticle monolayers assembled at liquid-liquid and liquid-air interfaces [125–128].

The MG model allows for further analysis of the films optical properties as shown in Figure 6.7. The complex refractive index, $\tilde{n} = n + ik$, and permittivity, $\varepsilon = \varepsilon' + i\varepsilon''$, of the switchable films are extracted in the swollen (cold) and contracted (hot) states. Both real and imaginary parts of the refractive index roughly double, with peak $n > 6$ in the hot collapsed state.

In addition, for the changes in volume fraction observed, a significant change in the real part of the permittivity occurs at $\lambda = 600$ nm. The permittivity switches from positive to negative indicating a insulator-metal transition. This implies that at this optical frequency the electrons on the surface of the film behave as if they are de-localised across the close-packed ANT particles. However, it is noted that at the high volume fractions in this top layer, the MG formalism is less reliable, but analytic models are not yet available for such random organisation of interacting plasmonic particles.

6.4.2 Light-induced Heating

The colour change in response to bulk heating is relatively slow due to the time required to heat and passively cool the water reservoir below the film. The switching speed is greatly improved with plasmonic heating since only small volumes change temperature. Modulating irradiation at 447 nm causes the film to rapidly collapse and

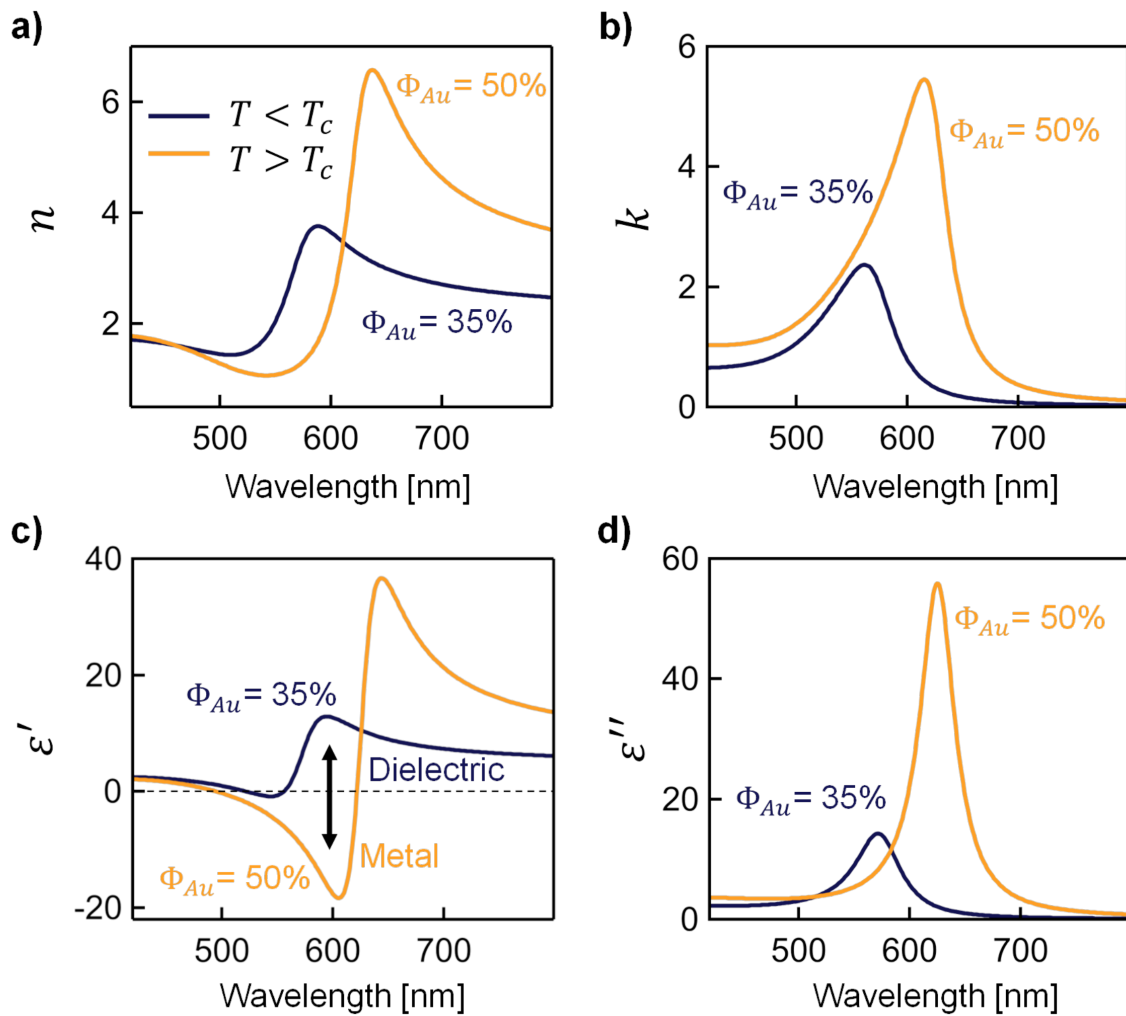


Fig. 6.7 Fitted refractive index and dielectric constants for the surface of hydrated ANT films in response to temperature where $T_c = 32^\circ\text{C}$. a) Real and b) imaginary parts of the refractive index in the cold and hot states. c) Real and d) imaginary parts of the effective dielectric constant in the cold and hot states.

swell. Conceptually it acts as a light-driven water pump, expelling the water upon heating above T_c and absorbing the water again once it cools with the irradiation off.

The transition area of the film clearly depends on laser power, as shown in Figure 6.8. Due to the large absorption cross-section of these dense nanoparticle films, low powers can induce the film transition. Switching is observed at powers below $2 \times 10^3 \text{ W cm}^{-2}$ (Figure 6.8a) when the film is biased at a temperature of 29°C . Also, as in the case of bulk heating, the switching of the films is completely reversible (Figure 6.8b). As the power is increased, the diameter of the transitioned area increases linearly for the examined range $P_{\text{th}} < P < 2.5 \text{ mW}$, where the beam spot is $5 \mu\text{m}$. The power threshold, P_{th} , depends on the initial biasing temperature, T_{bias} , as depicted in Figure 6.8c. The transitioned area discretely marks the region where $T > T_c$. The high contrast and sharpness of transitioned region is a testament to the sharp transition of the ANT particles.

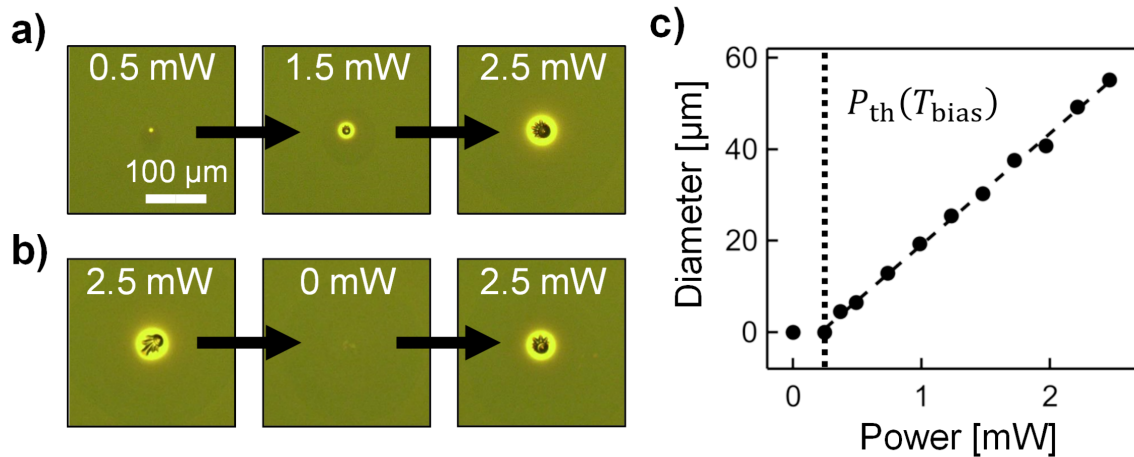


Fig. 6.8 Local heating of 14 nm ANT films with focused light at 447 nm. a) Images of ANT films during a power sweep from 0 mW to 2.5 mW and b) laser cycling on and off at 2.5 mW. c) The corresponding transitioned area diameters, where $T > T_c$, for given powers. The images are acquired through a 500 nm long-pass filter to remove the saturating laser scatter. The pump laser is focused to a $5 \mu\text{m}$ spot.

In the centre of the irradiated region, asymmetric features appear. These features are caused by the kinetics of the capillary-assisted assembly of the ANT particles in the transitioned area. It is important to note that the hydrated ANT films (i.e. in the cold state) are a semi-fluid and whereas in hot state the films are a semi-solid. Initially, upon irradiation, the ANTs in the beam path rapidly expel the local water and aggregate forming semi-solid arbitrary structures. Changes in the absorption

cross-section and the thermal conductivity of these structures help dissipate heat into the surrounding film. This effectively grows the transitioned area as ANTs near the irradiation spot are heated above the T_c and aggregate onto the initial asymmetric semi-solid structure. The shape is affected by capillary and jamming effects between the semi-fluid cold ANTs and the semi-solid heated ANTs. This process generates the fingering instabilities at the centre of the irradiated spots, as observed in Figure 6.8.

Light-induced switching occurs locally near the beam spot without heating the entire water reservoir below the sample. This greatly reduces the switching time from minutes to milliseconds when compared to bulk heating. The switching speed is characterised with video analysis from a high speed camera at 8000 fps, as shown in Figure 6.9. Even at this speed, the initial switching speed during heating cannot be resolved because the transition is too fast. However, the slower response of the growing transitioned area around the irradiation spot is captured as well as the cooling rate when the laser is switched off.

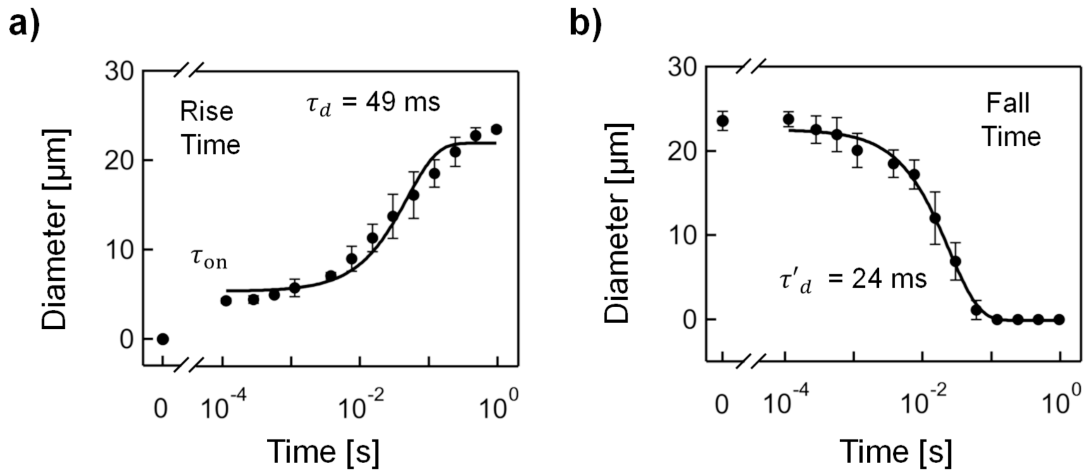


Fig. 6.9 Switching time of ANT films with light-induced heating ($\lambda = 447$ nm, 1 mW). a) Change in the transitioned ANT film area size ($T > T_c$) over time when the laser is switched on, and b) when the laser is switched off. The irradiation spot size is 5 μm . The solid lines are exponential fits with rise and fall times τ_d and τ'_d , respectively.

The initial switching time is less than the video frame rate, hence < 0.1 ms, but it takes ≈ 500 ms to reach the full size of the transitioned area. This is limited by the thermal diffusion from the irradiated spot to the surrounding film. In addition, it is found that the fall time observed in Figure 6.9b is ≈ 24 ms. These switching times are much faster than normally observed for thermoresponsive films. For example, Pong et al. measured de-swelling times of ≈ 3 h for 750 μm thick PNIPAM cross-linked films at

40°C [129]. The fast response of the ANT films is attributed to the lower thickness of the films ($\approx 1 \mu\text{m}$) and the fact that the PNIPAM continuous phase is not cross-linked.

6.5 Self-healing Behaviour

The ANT films also have self healing properties. As briefly mentioned above, they are semi-fluid at temperatures below T_c . This allows for the films to heal minor scuffs when hydrated. This is demonstrated by scoring ANT films in the dried state with a sharp blade and then placing the damaged samples on a water reservoir. As water wicks through the membrane and hydrates the film, the viscous ANTs can flow over surface scratches and restore the film, as shown in Figure 6.10.

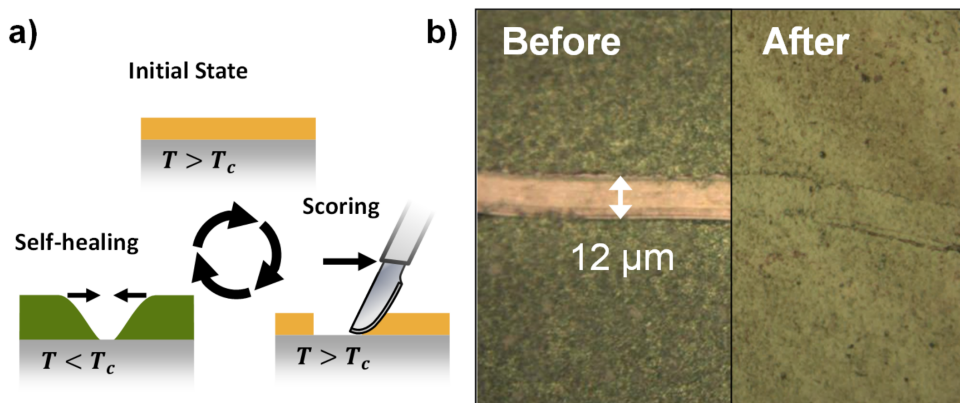


Fig. 6.10 Self-healing of ANT films. a) Schematic of film scratching with a scalpel and restoration from temperature cycling. b) Microscope images of a $12 \mu\text{m}$ scratch before and after wetting the film.

It is observed that scratches up to $12 \mu\text{m}$ can be healed. Larger scratches are more challenging to restore with hydration through the membrane; however, they can be removed by dissolving the ANT film on the substrate and drying the film. This process effectively re-casts the film.

6.6 Printing by Sintering

Another interesting property of the dense ANT films is the ability to sinter the gold nanoparticles with higher irradiation powers. Extensive research has been conducted

on the sintering gold nanoparticles with electron beams and irradiation, because it has the potential to 3D print electrical wires and plasmonic structures [130–133].

In the ANT films, it is shown that the particles can approach one another at short enough distances for the excited gold atoms to diffuse and bridge adjacent gold nanoparticles. This sintering occurs when the interband transitions of the gold nanoparticles are excited with high power irradiation $> 2.5 \times 10^5 \text{ W cm}^{-2}$ at $\lambda = 447 \text{ nm}$. This property can be used to print fixed patterns on the ANT films by raster scanning a focused beam, as demonstrated in Figure 6.11. The minimum printed feature is limited by the diameter of the irradiation spot.

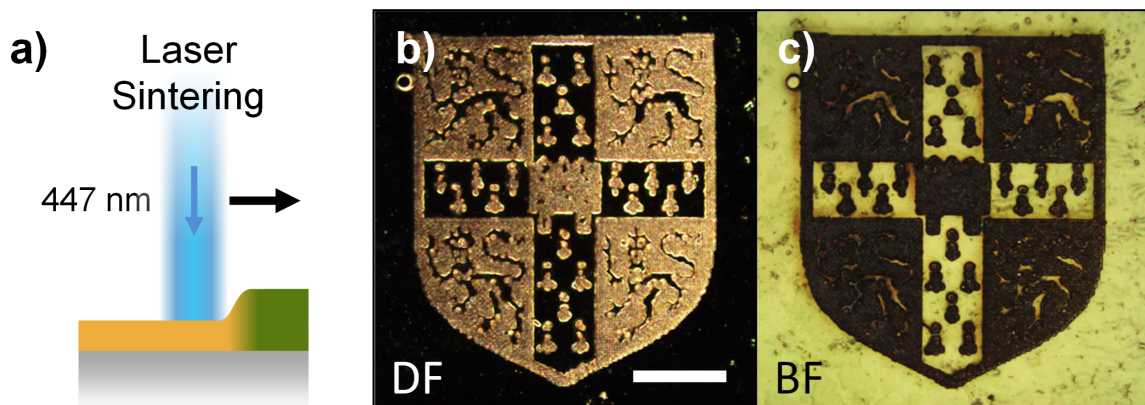


Fig. 6.11 Laser-induced sintering of the ANT film with irradiation at 447 nm and 7.5 mW focused to a 5 μm spot. a) Schematic of the laser sintering process. b) Dark-field (DF) and c) bright-field (BF) microscope images of the sintered Cambridge coat of arms. The circular 5 μm pixels are sintered with 1 s irradiation times. The scale bar is 50 μm .

Planar structures are easily printed by this sintering process, but in principle this technique can produce 3D structures by sequentially casting more ANTs above the printed layer and repeating the laser writing. Furthermore, it is observed that well-interconnected sintered structures can be washed off the substrate for use as standalone gold microstructures.

Although these properties are interesting, they are not specific to ANTs. Gold nanoparticles, and other metal particles, passivated with short thiol-alkanes have previously been shown to exhibit similar sintering behaviour [134]. However, sintering of ANT films could potentially be used to directly pattern permanently conductive areas for the design of dynamic metasurfaces.

6.7 Conclusion

In summary, this chapter demonstrates the ability to tune the optical properties of ANT films with the volume fraction of gold. These properties depend on the complex quasi-random plasmonic interactions of the gold nanoparticles within the film, which can be analytically approximated with the Maxwell-Garnett effective medium theory. ANT films prepared on aluminium oxide membranes can reversibly change the spacing between the interstitial gold nanoparticles from 4.5 nm to 2.2 nm with temperature. This change greatly increases the reflectivity of the films and redshifts the plasmon resonance, as the film undergoes an insulator-to-metal transition. Furthermore, light-induced heating enables the sub-second switching of the film with an initial transition within the irradiation spot that occurs in less than 0.1 ms. The films also show self-healing capabilities due to the semi-fluid behaviour at temperatures below 32°C. Finally, high laser powers are shown to sinter the particles, which enables the patterning of conductive regions that are no longer thermoresponsive. These films demonstrate many interesting behaviours and show high potential for realising fast light-controllable metasurfaces.



7. ANT Microdroplets

In this chapter, the behaviour of ANTs encapsulated in microdroplets is investigated. The confinement of the particles within microscale volumes greatly changes their temperature response as compared the flocculation of ANTs presented in Chapters 2 and 4. The results show interesting biomimetic behaviours where chromatophore-like switching and droplet locomotion are observed.

In nature, motor proteins, such as myosin and kinesin, are used to drive the motion of functional components within cells. For example, pigments and nanocrystals in chromatophores are reversibly moved around the cells to give strong changes in colour and transparency. This is used for active camouflage in many organisms, including cuttlefish, zebrafish, and chameleons [135]. There is substantial interest in mimicking such behaviour, particularly for applications in artificial active camouflage [136–139]. Similarly, there is a push towards developing biomimetic locomotion at the micro- and nanoscale [140–142].

The ANT microdroplets display dynamic colour effects similar to chromatophores in response to bulk temperature changes and local light induced switching. In addition, optically driven locomotion is observed from several mechanisms depending on the irradiation intensity. The droplets demonstrate how nanoscale changes can invoke microscale behaviours, similar to the nanomachines found in nature.

7.1 Artificial Chromatophores

Dense solutions of 14 nm ANT particles are prepared as described in Section 3.1 with amine-terminated PNIPAM. The particles are encapsulated inside $\approx 50 \mu\text{m}$ diameter microdroplets using a PDMS flow-focusing microfluidic device¹. The aqueous ANT phase is formed into water-in-oil microdroplets with a fluorocarbon oil phase (NOVEC 7500 with 0.5 wt% Pico-Surf 1 (Sphere Fluidics)). Once formed, the droplets

¹The microfluidic chip was provided by Wenting Wang, Department of Chemistry, University of Cambridge

are transferred to a sealed optical liquid cell, which allows for further analysis without the evaporation of the droplets and the oil phase.

The formation of the water-in-oil microdroplets is shown in Figure 7.1a. The droplets are generated at a rate of $\approx 1000 \text{ s}^{-1}$ with flow rates of $250 \text{ }\mu\text{L h}^{-1}$ for the aqueous ANT suspension and $500 \text{ }\mu\text{L h}^{-1}$ for the continuous fluorocarbon phase. The droplets are initially $\approx 70 \text{ }\mu\text{m}$ in diameter but overnight they equilibrate to $\approx 50 \text{ }\mu\text{m}$. This is attributed to the dissolution of water inside the fluorocarbon oil phase and results in slightly greater densities of ANT particles within the droplets. From the nanoparticle concentration and the droplet volume, there are $\approx 10^6$ nanoparticles per droplet.

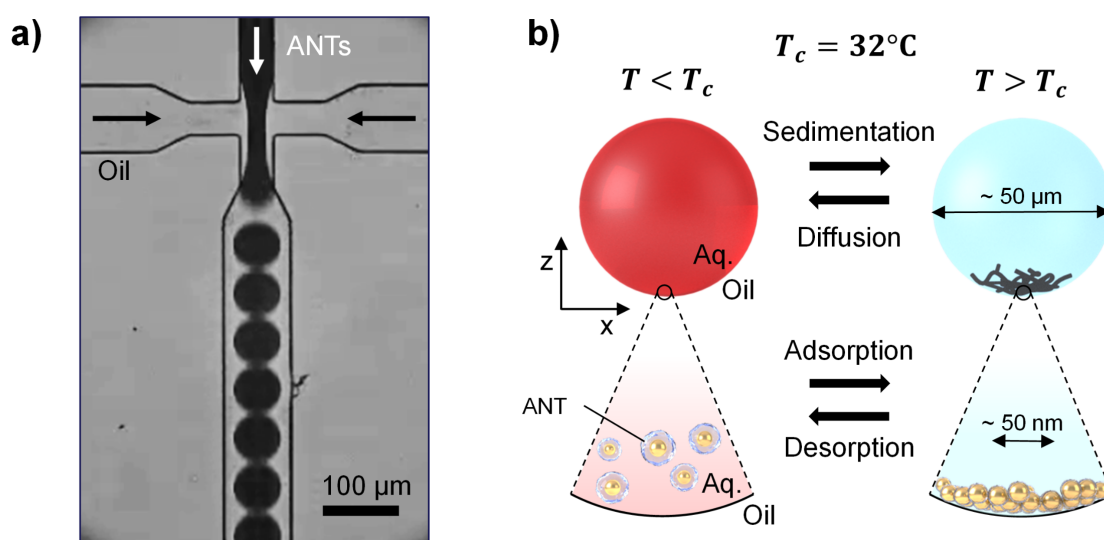


Fig. 7.1 Composition and encapsulation of ANTs in water-in-oil microdroplet chromatophores. a) Microscope transmission image of the formation of the ANT microdroplets with a microfluidic device. b) Schematic of the temperature response of the ANT microdroplets at the microscale and nanoscale.

The ANT microdroplets demonstrate artificial chromatophore-like behaviour where the ANT particles reversibly disperse and localise within the droplets with temperature, as depicted in Figure 7.1b. Below the critical temperature of PNIPAM, $T_c \approx 32^\circ\text{C}$, the ANT particles are uniformly distributed within the droplet. Whereas above T_c , the particles aggregate as previously shown in Chapters 2 and 4. However, here they form a single $\approx 30 \text{ }\mu\text{m}$ -wide aggregates in each microdroplet. Confocal transmission microscopy is used to resolve the position of the aggregates within the droplets, as shown in Figure 7.2. Interestingly, the aggregates are situated at the base of the microdroplets

and the assembled particles resemble two-dimensional (2D) fractal structures with fixed arm widths ($\approx 1 \mu\text{m}$).

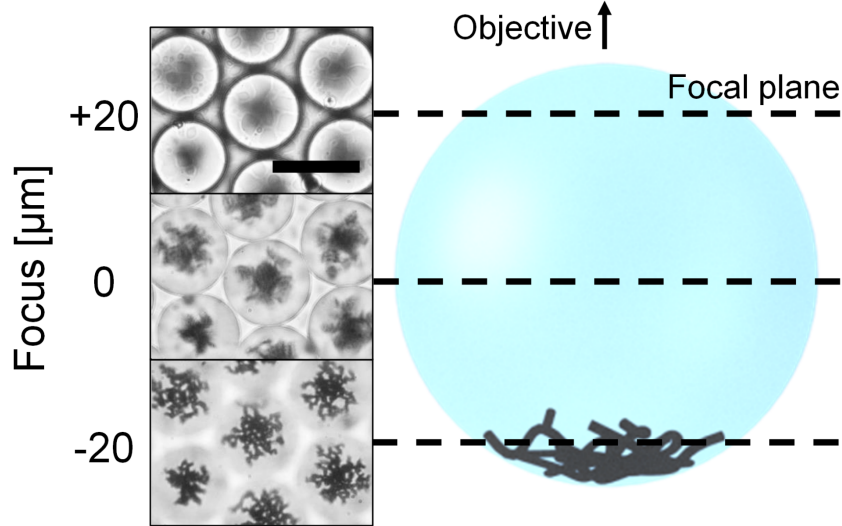


Fig. 7.2 Confocal transmission microscopy images with a 100x objective ($NA = 0.8$) where the focal plane offset by $-20 \mu\text{m}$ (further from objective), $0 \mu\text{m}$, and $+20 \mu\text{m}$ (closer to objective). The scale bar is $50 \mu\text{m}$. A schematic of a heated droplet illustrates the expected position of the focal planes.

The 2D fractal geometry is characteristic of 2D diffusion limited aggregation [143]. This suggests that the ANT particles assemble at the interface of the microdroplets and then sediment to the bottom of the droplets as a result of their larger size and dense gold composition. It is not clear why the fractal branch width is relatively uniform, but it may indicate that there is a critical size limit for the ANT cluster sedimentation along the interface of the microdroplets. Upon cooling the droplets below T_c , the sedimented ANT aggregate quickly re-disperses throughout the droplet with Brownian forces.

7.1.1 Optical Response to Bulk Heating

The optical properties are strongly dependent on the distribution of ANTs within the droplets. The transmission and scattering of the droplets changes drastically with temperature as shown in Figure 7.3. In transmission, the colour changes from red to transparent with a strong broadband absorbing centre. Whereas for dark-field scattering, the colour changes and the brightness is strongly increased in the hot,

aggregated state (Figure 7.3a). This is caused by large changes in scattering cross-section brought on by plasmonic coupling between closely packed gold nanoparticle assemblies. These changes are demonstrated in the spectra Figure 7.3b, taken from a 2 μm collection region at the centre of the droplets. The individual ANT plasmon mode at 526 nm redshifts to aggregate ANT coupled modes in the assembled state [86]. Notably the extinction in the assembled state covers the whole visible spectrum, whereas the dispersed ANT particles absorb predominantly blue and green light. Crucially, this process is fully reversible over repeated heating and cooling cycles.

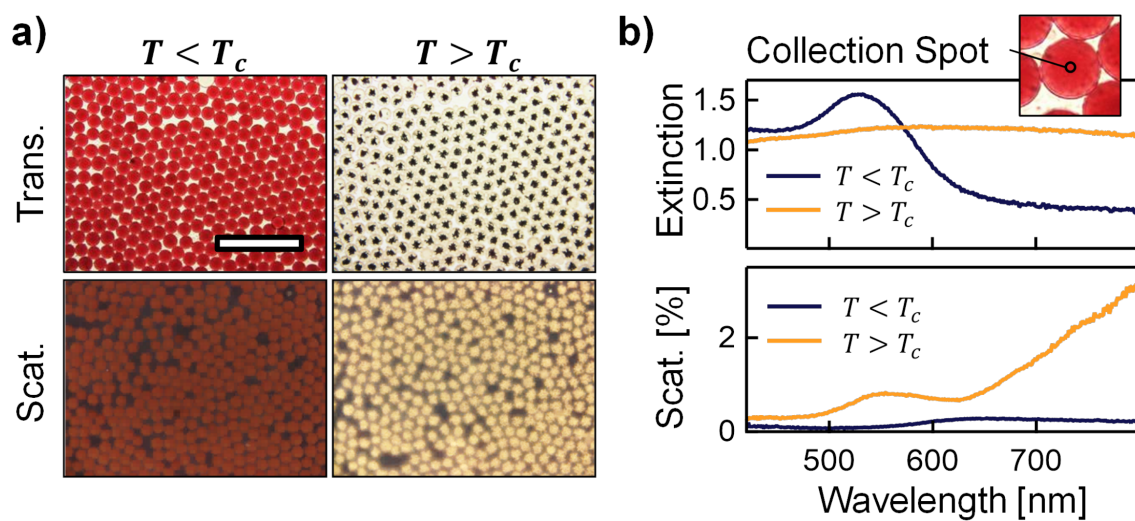


Fig. 7.3 Reversible temperature-induced optical response of the ANT microdroplets. a) Microscope images acquired in bright field transmission mode (top images) and dark field top illumination mode (bottom images) at temperatures below and above the critical temperature ($T_c = 32^\circ\text{C}$). The scale bar is 200 μm . b) Extinction and scattering spectra below ($T = 25^\circ\text{C}$) and above ($T = 40^\circ\text{C}$) the critical temperature acquired from a 2 μm spot in the centre of the droplets, as highlighted in the top-right inset.¹

The strong absorption of dispersed ANT particles in the green spectral region ($\lambda \approx 510 \text{ nm}$) can be used to gate the transmission of green light through the microdroplets, as demonstrated in Figure 7.4. The zoomed insets reveal the stark difference in green light transmission through the microdroplets. This is caused by the change in particle distribution within the microdroplets below and above T_c .

¹Microscope images were acquired by Dr. Andrew Salmon, Department of Physics, University of Cambridge

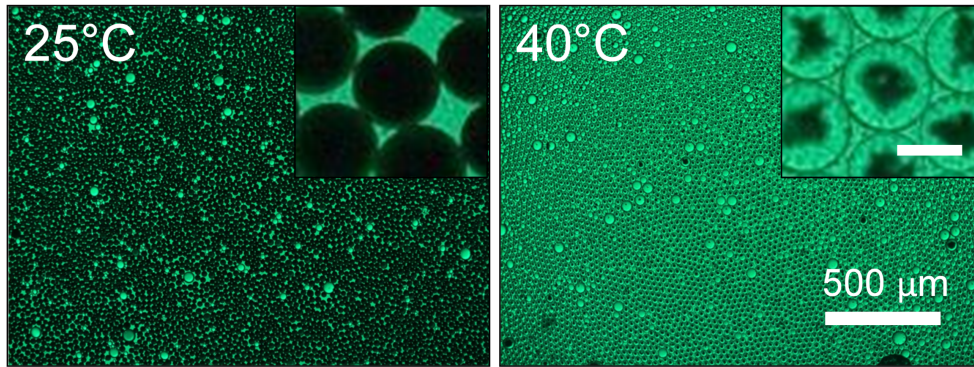


Fig. 7.4 Transmission microscopy images of the ANT microdroplets with green back illumination ($\lambda = 515\text{-}535\text{ nm}$) at 25°C and 40°C . Scale bar is $25\text{ }\mu\text{m}$ for the top right inset.

Multilayers of ANT microdroplets can be packed into large-area sealed cells ($1.5 \times 1.5\text{ cm}$) for macroscale colour change in response to temperature (Figure 7.5). With a white or reflective backing, the transmitted colour changes between the red of the dispersed ANTs and a relatively transparent grey.

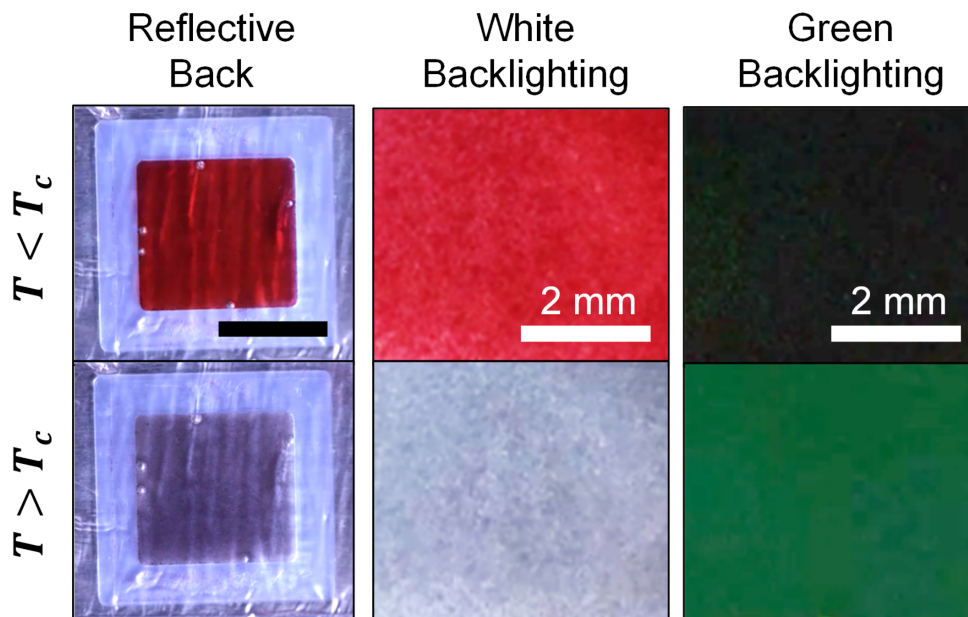


Fig. 7.5 Camera images showing the large area switching of the microdroplet chromatophores with temperature ($T_c = 32^\circ\text{C}$) in various lighting conditions. Top-left scale bar is 1 cm .

The highest transmission contrast is achieved using a green backlight, which is strongly absorbed by the dispersed ANTs. In this case a $\approx 50\%$ increase in green

transmission is observed when $T > T_c$. Using a peltier stage to heat and cool the cells, it is found that the on/off half-cycle switch time is approximately 5 s, which agrees well with the time-scales observed with light-induced switching in the following section. These switching times are longer than what is observed for the ANT films (< 1 s) in Section 6.4.2. This is because the droplet switching times are limited by particle diffusion and the particles are much further separated than in the case of ANT films.

7.1.2 Local Light-induced Heating Effects

The local heating of the artificial chromatophores using laser irradiation at 447 nm is investigated. At this wavelength, the gold interband transitions are strongly absorbing [144]. With the laser spot centred on the droplet, 0.5 mW focused to a 2 μm spot produces observable colour changes on the millisecond timescale (Figure 7.6a). The heat from the illuminated volume conducts throughout the droplet and into the continuous oil phase to neighbouring droplets. Time resolved spectra in Figure 7.6b demonstrate that this is highly reversible over 10 cycles. The short timescales involved in the assembly can be explained by the high particle concentrations. Aggregation of nanoparticles within microdroplets is well described by the diffusion-limited colloidal aggregation model in which the characteristic aggregation timescale is inversely proportional to concentration [145].

The kinetics of the ANT particle aggregation and dis-aggregation are resolved in videos of the transitions, as shown in Figure 7.6c. The initial response of the droplets, when the laser is turned on, is observed after 80 ms, where the droplet becomes darker due to the broadband absorption of the ANT aggregates, which begin to form. Over time, the aggregates grow in size and equilibrate after ≈ 5 s. Unlike the case of bulk heating, strong temperature gradients limit the localisation of the aggregates at the base of the droplet.

The observed cooling kinetics are remarkably fast as the red colour returns within the first 80 ms from shutting off the laser. This rapid response suggests that the microdroplet is rapidly cooled and the remaining 5 s relaxation time is set by the mass transport of the ANT particles to uniformly diffuse throughout the droplet.

The redshifted absorption spectra of the ANT aggregates, in comparison to the dispersed ANTs, suggests that there are different power threshold for instigating the aggregation and dis-aggregation for select wavelengths. This hysteretic behaviour

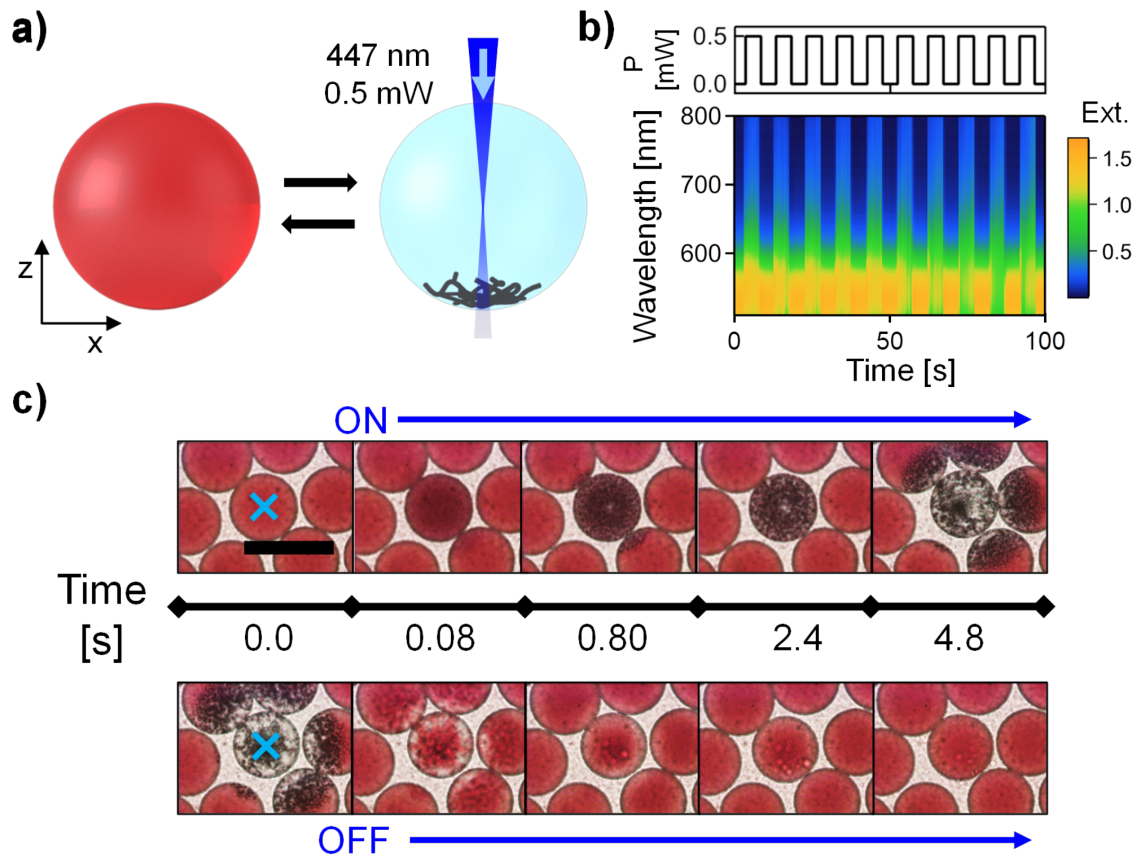


Fig. 7.6 Switching the microdroplet chromatophores with light using a 447 nm beam centered on the microdroplet. The images are acquired through a 500 nm long pass filter to remove the saturating laser scatter. a) Schematic of the light-induced microdroplet switching. b) Time-series extinction spectra map with the irradiation cycled at 100 mHz (50% duty cycle). c) Transmission video frames when switching the laser on and off. The scale bar is 50 μm . The blue crosses mark the 2 μm laser spot positions.

is demonstrated in Figure 7.7 by using 635 nm irradiation and sweeping the power between 0 and 0.3 mW over 3 cycles.

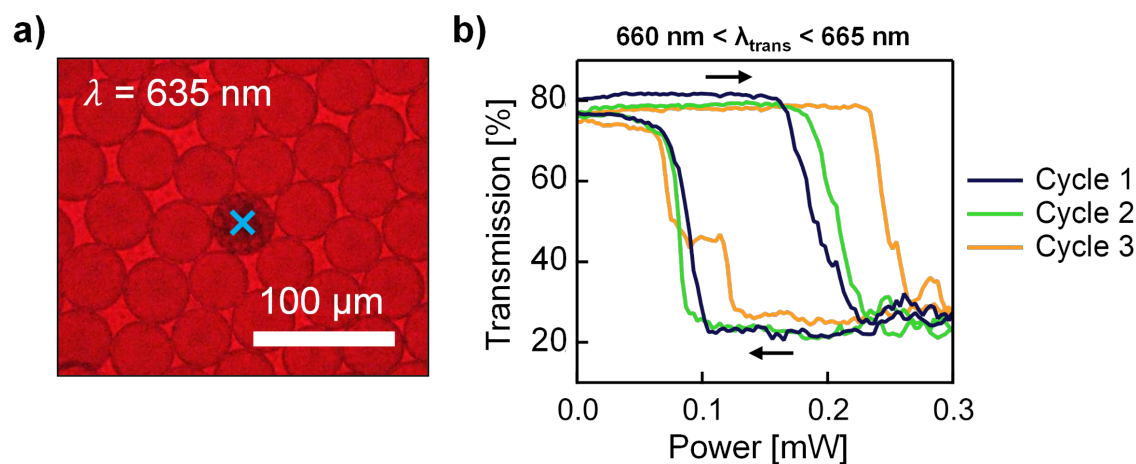


Fig. 7.7 Local microdroplet switching hysteresis with irradiation at $\lambda=635$ nm. a) Transmission microscopy image of microdroplet chromatophores with focused laser irradiation at 0.25 mW at 635 nm. The image is acquired through a 650 nm long pass filter to remove the saturating laser scatter. The blue cross marks the 2 μm laser focus spot. b), Transmission at wavelengths between 660 nm and 665 nm at the centre of an irradiated droplet during 3 cycles of power sweeps from 0 mW to 0.3 mW and back at a rate of 3 $\mu\text{W s}^{-1}$.

The light-induced switching of an individual microdroplet is observed through a 650 nm long pass filter (Figure 7.7a). The power sweep shows that the threshold for heating the ANT particles above T_c and initiating aggregation is approximately 0.2 mW (Figure 7.7b). Above this power the transmission of red light (660 to 665 nm) is greatly diminished from $\approx 80\%$ to $\approx 20\%$. Reducing the power below 0.2 mW does not induce dispersion of the ANTs until the 0.1 mW lower power threshold is reached. This hysteresis is caused by the increased absorption of the ANT aggregates at the excitation wavelength of 635 nm. The behaviour is observed over several cycles, however, the power thresholds are not very consistent. These inconsistencies are attributed to the random variations in cluster formation and flows generated by the temperature gradients in the irradiated microdroplets.

7.2 ANT Microdroplet Swimmers

Off-centre irradiation results in locomotion of the ANT microdroplets as shown in Figure 7.8. Two separate mechanisms are identified for the light-induced microdroplet propulsion. In the first case, the focused irradiation locally heats the ANTs generating a temperature gradient across the droplet. The heated ANTs have increased hydrophobicity which drives them to the water-oil interface. PNIPAM colloids are known to increase the surface tension at the water-oil interface at temperatures just above T_c , due to increased interparticle cohesion [146, 147]. This in effect with the temperature gradient, preferentially increases the surface tension on the irradiated side of the droplet, and causes Marangoni flow at the interface, as shown in Figure 7.8a. The interfacial flow results in a shear force that acts as a “pull stroke”.

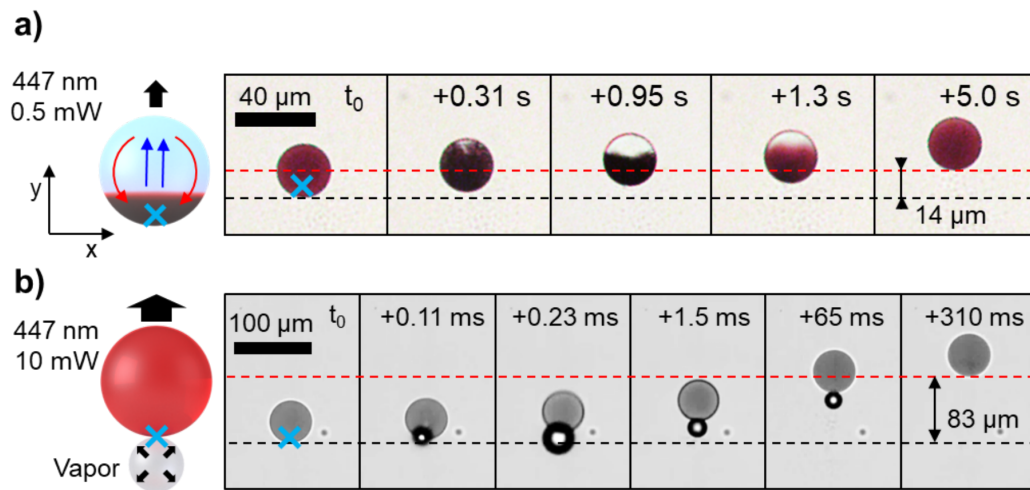


Fig. 7.8 Off-centred irradiation for microdroplet chromatophore locomotion. Two mechanisms are described: thermocapillary force and vapour expansion propulsion. a) Schematic of thermocapillary-induced swimming by off-centred laser-induced heating and time-stamped microscope video frames. b) Schematic of the vapour expansion mechanism for locomotion and time-stamped microscope video frames taken with a high-speed camera. The black and red dashed lines mark the start and stop positions of the microdroplets, respectively. The blue crosses mark the 2 μm laser spot positions.

The condition for locomotion at low Reynold’s number is that the swimming action is non-reciprocal with time [148]. Hence, if the ANTs caused a reciprocal interfacial flow when the droplet moves out of the laser spot, then the net locomotion would be zero. This is not observed as the aggregated ANTs simply desorb from the interface

and disperse inside the droplet to return to their initial internal state. This swimming action can be summarised as a Marangoni pull stroke followed by a diffusive recovery. The swimming of droplets by Marangoni flow (though with a chemical rather than optical fuel) has been well studied previously [149]. This motion is termed squirming, after the similar swimming action used by micro-organisms including paramecium and volvox. The key parameter that determines the locomotion velocity is the capillary number:

$$Ca = \frac{\eta_m V}{\gamma} \approx \frac{2}{5} \frac{\Delta\gamma}{\gamma}, \quad (7.1)$$

where η_m is the viscosity, V is the velocity and γ is the surface tension. Therefore, the velocity is determined by the change in surface tension, $\Delta\gamma$, across the droplet. $\Delta\gamma$ is small relative to γ as the droplets remain spherical, however it is sufficient to move the droplets at microns per second.

The second mechanism for droplet locomotion occurs at relatively high laser powers, as shown in Figure 7.8b. The local high temperatures excited with the 10 mW pump rapidly generate a gas bubble at high pressure. This bubble expands and propels the chromatophore before collapsing reaching maximum speeds of $> 6 \text{ cm s}^{-1}$. In this case the movement is inertial: the bubble expansion and collapse is geometrically reciprocal yet net motion still occurs. The motion is fast enough that, despite the high viscous damping in the fluid, there is still significant displacement. Interestingly, the lack of change in size of the droplets after repeated locomotion suggests that the source of gas for propelling the droplet is dissolved gas inside the oil phase. Furthermore, the formation of condensed water droplets after propulsion is not observed and oil vapour is also ruled out since its boiling point is 128°C , which is greater than that of water.

Therefore, release of gas from the oil is the most likely candidate. Fluorocarbon oils are well known to hold large quantities of dissolved gas [150]. The gas solubility decreases with temperature and thus, bubbles form when the oil is heated. This is also consistent with the observation that in some cases, after formation, the bubbles grow spontaneously. This implies that the bubble is growing in a supersaturated solution.

7.3 Conclusion

Mobile artificial chromatophores were made by densely loading microfluidic microdroplets with ANT particles. The ANT aggregation in the confines of the droplets differs greatly than in bulk, as seen in previous chapters. They reversibly assemble and

disassemble between dispersed and localised configurations upon temperature cycling above and below T_c . This transition produces dynamic colour effects. In the hot state, the light can transmit through the droplets, while in the cold state, light is strongly absorbed. This behaviour mimics the colour changing mechanism of chromatophores seen in nature. This switching is also demonstrated with light control and it is highly reversible. Complete switching times of ≈ 5 s are observed, which are limited by diffusional mass transport of ANTs.

Light-induced droplet locomotion is also presented with two distinct propulsion mechanisms. Droplet squirming is driven by interfacial thermocapillary flows with lower power irradiation, whereas inertial locomotion by rapid gas expansion is observed at higher powers. The ANT droplets showcase how the interaction of millions of artificial nano-actuators can drive larger, microscale physical changes.



8. Conclusions and Outlook

The dynamic behaviours of actuating nanotransducers (ANTs) have been investigated in 4 different systems in this work. The integration of ANTs in aqueous suspensions, nanoparticle on mirror structures (NPOMs), films, and microdroplets has been studied. This final chapter contains a brief summary of the main findings presented for each of these systems. Recommendations for future applications and research areas for ANTs are also discussed, including the development of ANTs with alternative cores, DNA nanomachines, artificial cilia, and dynamic metasurfaces.

8.1 Summary

ANTs are very versatile. They bring about dynamic properties to many, otherwise, static systems. This work examined the behaviours of simple artificial nano-actuators that consist of plasmonic nanoparticles coated with thermoresponsive polymer shells. Here, gold nanoparticle cores with grafted poly(N-isopropylacrylamide) (PNIPAM) shells were studied.

This thesis begins with the fundamentals of light interactions with plasmonic particles. Plasmonic nanoparticles were shown to exhibit optical signatures that are highly sensitive to their environment. Changes in shapes, size, refractive index, and the proximity to other plasmonic surfaces, significantly affect their optical properties. This reaction of plasmonic systems to their local environments enables the inference of their surroundings with spectroscopy. In addition, their large absorption cross-sections effectively convert light to heat in nanoscale volumes. Heat is rapidly generated and dissipated from these small volumes, which allows for fast temperature changes that are sufficient to induce a phase transition in PNIPAM shells.

The robust ability of PNIPAM chains to readily swell and de-swell in response to small temperature changes was demonstrated. This response is characterised by a coil-to-globule transition mediated by intrachain hydrogen bonding that occurs at a critical temperature, T_c , of 32°C. Simultaneously, an increase in interchain cohesion

drives the assembly of colloids at temperatures above T_c . The assembly of these colloids is dictated by intercolloidal interaction potentials described by extended DLVO theory.

The reversible assembly of colloidal ANTs in aqueous media was introduced. In heated ANT suspensions, closely-packed gold particle assemblies enable strong inter-particle plasmonic coupling. This can produce large shifts in plasmonic resonance wavelengths greater than 100 nm. This drastic optical response is triggered with bulk or light-induced heating of the suspension above T_c . Crucially, upon cooling, the initial state of the suspension is fully recovered.

The effects of PNIPAM termination, solution ionic strength, and excess PNIPAM on the reversible assembly of ANT colloids was studied. An analytical model was developed to predict the plasmon shift of the aggregates based on the size and separation of coupled plasmonic particles. It was found that the internal structure and size of the ANT clusters depend greatly on the local charges of the particles within the assemblies. High ionic strengths, and charged PNIPAM terminations help screen the surface charges and enable the particles to approach closer within the clusters as well as increase the overall cluster size. These effects work in conjunction to increase the plasmonic resonance redshift of these assemblies, resulting in the observed drastic changes in the optical properties of ANT suspensions.

The dynamic behaviours of individual ANT particles were characterised in the NPoM plasmonic structure. The NPoM structure enables the simultaneous probing and actuation of ANT particles with light. The mechanical actuation of individual particles was inferred from the dynamic optical signatures of the plasmonic structures. The gold core of an ANT particle plasmonically couples to its image charge in the gold mirror. This generates a coupled mode that is highly sensitive to the spacing between the particle and the mirror. The spacing is defined by the thickness of PNIPAM shell, which expands and contracts in response to temperature, and modulates the coupled mode resonance. The transient shell thickness is optically resolved in real-time with fitted FDTD solutions. The stroke length of individual particles was found to be ≈ 8 nm, with sub-ms switching times. In addition, the force of expansion of the PNIPAM shell is > 0.3 nN, which is more than sufficient to overcome the large van der Waals forces at nanoscale separations. Therefore, it is evident that ANT particles can produce useful mechanical work on the nanoscale.

ANTs were also studied in dense films cast on silicon and porous anodised aluminium. The optical properties of the films are found to depend greatly on the fill fraction of gold nanoparticles. A Maxwell-Garnett effective medium approximation was used to

analytically model the optical constants of these heterogeneous films. On porous media, water is effectively pumped in and out of the film in response to temperature. The swelling and de-swelling of the film is accompanied by significant change in the gold fill fraction and an interesting insulator-metal transition. Furthermore, fast transitions below 0.1 ms were observed with light-induced heating. The films also exhibit self-healing capabilities due to their semi-fluid state at temperatures below 32°C. Finally, high laser powers were shown to sinter the particles, which enables the patterning of permanent conductive regions that no longer switch. There is potential to exploit the dynamic properties of these ANT films for the development of transient light-configured metasurfaces.

The last ANT system studied in this work consisted of microdroplets densely loaded with ANT particles. The ANT assembly within the droplets differs greatly than in bulk due to confinement effects. They reversibly assemble and disassemble between dispersed and localised configurations upon temperature cycling above and below T_c producing dynamic colour. This behaviour mimics the remarkable colour changing mechanism of chromatophores as seen in nature. Furthermore, light-induced droplet locomotion was presented with two distinct propulsion mechanisms. Light-induced interfacial Marangoni flows cause droplet squirring. This is driven by a surface tension gradient across droplet in response to the light-induced temperature gradient. In addition, inertial propulsion by rapid gas expansion was demonstrated with higher irradiation powers. These droplets demonstrate how ANTs can interact with each other to cause microscale effects both in droplet colour dynamics and locomotion.

8.2 Future Directions

The work presented in this thesis describes a significant advance in plasmonic light-driven nano-actuator systems. The remarkable variety of dynamic behaviours presented in ANT systems has inspired several other research topics. Notably the development different types of ANT particles and ANT systems, including DNA nanomachines, artificial cilia, and dynamic metasurfaces.

Although, the ANTs discussed throughout this work consist of gold nanoparticles coated with PNIPAM. In principle, the basic ANT properties are not exclusive to Au@PNIPAM nanoparticles. Alternative plasmonic materials, such as silver, copper, and aluminium or even other highly absorbing materials, such as carbon nanoparticles, could be used depending on application constraints. These proposed materials can

greatly reduce the cost of developing ANT systems. However, the alternative plasmonic materials are plagued by thin innate oxide coatings that complicate the correlation between the dynamic optical signatures and the mechanical responses of ANT systems to light and temperature [151, 152]. For less stringent applications, where optical feedback is not required, even cheaper non-metal particles, such as carbon nanoparticles, can be used as strong absorbers for local heating on the nanoscale. Similarly, the choice of PNIPAM as the shell material is not critical. Other thermoresponsive polymers with convenient LCSTs, or even UCSTs, could be used. Potentially, polymers with different critical temperatures could be selected to satisfy the requirements of specific ANT system applications [69]. Although, different types of ANT particle could demonstrate similar or even improved functionalities compared to the Au@PNIPAM particles, it is important to recall that they will likely behave differently due to differences in the local charges on the ANT cores and the effective charge screening of the suspension, as discussed in Chapter 4.

The ANT systems presented in this work demonstrate that the ANT particles are promising candidates for driving nanomachines. With the recent advances in DNA origami leading to unprecedented control on the nanoscale, dynamic DNA nanomachines could be realised. Recently, dynamic hinges on the scale of ≈ 50 nm have been developed by integrating PNIPAM with DNA origami plates [153]. In addition, another study has shown temperature-induced switching of DNA origami structures with PNIPAM [154]. This suggests that the incorporation of ANT particles in DNA origami structures could enable light-induced switching via plasmonic heating. In such systems, individual DNA nanomachines could be optically addressed. These machines could mimic cellular nanomachines, such as enzymes and ribosomes, to realise artificial ‘DNAzymes’ and nanofactories. The advent of such nanomachines could lead to novel nanodevices and therapeutic treatments.

The nano-actuation of ANTs could also be harnessed for the design of beating and flexing filaments. Again mimicking a natural system, such as the behaviours of cilia and flagella, to develop artificial dynamic filaments could produce a useful nanodevice. Loading elastic fibres or forming bilayer filaments with integrated ANT particles could potentially produce wave-like filament responses to projected light patterns [155]. Similar, magnetically-driven artificial cilia have previously been reported [156–158], however these filaments cannot be controlled individually. Light-driven artificial cilia could have improved functionality as the fibres can be individually addressed with light. These fibres can be used to control fluids or to manipulate adsorbed nano- and microstructures.

Finally, as discussed in Chapter 6, the ANT films undergo a reversible transition from an insulator to metal in response to light-induced heating. This dynamic response could possibly be used to develop fast, reconfigurable metasurfaces that are controlled with projected light patterns. Such films could be used for dynamic cloaking or other 2D metamaterial applications. Furthermore, the local collapse of the ANT film with focused light-induced heating could be used to manipulate surface bound objects, such as colloids or cells. Such films could enable the light-guided 2D assembly of materials, furthering control on both the nano- and microscale.

References

- [1] Richard P. Feynman. There's Plenty of Room at the Bottom. *Caltech Engineering and Science*, 23(5):22–36, 1960.
- [2] Martien A. Cohen Stuart, Wilhelm T. S. Huck, Jan Genzer, Marcus Müller, Christopher Ober, Manfred Stamm, Gleb B. Sukhorukov, Igal Szleifer, Vladimir V. Tsukruk, Marek Urban, Françoise Winnik, Stefan Zauscher, Igor Luzinov, and Sergiy Minko. Emerging applications of stimuli-responsive polymer materials. *Nature materials*, 9(2):101–113, 2010.
- [3] Bruce Alberts, Alexander Johnson, Julian Lewis, Martin Raff, Keith Roberts, and Peter Walter. *Molecular Biology of the Cell*. Garland Science, New York, fourth edition, 2002.
- [4] Stefan A. Maier. *Plasmonics : fundamentals and applications*. Springer US, 2007.
- [5] J. J. Mock, M. Barbic, D. R. Smith, D. A. Schultz, and S. Schultz. Shape effects in plasmon resonance of individual colloidal silver nanoparticles. *The Journal of Chemical Physics*, 116(15):6755–6759, 2002.
- [6] Emilie Ringe, Mark R. Langille, Kwonnam Sohn, Jian Zhang, Jiaying Huang, Chad A. Mirkin, Richard P. Van Duyne, and Laurence D. Marks. Plasmon Length: A Universal Parameter to Describe Size Effects in Gold Nanoparticles. *The Journal of Physical Chemistry Letters*, 3(11):1479–1483, 2012.
- [7] Harald Ibach and Hans Lüth. *Solid-state physics: An introduction to principles of materials science*. Springer, 2009.
- [8] P. B. Johnson and R. W. Christy. Optical Constants of the Noble Metals. *Physical Review B*, 6(12):4370–4379, 1972.
- [9] Neil Bartlett. Relativistic effects and the chemistry of gold. *Gold Bulletin*, 31(1):22–25, 1998.
- [10] Craig F. Bohren and Donald R. Huffman. *Absorption and Scattering of Light by Small Particles*. John Wiley & Sons, Ltd, 1998.
- [11] Viktor Myroshnychenko, Jessica Rodríguez-Fernández, Isabel Pastoriza-Santos, Alison M. Funston, Carolina Novo, Paul Mulvaney, Luis M. Liz-Marzán, and F. Javier García de Abajo. Modelling the optical response of gold nanoparticles. *Chemical Society Reviews*, 37(9):1792, 2008.
- [12] P. Nordlander, C. Oubre, E. Prodan, K. Li, and M. I. Stockman. Plasmon hybridization in nanoparticle dimers. *Nano Letters*, 4(5):899–903, 2004.

-
- [13] D. W. Mackowski and M. I. Mishchenko. A multiple sphere T-matrix Fortran code for use on parallel computer clusters. *Journal of Quantitative Spectroscopy and Radiative Transfer*, 112(13):2182–2192, 2011.
- [14] Alexander O. Govorov, Wei Zhang, Timur Skeini, Hugh Richardson, Jaebeom Lee, and Nicholas A. Kotov. Gold nanoparticle ensembles as heaters and actuators: Melting and collective plasmon resonances. *Nanoscale Research Letters*, 1(1):84–90, 2006.
- [15] Alexander O. Govorov and Hugh H. Richardson. Generating heat with metal nanoparticles. *Nano Today*, 2(1):30–38, 2007.
- [16] Hideyuki Inouye, Koichiro Tanaka, Ichiro Tanahashi, and Kazuyuki Hirao. Ultrafast dynamics of nonequilibrium electrons in a gold nanoparticle system. *Physical Review B*, 57(18):11334–11340, 1998.
- [17] Wenyu Huang, Wei Qian, Mostafa A. El-Sayed, Yong Ding, and Zhong Lin Wang. Effect of the lattice crystallinity on the electron-phonon relaxation rates in gold nanoparticles. *Journal of Physical Chemistry C*, 111(29):10751–10757, 2007.
- [18] Guillaume Baffou and Romain Quidant. Thermo-plasmonics: Using metallic nanostructures as nano-sources of heat. *Laser and Photonics Reviews*, 7(2):171–187, 2013.
- [19] Orla M. Wilson, Xiaoyuan Hu, David G. Cahill, and Paul V Braun. Colloidal metal particles as probes of nanoscale thermal transport in fluids. *Physical Review B - Condensed Matter and Materials Physics*, 66(22):2243011–2243016, 2002.
- [20] Guillaume Baffou, Romain Quidant, and Christian Girard. Thermoplasmonics modeling: A Green’s function approach. *Physical Review B*, 82(16):165424, 2010.
- [21] Harper Meng and Jinlian Hu. A brief review of stimulus-active polymers responsive to thermal, light, magnetic, electric, and water/solvent stimuli. *Journal of Intelligent Material Systems and Structures*, 21(9):859–885, 2010.
- [22] Haruma Kawaguchi. Thermoresponsive microhydrogels: preparation, properties and applications. *Polymer International*, 63(6):925–932, 2014.
- [23] Avraham Halperin, Martin Kröger, and Françoise M. Winnik. Poly(N-isopropylacrylamide) Phase Diagrams: Fifty Years of Research. *Angewandte Chemie International Edition*, 54(51):15342–15367, 2015.
- [24] R. Koningsveld, W. H. Stockmayer, and E Nies. *Polymer Phase Diagrams: A Textbook*. Oxford University Press, 2001.
- [25] Paul J. Flory. Thermodynamics of high polymer solutions. *The Journal of Chemical Physics*, 10(1):51–61, 1942.
- [26] Maurice L. Huggins. Solutions of Long Chain Compounds. *The Journal of Chemical Physics*, 9(5):440, 1941.

- [27] S. Hirotsu. Coexistence of phases and the nature of first-order phase transition in poly-N-isopropylacrylamide gels. In *Responsive Gels: Volume Transitions II*, pages 1–26. Springer-Verlag, 1993.
- [28] Shingjiang Jessie Lue, Chi-Hwa Chen, and Chao-Ming Shih. Tuning of Lower Critical Solution Temperature (LCST) of Poly(N-Isopropylacrylamide-co-Acrylic acid) Hydrogels. *Journal of Macromolecular Science, Part B*, 50(3):563–579, 2011.
- [29] Kamiya Jain, Raman Vedarajan, Masaki Watanabe, Mamoru Ishikiriyama, and Noriyoshi Matsumi. Tunable LCST behavior of poly(N-isopropylacrylamide/ionic liquid) copolymers. *Polymer Chemistry*, 6(38):6819–6825, 2015.
- [30] Yukinori Okada and Fumihiko Tanaka. Cooperative hydration, chain collapse, and flat LCST behavior in aqueous poly(N-isopropylacrylamide) solutions. *Macromolecules*, 38(10):4465–4471, 2005.
- [31] R. Gomes de Azevedo, L. P. N. Rebelo, A. M. Ramos, J. Szydlowski, H. C. de Sousa, and J. Klein. Phase behavior of (polyacrylamides + water) solutions: concentration, pressure and isotope effects. *Fluid Phase Equilibria*, 185(1-2):189–198, 2001.
- [32] M. Heskins and J. E. Guillet. Solution Properties of Poly(N-isopropylacrylamide). *Journal of Macromolecular Science-Chemistry*, 2(8):1441–1455, 1968.
- [33] Chi Wu and Xiaohui Wang. Globule-to-Coil Transition of a Single Homopolymer Chain in Solution. *Physical Review Letters*, 80(18):4092–4094, 1998.
- [34] Matthias Karg, Thomas Hellweg, and Paul Mulvaney. Self-Assembly of Tunable Nanocrystal Superlattices Using Poly-(NIPAM) Spacers. *Advanced Functional Materials*, 21(24):4668–4676, 2011.
- [35] B. Derjaguin and L. Landau. Theory of the stability of strongly charged lyophobic sols and of the adhesion of strongly charged particles in solutions of electrolytes. *Progress in Surface Science*, 43(1-4):30–59, 1993.
- [36] E. J. W. Verwey. Theory of the stability of lyophobic colloids. *The Journal of physical Chemistry*, 51:631–636, 1947.
- [37] Robert J. Hunter. *Foundations of Colloid Science*. Oxford University Press, second edition, 2000.
- [38] Jacob N. Israelachvili. *Intermolecular and surface forces*. Academic Press, 2011.
- [39] Taehoon Kim, Kangtaek Lee, Myoung Seon Gong, and Sang Woo Joo. Control of gold nanoparticle aggregates by manipulation of interparticle interaction. *Langmuir*, 21(21):9524–9528, 2005.
- [40] Alaa H. Jalil and Ute Pyell. Quantification of Zeta-Potential and Electrokinetic Surface Charge Density for Colloidal Silica Nanoparticles Dependent on Type and Concentration of the Counterion: Probing the Outer Helmholtz Plane. *The Journal of Physical Chemistry C*, 122(8):4437–4453, 2018.

- [41] D. Grasso, K. Subramaniam, M. Butkus, K. Strevett, and J. Bergendahl. A review of non-DLVO interactions in environmental colloidal systems. *Reviews in Environmental Science and Biotechnology*, 1(1):17–38, 2002.
- [42] S. H. Behrens, M. Borkovec, and P. Schurtenberger. Aggregation in charge-stabilized colloidal suspensions revisited. *Langmuir*, 14(8):1951–1954, 1998.
- [43] Ihor Tokarev and Sergiy Minko. Tunable plasmonic nanostructures from noble metal nanoparticles and stimuli-responsive polymers. *Soft Matter*, 8(22):5980–5987, 2012.
- [44] Atsushi Shiotani, Takeshi Mori, Takuro Niidome, Yasuro Niidome, and Yoshiki Katayama. Stable incorporation of gold nanorods into N-isopropylacrylamide hydrogels and their rapid shrinkage induced by near-infrared laser irradiation. *Langmuir*, 23(7):4012–4018, 2007.
- [45] Maria Molina, Mazdak Asadian-Birjand, Juan Balach, Julian Bergueiro, Enrico Miceli, and Marcelo Calderón. Stimuli-responsive nanogel composites and their application in nanomedicine. *Chemical Society Reviews*, 44(17):6161–6186, 2015.
- [46] Youwei Zhang, Ming Jiang, Jiongxin Zhao, and Daoyong Chen. Thermo-sensitive core-shell nanoparticles as potential drug carrier. *European Polymer Journal*, 43(12):4905–4915, 2007.
- [47] Ming Qiang Zhu, Li Qiong Wang, Gregory J. Exarhos, and Alexander D. Q. Li. Thermosensitive Gold Nanoparticles. *Journal of the American Chemical Society*, 126(9):2656–2657, 2004.
- [48] Samuel T. Jones, Zarah Walsh-Korb, Steven J. Barrow, Sarah L. Henderson, Jesús Del Barrio, and Oren A. Scherman. The Importance of Excess Poly(N-isopropylacrylamide) for the Aggregation of Poly(N-isopropylacrylamide)-Coated Gold Nanoparticles. *ACS Nano*, 10(3):3158–3165, 2016.
- [49] Tao Ding, Ventsislav K. Valev, Andrew R. Salmon, Chris J. Forman, Stoyan K. Smoukov, Oren A. Scherman, Daan Frenkel, and Jeremy J. Baumberg. Light-induced actuating nanotransducers. *Proceedings of the National Academy of Sciences of the United States of America*, 113(20):5503–7, 2016.
- [50] Nicolas Vogel, Cristina Fernández-López, Jorge Pérez-Juste, Luis M. Liz-Marzán, Katharina Landfester, and Clemens K. Weiss. Ordered Arrays of Gold Nanostructures from Interfacially Assembled Au@PNIPAM Hybrid Nanoparticles. *Langmuir*, 28(24):8985–8993, 2012.
- [51] Fei Han, Alexander H. Soeriyadi, S. R. C. Vivekchand, and J. Justin Gooding. Simple Method for Tuning the Optical Properties of Thermoresponsive Plasmonic Nanogels. *ACS Macro Letters*, 5(5):626–630, 2016.
- [52] Samarendra Maji, Belgin Cesur, Zhiyue Zhang, Bruno G. De Geest, and Richard Hoogenboom. Poly(N-isopropylacrylamide) coated gold nanoparticles as colourimetric temperature and salt sensors. *Polymer Chemistry*, 7(9):1705–1710, 2016.

- [53] Holger Lange, Beatriz H. Juárez, Adrian Carl, Marten Richter, Neus G. Bastús, Horst Weller, Christian Thomsen, Regine von Klitzing, and Andreas Knorr. Tunable Plasmon Coupling in Distance-Controlled Gold Nanoparticles. *Langmuir*, 28(24):8862–8866, 2012.
- [54] Xiaoyun Liu, Xiuqin Wang, Liusheng Zha, Danli Lin, Jianmao Yang, Jianfeng Zhou, and Li Zhang. Temperature- and pH-tunable plasmonic properties and SERS efficiency of the silver nanoparticles within the dual stimuli-responsive microgels. *Journal of Materials Chemistry C*, 2(35):7326–7335, 2014.
- [55] Cristina Fernández-López, Lakshminarayana Polavarapu, Diego M. Solís, José M. Taboada, Fernando Obelleiro, Rafael Contreras-Cáceres, Isabel Pastoriza-Santos, and Jorge Pérez-Juste. Gold Nanorod–pNIPAM Hybrids with Reversible Plasmon Coupling: Synthesis, Modeling, and SERS Properties. *ACS Applied Materials & Interfaces*, 7(23):12530–12538, 2015.
- [56] Hélène Gehan, Laure Fillaud, Mohamed M. Chehimi, Jean Aubard, Andreas Hohenau, Nordin Felidj, and Claire Mangeney. Thermo-induced electromagnetic coupling in gold/polymer hybrid plasmonic structures probed by surface-enhanced raman scattering. *ACS Nano*, 4(11):6491–6500, 2010.
- [57] Tao Ding, Christian Rüttiger, Xuezhi Zheng, Felix Benz, Hamid Ohadi, Guy A. E. Vandenbosch, Victor V. Moshchalkov, Markus Gallei, and Jeremy J. Baumberg. Fast Dynamic Color Switching in Temperature-Responsive Plasmonic Films. *Advanced Optical Materials*, 4(6):877–882, 2016.
- [58] Menglian Wei and Michael J. Serpe. Temperature-Light Dual-Responsive Au@PNIPAm Core-Shell Microgel-Based Optical Devices. *Particle & Particle Systems Characterization*, 36(1):1800326, 2019.
- [59] Tao Ding, Adam W. Rudrum, Lars O. Herrmann, Vladimir Turek, and Jeremy J. Baumberg. Polymer-assisted self-assembly of gold nanoparticle monolayers and their dynamical switching. *Nanoscale*, 8(35):15864–15869, 2016.
- [60] Sean Murphy, Sarah Jaber, Cameron Ritchie, Matthias Karg, and Paul Mulvaney. Laser Flash Photolysis of Au-PNIPAM Core–Shell Nanoparticles: Dynamics of the Shell Response. *Langmuir*, 32(47):12497–12503, 2016.
- [61] Ashavani Kumar, Saikat Mandal, P. R. Selvakannan, Renu Pasricha, A. B. Mandale, and Murali Sastry. Investigation into the Interaction between Surface-Bound Alkylamines and Gold Nanoparticles. *Langmuir*, 19(15):6277–6282, 2003.
- [62] Ezequiel de la Llave, Romain Clarenc, David J. Schiffrin, and Federico J. Williams. Organization of Alkane Amines on a Gold Surface: Structure, Surface Dipole, and Electron Transfer. *The Journal of Physical Chemistry C*, 118(1):468–475, 2014.
- [63] Changwoong Chu, Jeong Seok Na, and Gregory N. Parsons. Conductivity in alkylamine/gold and alkanethiol/gold molecular junctions measured in molecule/nanoparticle/molecule bridges and conducting probe structures. *Journal of the American Chemical Society*, 129(8):2287–2296, 2007.

- [64] Yurui Xue, Xun Li, Hongbin Li, and Wenke Zhang. Quantifying thiol–gold interactions towards the efficient strength control. *Nature Communications*, 5(1):4348, 2014.
- [65] Guangming Liu, He Cheng, Lifeng Yan, and Guangzhao Zhang. Study of the kinetics of the pancake-to-brush transition of poly(N-isopropylacrylamide) chains. *Journal of Physical Chemistry B*, 109(47):22603–22607, 2005.
- [66] P. G. de Gennes. Conformations of Polymers Attached to an Interface. *Macromolecules*, 13(5):1069–1075, 1980.
- [67] Brett W. Garner, Tong Cai, Santaneel Ghosh, Zhibing Hu, and Arup Neogi. Refractive Index Change Due to Volume-Phase Transition in Polyacrylamide Gel Nanospheres for Optoelectronics and Bio-photonics. *Applied Physics Express*, 2(5):057001, 2009.
- [68] Chen Li, Yunwei Ma, and Zhiting Tian. Thermal Switching of Thermoresponsive Polymer Aqueous Solutions. *ACS Macro Letters*, 7(1):53–58, 2018.
- [69] Vladimir O. Aseyev, Heikki Tenhu, and François M. Winnik. *Temperature dependence of the colloidal stability of neutral amphiphilic polymers in water*, volume 196. Springer-Verlag, 2006.
- [70] Christoph Ziegler and Alexander Eychmüller. Seeded Growth Synthesis of Uniform Gold Nanoparticles with Diameters of 15–300 nm. *The Journal of Physical Chemistry C*, 115(11):4502–4506, 2011.
- [71] Felix Benz, Rohit Chikkaraddy, Andrew Salmon, Hamid Ohadi, Bart de Nijs, Jan Mertens, Cloudy Carnegie, Richard W. Bowman, and Jeremy J. Baumberg. SERS of Individual Nanoparticles on a Mirror: Size Does Matter, but so Does Shape. *The Journal of Physical Chemistry Letters*, 7(12):2264–2269, 2016.
- [72] John Turkevich, Peter C. Stevenson, and J. Hillier. The Formation of Colloidal Gold. *The Journal of Physical Chemistry*, 57(7):670–673, 1953.
- [73] J. Kimling, M. Maier, B. Okenve, V. Kotaidis, H. Ballot, and A. Plech. Turkevich method for gold nanoparticle synthesis revisited. *Journal of Physical Chemistry B*, 110(32):15700–15707, 2006.
- [74] Pengxiang Zhao, Na Li, and Didier Astruc. State of the art in gold nanoparticle synthesis. *Coordination Chemistry Reviews*, 257(3):638–665, 2013.
- [75] Chunfang Li, Dongxiang Li, Gangqiang Wan, Jie Xu, and Wanguo Hou. Facile synthesis of concentrated gold nanoparticles with low size-distribution in water: Temperature and pH controls. *Nanoscale Research Letters*, 6(1):1–10, 2011.
- [76] Rafael Contreras-Cáceres, Jessica Pacifico, Isabel Pastoriza-Santos, Jorge Pérez-Juste, Antonio Fernández-Barbero, and Luis M. Liz-Marzán. Au@pNIPAM thermosensitive nanostructures: Control over shell cross-linking, overall dimensions, and core growth. *Advanced Functional Materials*, 19(19):3070–3076, 2009.

- [77] G. Conzatti, S. Cavalie, C. Combes, J. Torrisani, N. Carrere, and A. Tourrette. PNIPAM grafted surfaces through ATRP and RAFT polymerization: Chemistry and bioadhesion. *Colloids and Surfaces B: Biointerfaces*, 151:143–155, 2017.
- [78] Ibrahim B. Malham and Lionel Bureau. Density Effects on Collapse, Compression, and Adhesion of Thermoresponsive Polymer Brushes. *Langmuir*, 26(7):4762–4768, 2010.
- [79] Martin Hegner, Peter Wagner, and Giorgio Semenza. Ultralarge atomically flat template-stripped Au surfaces for scanning probe microscopy. *Surface Science*, 291(1-2):39–46, 1993.
- [80] Wolfgang Haiss, Nguyen T. K. Thanh, Jenny Aveyard, and David G. Fernig. Determination of Size and Concentration of Gold Nanoparticles from UV-Vis Spectra. *Analytical Chemistry*, 79(11):4215–4221, 2007.
- [81] R. Pecora. Dynamic Light Scattering Measurement of Nanometer Particles in Liquids. *Journal of Nanoparticle Research*, 2(2):123–131, 2000.
- [82] William Sutherland. LXXV. A dynamical theory of diffusion for non-electrolytes and the molecular mass of albumin. *The London, Edinburgh, and Dublin Philosophical Magazine and Journal of Science*, 9(54):781–785, 1905.
- [83] M. von Smoluchowski. Zur kinetischen Theorie der Brownschen Molekularbewegung und der Suspensionen. *Annalen der Physik*, 326(14):756–780, 1906.
- [84] Matthew I. Gibson and Rachel K. O’Reilly. To aggregate, or not to aggregate? considerations in the design and application of polymeric thermally-responsive nanoparticles. *Chem. Soc. Rev.*, 42(17):7204–7213, 2013.
- [85] Kenji Kubota, Kenzi Hamano, Nobuhiro Kuwahara, Shouei Fujishige, and Isao Ando. Characterization of Poly(N-isopropylmethacrylamide) in Water. *Polymer Journal*, 22(12):1051–1057, 1990.
- [86] Ruben Esteban, Richard W. Taylor, Jeremy J. Baumberg, and Javier Aizpurua. How Chain Plasmons Govern the Optical Response in Strongly Interacting Self-Assembled Metallic Clusters of Nanoparticles. *Langmuir*, 28(24):8881–8890, 2012.
- [87] Felix Benz, Bart de Nijs, Christos Tserkezis, Rohit Chikkaraddy, Daniel O. Sigle, Laurynas Pukenas, Stephen D. Evans, Javier Aizpurua, and Jeremy J. Baumberg. Generalized circuit model for coupled plasmonic systems. *Optics Express*, 23(26):33255, 2015.
- [88] H. Yim, M. S. Kent, S. Mendez, G. P. Lopez, S. Satija, and Y. Seo. Effects of grafting density and molecular weight on the temperature-dependent conformational change of poly(N-isopropylacrylamide) grafted chains in water. *Macromolecules*, 39(9):3420–3426, 2006.
- [89] Yanjie Zhang, Steven Furyk, David E. Bergbreiter, and Paul S. Cremer. Specific ion effects on the water solubility of macromolecules: PNIPAM and the Hofmeister series. *Journal of the American Chemical Society*, 127(41):14505–14510, 2005.

- [90] C. Tserkezis, R. Esteban, D. O. Sigle, J. Mertens, L. O. Herrmann, J. J. Baumberg, and J. Aizpurua. Hybridization of plasmonic antenna and cavity modes: Extreme optics of nanoparticle-on-mirror nanogaps. *Physical Review A*, 92(5):053811, 2015.
- [91] Rohit Chikkaraddy, Xuezi Zheng, Felix Benz, Laura J. Brooks, Bart de Nijs, Cloudy Carnegie, Marie-Elena Kleemann, Jan Mertens, Richard W. Bowman, Guy A. E. Vandenbosch, Victor V. Moshchalkov, and Jeremy J. Baumberg. How Ultranarrow Gap Symmetries Control Plasmonic Nanocavity Modes: From Cubes to Spheres in the Nanoparticle-on-Mirror. *ACS Photonics*, 4(3):469–475, 2017.
- [92] Min Hu, Amitabh Ghoshal, Manuel Marquez, and Pieter G. Kik. Single Particle Spectroscopy Study of Metal-Film-Induced Tuning of Silver Nanoparticle Plasmon Resonances. *The Journal of Physical Chemistry C*, 114(16):7509–7514, 2010.
- [93] Chatdanai Lumdee, Seyfollah Toroghi, and Pieter G. Kik. Post-fabrication Voltage Controlled Resonance Tuning of Nanoscale Plasmonic Antennas. *ACS Nano*, 6(7):6301–6307, 2012.
- [94] Tao Ding, Daniel Sigle, Liwu Zhang, Jan Mertens, Bart de Nijs, and Jeremy J. Baumberg. Controllable Tuning Plasmonic Coupling with Nanoscale Oxidation. *ACS Nano*, 9(6):6110–6118, 2015.
- [95] W. Lukosz. Light emission by magnetic and electric dipoles close to a plane dielectric interface III Radiation patterns of dipoles with arbitrary orientation. *Journal of the Optical Society of America*, 69(11):1495, 1979.
- [96] J. Mertens, A. Demetriadou, R. W. Bowman, F. Benz, M.-E. Kleemann, C. Tserkezis, Y. Shi, H. Y. Yang, O. Hess, J. Aizpurua, and J. J. Baumberg. Tracking Optical Welding through Groove Modes in Plasmonic Nanocavities. *Nano Letters*, 16(9):5605–5611, 2016.
- [97] A. Plech, V. Kotaidis, S. Grésillon, C. Dahmen, and G. Von Plessen. Laser-induced heating and melting of gold nanoparticles studied by time-resolved x-ray scattering. *Physical Review B - Condensed Matter and Materials Physics*, 70(19):1–7, 2004.
- [98] Tao Ding, Jan Mertens, Daniel O. Sigle, and Jeremy J. Baumberg. Capillary-Force-Assisted Optical Tuning of Coupled Plasmons. *Advanced Materials*, 27(41):6457–6461, 2015.
- [99] Lie-Wen Xia, Rui Xie, Xiao-Jie Ju, Wei Wang, Qianming Chen, and Liang-Yin Chu. Nano-structured smart hydrogels with rapid response and high elasticity. *Nature Communications*, 4(1):2226, 2013.
- [100] Xiaobo Zhang, Cary L. Pint, Min Hyung Lee, Bryan Edward Schubert, Arash Jamshidi, Kuniharu Takei, Hyunhyub Ko, Andrew Gillies, Rizia Bardhan, Jeffrey J. Urban, Ming Wu, Ronald Fearing, and Ali Javey. Optically- and Thermally-Responsive Programmable Materials Based on Carbon Nanotube-Hydrogel Polymer Composites. *Nano Letters*, 11(8):3239–3244, 2011.

- [101] Wesley R. Browne and Ben L. Feringa. Making molecular machines work. *Nature Nanotechnology*, 1(1):25–35, 2006.
- [102] Xi Chen, Yiting Chen, Min Yan, and Min Qiu. Nanosecond Photothermal Effects in Plasmonic Nanostructures. *ACS Nano*, 6(3):2550–2557, 2012.
- [103] Issei Aibara, Shinya Mukai, and Shuichi Hashimoto. Plasmonic-Heating-Induced Nanoscale Phase Separation of Free Poly(N-isopropylacrylamide) Molecules. *Journal of Physical Chemistry C*, 120, 2016.
- [104] A. W. C. Lau, M. Portigliatti, E. Raphaël, and L. Léger. Spreading of latex particles on a substrate. *Europhysics Letters*, 60(5):717–723, 2002.
- [105] D. Leckband and J. Israelachvili. Intermolecular forces in biology. *Quarterly reviews of biophysics*, 34(2):105–267, 2001.
- [106] Taehoon Kim, Kangtaek Lee, Myoung Seon Gong, and Sang Woo Joo. Control of gold nanoparticle aggregates by manipulation of interparticle interaction. *Langmuir*, 21(21):9524–9528, 2005.
- [107] A. J. Hallock, P. L. Redmond, and L. E. Brus. Optical forces between metallic particles. *Proceedings of the National Academy of Sciences of the United States of America*, 102(5):1280–4, 2005.
- [108] Anders Kristensen, Joel K. W. Yang, Sergey I. Bozhevolnyi, Stephan Link, Peter Nordlander, Naomi J. Halas, and N. Asger Mortensen. Plasmonic colour generation. *Nature Reviews Materials*, 2(1):16088, 2016.
- [109] Lei Shao, Xiaolu Zhuo, and Jianfang Wang. Advanced Plasmonic Materials for Dynamic Color Display. *Advanced Materials*, 30(16):1704338, 2018.
- [110] Jialong Peng, Hyeon-Ho Jeong, Qianqi Lin, Sean Cormier, Hsin-Ling Liang, Michael F. L. De Volder, Silvia Vignolini, and Jeremy J. Baumberg. Scalable electrochromic nanopixels using plasmonics. *Science Advances*, 5(5):eaaw2205, 2019.
- [111] Thang B. Hoang and Maiken H. Mikkelsen. Broad electrical tuning of plasmonic nanoantennas at visible frequencies. *Applied Physics Letters*, 108(18):183107, 2016.
- [112] Vadim A. Markel. Introduction to the Maxwell Garnett approximation: tutorial. *Journal of the Optical Society of America A*, 33(7):1244, 2016.
- [113] R. Ruppin. Evaluation of extended Maxwell-Garnett theories. *Optics Communications*, 182(4-6):273–279, 2000.
- [114] Neal J. Hutchinson, Thomas Coquil, Erik K. Richman, Sarah H. Tolbert, and Laurent Pilon. Reflectance of surfactant-templated mesoporous silica thin films: Simulations versus experiments. *Thin Solid Films*, 518(8):2134–2140, 2010.
- [115] J. C. Maxwell Garnett. Colours in Metal Glasses and in Metallic Films. *Philosophical Transactions of the Royal Society A: Mathematical, Physical and Engineering Sciences*, 203(359-371):385–420, 1904.

- [116] D. A. G. Bruggeman. Berechnung verschiedener physikalischer Konstanten von heterogenen Substanzen. I. Dielektrizitätskonstanten und Leitfähigkeiten der Mischkörper aus isotropen Substanzen. *Annalen der Physik*, 416(7):636–664, 1935.
- [117] Gunnar Niklasson, Claes Granqvist, and O. Hunderi. Effective medium models for the optical-properties of inhomogeneous materials. *Applied optics*, 20:26–30, 1981.
- [118] Oleksandr Zhuromskyy. Applicability of Effective Medium Approximations to Modelling of Mesocrystal Optical Properties. *Crystals*, 7(1):1, 2016.
- [119] S. Torquato, T. M. Truskett, and P. G. Debenedetti. Is random close packing of spheres well defined? *Physical Review Letters*, 84(10):2064–2067, 2000.
- [120] M. Born and E. Wolf. *Principles of optics*. Pergamon Press, 1999.
- [121] Pierre Lecaruyer, Emmanuel Maillart, Michael Canva, and Jannick Rolland. Generalization of the Rouard method to an absorbing thin film stack and application to surface plasmon resonance. *Applied optics, Optical Society of America*, 45(33):8419–8423, 2006.
- [122] Pierre Rouard. Études des propriétés optiques des lames métalliques très minces. *Annales de physique*, 7(2):291–384, 1937.
- [123] J. Wang, D. Gan, L. A. Lyon, and M. A. El-Sayed. Temperature-jump investigations of the kinetics of hydrogel nanoparticle volume phase transitions. *Journal of the American Chemical Society*, 123(45):11284–11289, 2001.
- [124] Mitsuhiro Shibayama and Kohji Nagai. Shrinking Kinetics of Poly(N-isopropylacrylamide) Gels T-Jumped across Their Volume Phase Transition Temperatures. *Macromolecules*, 32(22):7461–7468, 1999.
- [125] Thearith Ung, Luis M. Liz-Marzán, and Paul Mulvaney. Gold nanoparticle thin films. *Colloids and Surfaces A: Physicochemical and Engineering Aspects*, 202(2):119–126, 2002.
- [126] Nicolas Vogel, Clemens K. Weiss, and Katharina Landfester. From soft to hard: The generation of functional and complex colloidal monolayers for nanolithography. *Soft Matter*, 8(15):4044–4061, 2012.
- [127] Zhilin Yang, Shu Chen, Pingping Fang, Bin Ren, Hubert H. Girault, Zhongqun Tian, I. Benjamin, P. Vanýsek, and M. L. Schlossman. LSPR properties of metal nanoparticles adsorbed at a liquid–liquid interface. *Physical Chemistry Chemical Physics*, 15(15):5374, 2013.
- [128] Ping-Ping Fang, Shu Chen, Haiqiang Deng, Micheál D. Scanlon, Frédéric Gumy, Hye Jin Lee, Dmitry Momotenko, Véronique Amstutz, Fernando Cortés-Salazar, Carlos M. Pereira, Zhilin Yang, and Hubert H. Girault. Conductive Gold Nanoparticle Mirrors at Liquid/Liquid Interfaces. *ACS Nano*, 7:9241–9248, 2013.

- [129] Frances Y. Pong, Michelle Lee, Jessica R. Bell, and Nolan T. Flynn. Thermoresponsive behavior of poly(N-isopropylacrylamide) hydrogels containing gold nanostructures. *Langmuir*, 22(8):3851–3857, 2006.
- [130] Yu Chen, Richard E. Palmer, and Jess P. Wilcoxon. Sintering of passivated gold nanoparticles under the electron beam. *Langmuir*, 22(6):2851–2855, 2006.
- [131] Koichi Nakaso, Manabu Shimada, Kikuo Okuyama, and Knut Deppert. Evaluation of the change in the morphology of gold nanoparticles during sintering. *Journal of Aerosol Science*, 33(7):1061–1074, 2002.
- [132] Michael J. Coutts, Michael B. Cortie, Michael J. Ford, and Andrew M. McDonagh. Rapid and Controllable Sintering of Gold Nanoparticle Inks at Room Temperature Using a Chemical Agent. *The Journal of Physical Chemistry C*, 113(4):1325–1328, 2009.
- [133] Ioannis Kanelidis and Tobias Kraus. The role of ligands in coinage-metal nanoparticles for electronics. *Beilstein journal of nanotechnology*, 8:2625–2639, 2017.
- [134] Seung H. Ko, Heng Pan, Costas P. Grigoropoulos, Christine K. Luscombe, Jean M. J. Fréchet, and Dimos Poulikakos. All-inkjet-printed flexible electronics fabrication on a polymer substrate by low-temperature high-resolution selective laser sintering of metal nanoparticles. *Nanotechnology*, 18(34):345202, 2007.
- [135] Ernst Florey. Ultrastructure and function of cephalopod chromatophores. *Integrative and Comparative Biology*, 9(2):429–442, 1969.
- [136] Susumu Aoyama, Masahiko Shimoike, and Yuichi Hiratsuka. Self-organized optical device driven by motor proteins. *Proceedings of the National Academy of Sciences*, 110(41):16408–16413, 2013.
- [137] C. Yu, Y. Li, X. Zhang, X. Huang, V. Malyarchuk, S. Wang, Y. Shi, L. Gao, Y. Su, Y. Zhang, H. Xu, R. T. Hanlon, Y. Huang, and J. A. Rogers. Adaptive optoelectronic camouflage systems with designs inspired by cephalopod skins. *Proceedings of the National Academy of Sciences*, 111(36):12998–13003, 2014.
- [138] Stephen A. Morin, Robert F. Shepherd, Sen Wai Kwok, Adam A. Stokes, Alex Nemiroski, and George M. Whitesides. Camouflage and display for soft machines. *Science*, 337(6096):828–832, 2012.
- [139] Chengyi Xu, George T. Stiubianu, and Alon A. Gorodetsky. Adaptive infrared-reflecting systems inspired by cephalopods. *Science*, 359(6383):1495–1500, 2018.
- [140] Leilei Xu, Fangzhi Mou, Haotian Gong, Ming Luo, and Jianguo Guan. Light-driven micro/nanomotors: from fundamentals to applications. *Chemical Society Reviews*, 46(22):6905–6926, 2017.
- [141] Stefano Palagi, Andrew G. Mark, Shang Yik Reigh, Kai Melde, Tian Qiu, Hao Zeng, Camilla Parmeggiani, Daniele Martella, Alberto Sanchez-Castillo, Nadia Kapernaum, Frank Giesselmann, Diederik S. Wiersma, Eric Lauga, and Peer Fischer. Structured light enables biomimetic swimming and versatile locomotion of photoresponsive soft microrobots. *Nature Materials*, 15(6):647–653, 2016.

- [142] Baohu Dai, Jizhuang Wang, Ze Xiong, Xiaojun Zhan, Wei Dai, Chien Cheng Li, Shien Ping Feng, and Jinyao Tang. Programmable artificial phototactic microswimmer. *Nature Nanotechnology*, 11(12):1087–1092, 2016.
- [143] M. Y. Lin, H. M. Lindsay, D. A. Weitz, R. Klein, R. C. Ball, and P. Meakin. Universal diffusion-limited colloid aggregation. *Journal of Physics: Condensed Matter*, 2(13):3093–3113, 1990.
- [144] Anastasiya Derkachova, Krystyna Kolwas, and Iraida Demchenko. Dielectric Function for Gold in Plasmonics Applications: Size Dependence of Plasmon Resonance Frequencies and Damping Rates for Nanospheres. *Plasmonics*, 11(3):941–951, 2016.
- [145] Andrew R. Salmon, Ruben Esteban, Richard W. Taylor, James T. Hugall, Clive A. Smith, Graeme Whyte, Oren A. Scherman, Javier Aizpurua, Chris Abell, and Jeremy J. Baumberg. Monitoring Early-Stage Nanoparticle Assembly in Microdroplets by Optical Spectroscopy and SERS. *Small*, 12(13):1788–1796, 2016.
- [146] Zifu Li, Walter Richtering, and To Ngai. Poly(N-isopropylacrylamide) microgels at the oil–water interface: temperature effect. *Soft Matter*, 10(33):6182–6191, 2014.
- [147] Cécile Monteux, Claire Marlière, Pauline Paris, Nadège Pantoustier, Nicolas Sanson, and Patrick Perrin. Poly(N-isopropylacrylamide) microgels at the oil-water interface: Interfacial properties as a function of temperature. *Langmuir*, 26(17):13839–13846, 2010.
- [148] E. M. Purcell. Life at low Reynolds number. *American Journal of Physics*, 45(1):3–11, 1977.
- [149] Stephan Herminghaus, Corinna C. Maass, Carsten Krüger, Shashi Thutupalli, Lucas Goehring, and Christian Bahr. Interfacial mechanisms in active emulsions. *Soft Matter*, 10(36):7008–7022, 2014.
- [150] Rubin Battino, Timothy R. Rettich, and Toshihiro Tominaga. The Solubility of Nitrogen and Air in Liquids. *Journal of Physical and Chemical Reference Data*, 13(2):563–600, 1984.
- [151] P. Wismann and R. E. Hummell. *Handbook of Optical Properties: Optics of small particles, interfaces, and surfaces, vol II*. CRC Press, 1997.
- [152] Mark W. Knight, Nicholas S. King, Lifei Liu, Henry O. Everitt, Peter Nordlander, and Naomi J. Halas. Aluminum for Plasmonics. *ACS Nano*, 8(1):834–840, 2014.
- [153] Vladimir A. Turek, Sean Cormier, Benjamin Sierra-Martin, Ulrich F. Keyser, Tao Ding, and Jeremy J. Baumberg. The Crucial Role of Charge in Thermoresponsive-Polymer-Assisted Reversible Dis/Assembly of Gold Nanoparticles. *Advanced Optical Materials*, 6(8):1701270, 2018.

-
- [154] Thomas R. Wilks, Jonathan Bath, Jan Willem De Vries, Jeffery E. Raymond, Andreas Herrmann, Andrew J. Turberfield, and Rachel K. O'Reilly. "giant surfactants" created by the fast and efficient functionalization of a DNA tetrahedron with a temperature-responsive polymer. *ACS Nano*, 7(10):8561–8572, 2013.
- [155] Yuhang Hu, Philseok Kim, and Joanna Aizenberg. Harnessing structural instability and material instability in the hydrogel-actuated integrated responsive structures (HAIRS). *Extreme Mechanics Letters*, 13:84–90, 2017.
- [156] Shuaizhong Zhang, Ye Wang, Reinoud Lavrijsen, Patrick R. Onck, and Jaap M. J. den Toonder. Versatile microfluidic flow generated by moulded magnetic artificial cilia. *Sensors and Actuators, B: Chemical*, 263:614–624, 2018.
- [157] Ye Wang, Jaap den Toonder, Ruth Cardinaels, and Patrick Anderson. A continuous roll-pulling approach for the fabrication of magnetic artificial cilia with microfluidic pumping capability. *Lab on a Chip*, 16(12):2277–2286, 2016.
- [158] Syed N. Khaderi, Jaap M.J. den Toonder, and Patrick R. Onck. Magnetic artificial cilia for microfluidic propulsion. *Advances in Applied Mechanics*, 48:1–78, 2015.